Mathematical and Computational Modeling of Injection-induced Seismicity

by

Maryam Alghannam

B.S., Texas A&M University (2012)

M.S., University of California at Berkeley (2017)

Submitted to the Department of Civil and Environmental Engineering
and the Center for Computational Science and Engineering
in partial fulfillment of the requirements for the degree of

Doctor of Philosophy

at the

MASSACHUSETTS INSTITUTE OF TECHNOLOGY

February 2023

Author .....

Department of Civil and Environmental Engineering and the Center for Computational Science and Engineering

January 13, 2023

Certified by .....

Ruben Juanes

Professor of Civil and Environmental Engineering

Professor of Earth, Atmospheric, and Planetary Sciences

Thesis Supervisor

Accepted by .....

Colette Heald

Professor of Civil and Environmental Engineering

Chair, Graduate Program Committee

Accepted by .....

Nicolas Hadjiconstantinou

Professor of Mechanical Engineering

Co-Director, Center for Computational Science and Engineering

Mathematical and Computational Modeling of Injection-induced Seismicity

by

Maryam Alghannam

Submitted to the Department of Civil and Environmental Engineering and the
Center for Computational Science and Engineering
on January 13, 2023, in partial fulfillment of the
requirements for the degree of
Doctor of Philosophy

Abstract

It has long been recognized that pumping fluids into or out of the Earth has the potential to cause earthquakes. Some of the earliest field evidence dates to the 1960s, when earthquakes were turned on and off by water injection in Rangely, Colorado. More recently, induced seismicity has been reported worldwide in connection with many subsurface technologies, including wastewater disposal, natural gas storage, enhanced geothermal systems, and hydraulic fracturing. As a result, there has been a growing public concern around the world about the potential seismic hazard and environmental impact of subsurface energy technologies. Understanding the physical mechanisms that lead to induced seismicity is essential in efforts to mitigate the risk associated with subsurface operations. As a first step in this thesis, we develop a spring-poroslider model of frictional slip as an analogue for induced seismicity, and analyze conditions for the emergence of stick-slip frictional instability—the mechanism for earthquakes—by carrying out a linear stability analysis and nonlinear simulations. We found that the likelihood of triggering earthquakes depends largely on the rate of increase in pore pressure rather than its magnitude. Thus, the model explains the common observation that abrupt increases in injection rate increase the seismic risk. Second, we perform an energy analysis using the same spring-poroslider model to shed light into the partitioning of energy released into frictional and radiated energy—since the latter is associated with the overall size of the earthquake and its potential for damage to man-made structures. Two key elements of the analysis are: (1) incorporating seismic radiation within the model using a precisely-defined viscous damper, and (2) partitioning the energy supplied by fluid injection into dissipated and stored energy in fluid and skeleton. The analysis shows how the rate of increase in pore pressure controls the radiated energy, stress drop, and total slip of the earthquake. Third, we study the effect of heterogeneity on the dynamics of frictional faults. In particular, we develop an objective (frame-indifferent) formulation of frictional contact between heterogeneous surfaces at a small scale, and introduce the notion that friction is a function of the states of the two surfaces in contact, each representing

roughness and microstructural details for the surface. We then conduct dynamic simulations of a spring-slider model and show that heterogeneous Coulomb friction alone is capable of reproducing the transitions in complex frictional behavior, from stable creep to regular earthquakes and slow slip. This thesis, as a whole, enhances our understanding of the mechanics of fluid-injection-induced earthquakes and suggests strategies that mitigate or minimize the seismic risk associated with a wide range of subsurface operations, from hydraulic fracturing and geothermal energy extraction to wastewater injection and geologic CO2 sequestration.

Thesis Supervisor: Ruben Juanes
Title: Professor of Civil and Environmental Engineering
Professor of Earth, Atmospheric, and Planetary Sciences

Acknowledgments

This thesis would not have been possible without the support of many people, to whom I am very grateful. My thesis supervisor Ruben Juanes has been the best mentor I have ever had. Coming to MIT, I had no prior research experience nor any real knowledge of academia as a field. He introduced me to scientific research and showed me how fun it can be. He also provided a nurturing environment in which I was able to explore new areas and lead my own research projects. His enthusiasm for what I do has been a great source of motivation to push through difficult obstacles and research setbacks throughout my PhD journey. Because of him, the doors of academia opened up widely for me. Ruben will continue to be a role model as an academic who cares deeply about his students and places their growth and well-being above his research output or metrics.

My thesis committee members Brad Hager, Tal Cohen, and Youssef Marzouk have been source of intellectual discussion. Their comments on my work during annual meetings leading up to the defense improved the quality of this thesis. My collaborators Hector Gomez from Purdue University and Jan Nordbotten from the University of Bergen have been instrumental in the work presented in chapter 3 and chapter 4, respectively. Hector provided valuable technical feedback on energy analyses with his strong background in mechanics and applied mathematics. Jan inspired a creative outlook by sparking new ideas and challenging existing formulations of friction.

In addition to the people who supported my research, many others supported me emotionally and made my time at MIT worthwhile. Members of the Juanes research group Rebecca Liyanage, Lluis Salo, Yu Qiu, and Bauyrzhan Primkulov have been wonderful colleagues and friends. Bauyrzhan and Maksuda are some of the people I am most grateful for during my PhD. Their generosity, patience, and kindness helped me tremendously—especially during the pandemic. My Saudi friends Arwa Albaadi, Lubna Bargouthy, and Jawaher Almutlaq made my time at MIT more joyful and fun. Fatimah Ismail has been one of my closest friends for nearly 15 years. Despite being far away and busy with work and family, she always found the time to listen to me

whenever I needed. Last but not least, my family has been the greatest source of inspiration and support not only during my PhD but throughout my whole academic journey. Having Ahmed, Lujain, Afnan, Mohammed, and Merna as my siblings and Ali and Naeemah as my parents has been the greatest gift in my life.

Contents

List of Figures

List of Tables

Chapter 1

Introduction

Induced seismicity is a central issue in the development of subsurface energy technologies around the world (National Research Council, 2013). Examples include subsurface waste water injection, reservoir impoundment in the vicinity of large dams, and development of mining, geothermal or hydrocarbon resources. Recently, induced seismicity has also become a concern in connection with geologic carbon sequestration projects. Figure 1-1 provides an overview on the geographical distribution of induced seismicity, classified by magnitude and industrial activity (Grigoli et al., 2017). The majority of events are related to fluid injection. In Basel Switzerland, for example, the injection of water at high pressure into permeable basement rocks to develop and enhance geothermal system underneath the city induced earthquakes in 2006 and 2007 (Deichmann and Giardini, 2009). In central United States, the number of earthquakes of magnitude Mw>3 rose significantly over the past few years; from an average rate of 21 events per year in the period between 1970 and 2000 to more than 300 earthquakes in the years from 2010 to 2012 (Ellsworth, 2013). While most of the injection-induced earthquakes are micro-tremors, they can occasionally be of large magnitude, such as the Prague M_w 5.7 earthquake in 2011 (Keranen et al., 2014), the Pawnee M_w 5.8 earthquake in 2016 (Yeck et al., 2017), and the Pohang M_w 5.5 earthquake in 2017 (Grigoli et al., 2018), among others.

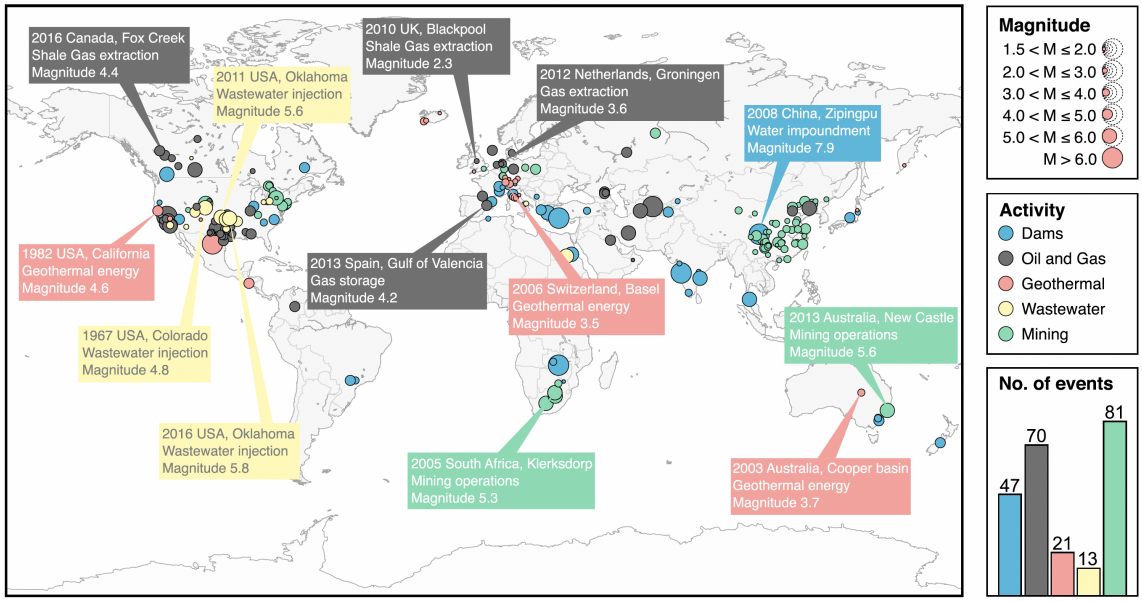

Figure 1-1: Induced and triggered seismicity has been observed worldwide in conjunction with several industrial activities (taken from Grigoli et al. (2017)).

1.1 Field observations

It has been hypothesized that increases in fluid pressure could induce earthquakes since the 1960s (Pratt and Johnson, 1926; Hough and Page, 2015; Hubbert and Rubey, 1959), but it was not until 1976 when this hypothesis was confirmed by a field experiment at Rangely Colorado (Raleigh et al., 1976). The experiment began in 1969, when a seismic network of 14-short period, vertical seismometers was installed. The network recorded the seismic activity under unaltered fluid pressure conditions for one year. After then, two full cycles of increased fluid injection and back-flowing were performed. Raleigh et al. (1976) found that seismic activity responded promptly to changes in fluid pressure. However, high fluid pressures do not always result in earthquakes. Cogdell oil field in Texas, for example, had numerous injection sites with high injection pressures and volumes of injected fluid (Davis and Pennington, 1989). Failure could occur by Mohr-Coulomb law in these sites, but no earthquakes have been observed. It was concluded that failure must have occurred aseismically. Interestingly, earthquakes were found to occur in sites of relatively low pressure surrounded by high fluid pressure. Rangely and Cogdell are not the only fields where

increases in fluid pressure led to inconsistent outcomes. Increases in fluid pressure led to seismic slip in many other fields (Majer et al., 2007; Healy et al., 1968; Raleigh et al., 1976; Keranen et al., 2014; Yeck et al., 2017; Grigoli et al., 2018) and aseismic slip in others (Guglielmi et al., 2015; Cornet et al., 1997; Bourouis and Bernard, 2007; Zoback et al., 2012; Wei et al., 2015).

Several field observations link the temporal variations in fluid pressure with the occurrence of earthquakes. Seismicity in Hutubi gas field in China between 2013 and 2015, for example, did not correlate with total gas injection volume or well pressure (Tang et al., 2018). It instead occurred eleven to seventeen hours after simultaneous abrupt increases and decreases of well pressure. At Val d'Agri oil field in Italy, seismicity has been induced by rapid communication of fluid pressure perturbations along a high-permeability fault zone favorably oriented with respect to the local extensional stress field (Improta et al., 2015; Hager et al., 2021). It was found, for the period between 2006 and 2015, that seismicity rate correlates with short-term injection pressure. Youngstown, Ohio—an area with no known earthquakes—experienced 109 small earthquakes close to a deep injection well from 2011 to 2012. It was observed that several periods of quiescence of seismicity follow minima in injection volumes and pressure, indicating that earthquakes were directly caused by sharp pressure buildup and stopped when pressure dropped. At the enhanced geothermal simulation site of Soultz-sous-Forets in France, the evolution of seismicity was also found to strongly depend on the variations of well head pressure. Abrupt increases led to changes in the number and magnitude of micro-seismic events.

Spatial heterogeneity and variations in fluid pressure have also been observed to influence the occurrence of earthquakes. Measurements of the spatial decay of induced earthquakes from causative wells worldwide indicate two types of spatial decay (Kraft and Deichmann, 2014; Ogwari et al., 2018; Block et al., 2014; Martínez-Garzón et al., 2014; Horton, 2012; Duboeuf et al., 2017; Baisch et al., 2006; Albaric et al., 2014; Baisch et al., 2002; Diehl et al., 2021; Evans et al., 2012). The first type is sequences with an extended plateau close to the well followed by an abrupt decay within less than 1 km, and the second is sequences with steady, power law-like decay

out to distances of more than 10 km (Goebel and Brodsky, 2018). The rate of spatial decay of aftershocks also varies. For example, it has been observed that the decay is more rapid in Oklahoma than in Southern California (Rosson et al., 2019). The spatial distribution of induced earthquakes follows fluid pressure diffusion, in respect of their rate of spatial growth, their geometry, and their spatial density (Shapiro et al., 2003). Low permeability in regions of stratigraphic transitions can limit the spatial extent of seismicity (Lambert, 2017). For example, seismicity is observed to be contained within carbonate reefs at Cogdell Texas (Davis and Pennington, 1989), and concentrates along the edges of reefs in Alberta, Canada (Schultz et al., 2016). High permeability, on the other hand, can extend seismicity tens of kilometers from wells (Keranen et al., 2014; King et al., 2014; Mulargia and Bizzarri, 2014; Yeck et al., 2016).

1.2 Laboratory observations

To the best of our knowledge, there are at least 13 experimental studies that consider the effects of fluid pressurization on friction and fault stability, with the goal of explaining field observations of induced earthquakes. Six of these experiments are performed on bare rock surfaces (Byerlee and Brace, 1972; Wang et al., 2020b; French et al., 2016; Ougier-Simonin and Zhu, 2013; Rutter and Hackston, 2017; Gori et al., 2021), six are performed on granular gouge materials (Sawai et al., 2016; Scuderi and Collettini, 2016; Scuderi et al., 2017; Scuderi and Collettini, 2018; Cappa et al., 2019; Ikari et al., 2009), and one combines both (Xing et al., 2019).

Bare rock surfaces

French et al. (2016) performed axial compression and lateral relaxation tests on permeable sandstones with saw-cut surfaces. Their experiment shows that a gradual increase in pore pressure results in unstable slip during the transient-state, and that the degree of instability measured by the total slip, slip rate, and shear stress drop correlates with the rate of pore pressure increase.

Wang et al. (2020b) conducted fluid-induced fault slip experiments in the laboratory on critically stressed saw-cut sandstone samples with high permeability using different fluid pressurization rates. Their experimental results demonstrate that fault slip behavior is governed by fluid pressurization rate rather than injection pressure. Slow stick-slip episodes (peak slip velocity < 4 μm/s) are induced by fast fluid injection rate, whereas fault creep with slip velocity < 0.4 μm/s mainly occurs in response to slow fluid injection rate. Their results indicate that the coefficient of friction is generally between 0.6 and 0.85. During fluid pressurization, the coefficient of friction appears to slightly increase up to a static friction coefficient just before onset of sliding, and then drops rapidly as fault sliding accelerated to maximum sliding velocity.

Gori et al. (2021) used a laboratory earthquake setup with PMMA to compare the rupture behavior for different rates of fluid injection: fast (megapascals per second) versus slow (megapascals per hour). They found that, in cases of rapid increase in pore pressure, unstable, fast slip is promoted nearly instantaneously and for rupture lengths considerably smaller than the critical sizes predicted by the quasistatic theoretical estimates. In cases of gradual pore pressure increase, considerably less fluid is delivered into the fault prior to the nucleation of seismic events, and dynamic slip is triggered at lower levels of fluid pore pressure. They also found that the resulting dynamic ruptures propagating over wetted interfaces exhibit dynamic stress drops almost twice as large as those over the dry interfaces.

Byerlee and Brace (1972) performed triaxial loading experiments on a fine-grained gabbro rock. They found that sliding between two rock surfaces is much more stable at high than at low steady-state pore pressure. Sliding is observed to be by slow, steady-type motion at high pore pressure, and by stick-slip at low pore pressure. Rutter and Hackston (2017) performed triaxial experiments on pre-cut planar surfaces in Darley Dale and Pennant sandstones. They found that sudden access by overpressured fluid to the fault plane via hydrofracture causes seismic fault slip. Ougier-Simonin and Zhu (2013) conducted deformation experiments with and without excess pore pressure on intact porous Berea sandstone samples. They found that excess pore pressure induces

slow slip.

Granular gouge materials

Ikari et al. (2009) and Scuderi and Collettini (2018) conducted experiments using a pressure vessel within a servocontrolled biaxial testing apparatus under true-triaxial conditions and experiments using a biaxial apparatus configured in a double-direct shear geometry within a pressure vessel, respectively. They measured the strength and friction constitutive properties of saturated shale and clay-rich fault gouges. They found that the gouges are consistently weak with steady-state coefficient of sliding of friction of < 0.35. They also found that, at effective normal stresses from 12 to 59 MPa, all gouges show velocity-strengthening frictional behavior in the sliding velocity range 0.5 – 300 mm/s.

Cappa et al. (2019) conducted triaxial loading experiments on limestone fault gouge sample. They examined rate dependence of frictional behavior as a function of slip velocity for different values of fluid pressure and effective normal stress. They found that rate weakening mainly occurs at low velocities (< 10 μm/s), which is a necessary condition for the nucleation of seismic slip. At higher velocities, the fault mainly becomes rate strengthening, which is indicative of stable aseismic slip. At fluid pressure above 1.5 MPa, the fault friction switches from rate weakening at low slip velocity (0.1 to 1 μm/s) to rate strengthening at high slip velocity (10 to μm/s), delineating two regimes of frictional behavior. This transition means that the unstable slip is suppressed above a threshold velocity and the aseismic creep is sustained.

Sawai et al. (2016) performed shear experiments on blueschist fault gouge using a hydrothermal ring shear apparatus. Their results show a transition from stable to unstable slip with increasing fluid pressure caused by a decrease in parameters controlling frictional evolution. Scuderi et al. (2017) and Scuderi and Collettini (2016) performed shear experiments on carbonate fault gouge in a double direct shear configuration with a triaxial pressure vessel. They found that fluid pressurization triggers dynamic instability even in cases of velocity strengthening friction, and that friction evolves from velocity strengthening to velocity neutral as a result of increase fluid

pressure—possibly facilitating dynamic slip.

Rock surfaces separated by gouge materials

Xing et al. (2019) investigated whether the strengthening effect of high pore pressure holds true for frictional slip along gouge-bearing experimental faults. Saw cut porous sandstone samples with a layer of gouge powders, placed between the precut surfaces were deformed in the conventional triaxial loading configuration. In disagreement with the previous experiments performed on shearing granular gouge materials, they demonstrate that under constant effective pressure, increasing pore pressure stabilizes the frictional slip of faults with all four gouge materials including antigorite, olivine, quartz, and chrysotile. The stabilizing effect, enhanced by increasing fluid pressure, is characterized by a gradual increase in parameters controlling frictional evolution.

1.3 Previous modeling studies

Field and laboratory observations have motivated the development of different mathematical and numerical models to understand the physical mechanisms behind injection-induced seismicity, including seismicity-rate models (Langenbruch et al., 2018; Norbeck and Rubinstein, 2018; Zhai et al., 2019; Shapiro and Dinske, 2009) and 2D numerical simulations of coupled flow-geomechanics (Torberntsson et al., 2018; Pampillón et al., 2018). Seismicity-rate models consider the large-scale spatiotemporal effects of nonlinear diffusion on the probability of a given magnitude earthquake using Gutenberg-Richter statistics. The numerical simulations study fault slip triggered by fluid injection and diffusion in a 2D poroelastic continuum, where earthquake triggering depends the Coulomb failure criterion (Hubbert and Rubey, 1959; Healy et al., 1968; Segall and Lu, 2015). According to this criterion, pore pressure perturbations and poroelastic stress changes increase the ratio of shear to effective normal stress which in turn cause a fault to slip. These models, however, do not address the dynamics of the rupture and whether a fault slips seismically or aseismically. An increase in pore pressure from fluid injection, for instance, leads to seismic slip in some sites

(Majer et al., 2007; Healy et al., 1968; Raleigh et al., 1976; Keranen et al., 2014; Yeck et al., 2017; Grigoli et al., 2018) and aseismic slip in others (Davis and Pennington, 1989; Guglielmi et al., 2015; Cornet et al., 1997; Bourouis and Bernard, 2007; Zoback et al., 2012; Wei et al., 2015).

Different criteria, derived from stability analyses of models of frictional slip between elastic media, are often used to differentiate between seismic and aseismic fault slip (Ruina, 1983; Rice and Tse, 1986; Ranjith and Rice, 1999). Frictional slip is described by the laboratory-derived rate-and-state constitutive laws, which are capable of reproducing a wide range of observed seismic and aseismic fault behaviors ranging from preseismic slip and earthquake nucleation to coseismic rupture and earthquake after slip (Dieterich, 1979a,b; Ruina, 1983; Marone, 1998). The formulation of rate-and-state laws combines the logarithmic increase of static friction with hold time and the slip weakening behavior during dynamic instabilities in a unified and consistent manner. They describe frictional stress as a function of effective normal stress and a coefficient of friction that is dependent on slip velocity and the state of the sliding surface, and take the following form

$$\tau = \mu(v, \theta)\sigma', \tag{1.1}$$

$$\mu(v, \theta) = \mu_* + a \ln \frac{v}{v_*} + \theta, \tag{1.2}$$

$$\dot{\theta} = -\frac{v}{d_c}(\theta + b \ln \frac{v}{v_*}) - \alpha \frac{\dot{\sigma}'}{\sigma'}, \tag{1.3}$$

where τ is the frictional stress, σ' is the effective normal stress (the difference between total normal stress and pore pressure), μ is the coefficient of friction, v is the slider's velocity or slip rate, and θ is a state variable with the physical interpretation of the fractional contact area that is associated with time dependent creep (Linker and Dieterich, 1992). It is also related to the age of asperity contacts. The parameter a is an experimentally derived parameter, v_* is a normalizing velocity, and μ_* is a constant appropriate for steady-state at velocity v_*, d_c is the characteristic sliding distance required to replace the old contact population with a new one, b is a constitutive

parameter, and α is a scaling factor. The slip velocity and state dependence is complex in natural fault zones and sensitive to changes in loading conditions. A sudden increase in loading causes a sudden increase in slip velocity, which in turns results in accelerated seismic slip or a stick-slip instability (Brace and Byerlee, 1966; Scholz, 1998).

On a discrete level, zero dimensional spring-slider models of frictional slip provide insights into the stability of rate-and-state faults (Ruina, 1983; Rice and Tse, 1986; Ranjith and Rice, 1999). Some spring-slider models consider normal stress variations by inclining the spring at an angle with respect to the sliding surface and by incorporating periodic loading (Dieterich and Linker, 1992; He et al., 1998; Perfettini et al., 2001; Perfettini and Schmittbuhl, 2001). Others include an evolution of effective normal stress in a fluid infiltrated fault via shear-induced dilatancy and pore compaction of gouge materials (Segall and Rice, 1995; Iverson, 2005). None of these models, however, address the poroelastic coupling with the rock mass surrounding the fault—an effect that likely plays a causal role in the occurrence of induced earthquakes.

On a continuum scale, modeling of steady sliding between elastic materials using rate-and-state friction gives insights into earthquake nucleation and propagation of rupture fronts. Previous studies analyzed the linearized response of frictional sliding between identical materials to anti-plane and in-plane perturbations of steady-state sliding, and derived analytical criteria for the onset of the instability (Rice et al., 2001; Bar-Sinai et al., 2013). Previous studies also considered frictional sliding along an interface between elastically or geometrically dissimilar materials, where spatially inhomogeneous slip is coupled to normal stress variations (Rice et al., 2001; Shlomai et al., 2020; Aldam et al., 2017, 2016). Sliding in this case was found to be especially susceptible to a type of an instability, called slip-pulses, regardless of the frictional law or parameters. Others examined the role of heterogeneity in frictional properties in earthquake nucleation (Ray and Viesca, 2017; Luo and Ampuero, 2018)—an aspect that is relevant to spatially complex fault zones in nature (Blanpied et al., 1991; Scholz, 1988). Only one study so far considered the stability of sliding between poroelastic materials with rate-and-state friction (Heimisson et al., 2019), with a

focus on the slip-induced poroelastic effects on the occurrence of slow slip-pulses. This study, however, did not address the fluid injection-induced poroelastic effects on the occurrence or energy partitioning of induced earthquakes—a major focus of this thesis.

Chapter 2

Understanding rate effects in induced earthquakes

The occurrence of induced earthquakes of large magnitude has motivated development of different operational strategies for seismic hazard mitigation. In particular, an early attempt to control seismicity at the Rangely oil field suggested maintaining the magnitude of fluid pressure below a critical threshold (Raleigh et al., 1976), based on a Mohr-Coulomb failure model that links the magnitude of fluid pressure to the occurrence of induced earthquakes (Hubbert and Rubey, 1959). This model, however, does not address the evolution of the rupture and whether a fault slips seismically or aseismically. It was also insufficient to explain seismicity at Cogdell oil field, for instance, where earthquakes were observed in regions of low rather than high fluid pressure (Davis and Pennington, 1989). A different strategy to control seismicity involved maintaining the cumulative volume of injected fluid below a critical threshold (Hofmann et al., 2019), based on empirical observations and modeling linking the cumulative volume of injected fluid to the maximum magnitude of induced earthquakes (McGarr, 2014). This model, however, is at odds with the 2017 Pohang earthquake, as its magnitude exceeded the size estimated from the injected volume by 500 times (Lee et al., 2019).

A growing number of field observations suggests that fluid injection rate is linked to the occurrence of induced earthquakes. It is observed that low-rate wells, for

instance, are much less likely to be associated with earthquakes than high-rate wells, and that the critical rate above which earthquakes are induced is likely dependent on reservoir properties (Frohlich, 2012; Weingarten et al., 2015). It is also observed that temporal variation in injection rates is generally correlated with the frequency of earthquakes (Healy et al., 1968; Improta et al., 2015; Langenbruch and Zoback, 2016; Barbour et al., 2017), and that abrupt increases in injection rates tend to shortly precede the occurrence of earthquakes (Cuenot et al., 2008; Kim, 2013; Tang et al., 2018).

Here we develop a poroelastic model of induced earthquakes in the manner of spring–sliders (Byerlee, 1970; Ruina, 1983; Rice and Tse, 1986; Segall and Rice, 1995; Iverson, 2005) based on rate-and-state friction (Dieterich, 1979a; Ruina, 1983), and we study the effect of injection rate on stick-slip frictional behavior—the mechanism for earthquakes (Brace and Byerlee, 1966).

2.1 Spring-poroslider model

When fluid is injected into a faulted reservoir, the pore pressure change induces effective stress variations in the reservoir and surrounding rock (Fig. 2-1A). To model the effects of variations in effective normal stress on a creeping fault segment, we develop a poroelastic spring–slider model of frictional slip (Fig. 2-1B). Our model consists of a slider of unit base area that is pulled by a spring whose end is constrained to move at a steady slip rate. The spring stiffness accounts for the elastic interaction of the sliding surface with the surrounding rock. The slider represents the injection-driven deformation process, where a piston is loaded vertically and compresses a spring inside a fluid-filled space. The vertical spring is analogous to the rock skeleton, while the fluid inside the slider represents fluid in the rock pores subject to increase from fluid injection and decrease from pressure diffusion. Our model accounts for the poroelastic coupling between the shear and effective normal stresses along the fault.

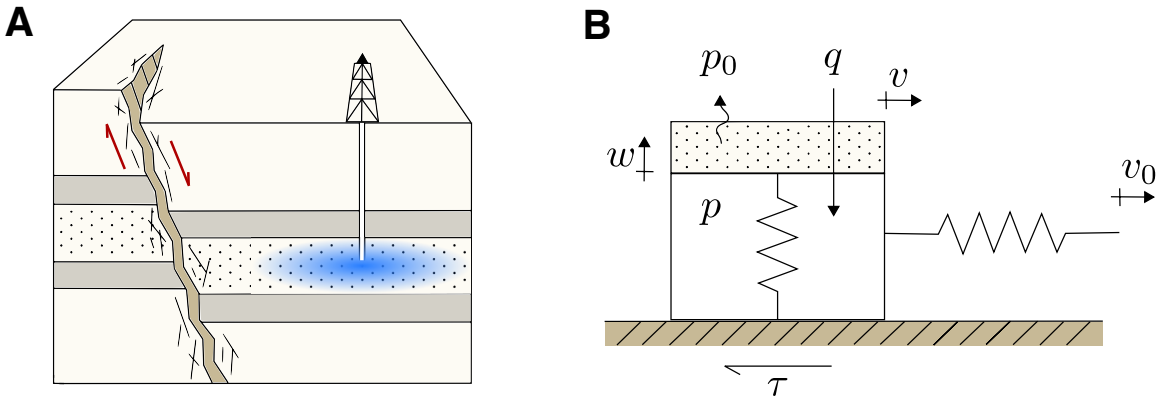

Figure 2-1: Conceptual picture of induced seismicity including poroelastic effects.

2.1.1 Frictional evolution

Frictional evolution is modeled by the rate-and-state constitutive laws, which are capable of reproducing a wide range of observed seismic and interseismic fault behaviors ranging from preseismic slip and earthquake nucleation to coseismic rupture and earthquake after slip (Dieterich, 1979a,b; Ruina, 1983; Marone, 1998). These laws propose that frictional shear stress τ can be described as

$$\tau = \mu(V, \Theta)\Sigma', \tag{2.1}$$

where Σ' is the effective normal stress (the difference between total normal stress and pore pressure), μ is the coefficient of friction, V is the slider's velocity or slip rate, and Θ is a state variable with the physical interpretation of the fractional contact area that is associated with time dependent creep (Linker and Dieterich, 1992). It is also related to the age of asperity contacts.

We adopt Ruina's (Ruina, 1983) slip law for the coefficient of friction because it fits experimental data at variable normal stress better than Dieterich's (Dieterich, 1979a) aging law (Richardson and Marone, 1999),

$$\mu(V, \Theta) = \mu_* + \hat{a} \ln \frac{V}{V_*} + \Theta, \tag{2.2}$$

where $\hat{a}$ is an experimentally derived parameter, V_* is a normalizing velocity, and

μ_* is a constant appropriate for steady-state at velocity V_*. Laboratory experiments on dry rocks show that a step change in normal stress results in a sudden change in the coefficient of friction followed by a displacement-dependent decay back toward the initial steady-state value (Olsson, 1988; Linker and Dieterich, 1992; Wang and Scholz, 1994; Kilgore et al., 2012). Linker and Dieterich (Linker and Dieterich, 1992) interpret this as due to a normal stress effect on the state variable and propose to model the magnitude of the sudden change as $\hat{\alpha}\dot{\Sigma}/\Sigma$. Although the model is based on step test experiments, it captures, at least qualitatively, the pressurization-weakening effect on the coefficient of friction observed from ramping experiments by Olsson (Olsson, 1988). He performed laboratory tests in which the normal stress was increased at constant rate while the load point speed was held constant. He found that shear stress is a function of the normal stress rate. When the normal stress rate was increased by 10 during steady sliding, the rate of increase of shear stress with normal stress (coefficient of friction) decreased by a factor of two—a significant effect.

Here, we combine the proposed state evolution model with the effective stress principle to get

$$\dot{\Theta} = -\frac{V}{d_{\mathrm{c}}}(\Theta + \hat{b}\ln\frac{V}{V_*}) - \hat{\alpha}\frac{\dot{\Sigma}'}{\Sigma'}, \tag{2.3}$$

where d_{c} is the characteristic sliding distance required to replace the old contact population with a new one, $\hat{b}$ is a constitutive parameter, and $\hat{\alpha}$ is a scaling factor. Theoretical and laboratory studies for a sudden change in normal stress show that $\hat{\alpha}$ ranges from 0 to μ (Linker and Dieterich, 1992; Perfettini et al., 2001; Hong and Marone, 2005), but more studies are needed to determine the value of $\hat{\alpha}$ for a gradual change in normal stress. From momentum balance of forces acting on the slider, the equations of motion of the system evolution at variable effective normal stress become

$$\dot{U} = V_0 - V, \tag{2.4}$$

$$\dot{V} = \frac{1}{(T/2\pi)^2}\left[U - \frac{1}{k_{\mathrm{s}}}\mu(V,\Theta)\Sigma'\right], \tag{2.5}$$

where $T = 2\pi\sqrt{m/k_{\mathrm{s}}}$ is the vibration period of the analogous freely slipping system

(Rice and Tse, 1986).

2.1.2 Poroelastic coupling

To obtain a physical evolution of effective stress on the frictional surface, we couple it with a poroelastic model of pore pressure and rock deformation. Starting with the principle of mass conservation, we specify the change of mass from fluid diffusion to be Δm_{diff}, mass accumulation due to rock expansion or fluid compressibility $\frac{\partial}{\partial t}(\rho V_{\text{f}})\Delta t$, and injection source term to be $\tilde{Q}\Delta t$. We assume that both the fluid and rock matrix are compressible (Wang, 2000), and so mass balance leads to

$$\Delta m_{\text{diff}} = \frac{\partial(\rho V_{\text{f}})}{\partial t}\Delta t - \tilde{Q}\Delta t, \tag{2.6}$$

where the change in fluid mass due to pressure diffusion can be written using Darcy's law as

$$\Delta m_{\text{diff}} = -\frac{\rho k A(P - P_0)}{\eta L}\Delta t, \tag{2.7}$$

where η is fluid dynamic viscosity, k is permeability, and L is the pressure diffusion length. The mass accumulation term can be expressed as

$$\frac{\partial}{\partial t}\rho V_{\text{f}}\Delta t = \frac{\partial}{\partial t}\rho(P)HA\Delta t = \frac{\partial}{\partial t}(\rho_0(1 + c_{\text{f}}(P - P_0))(H_0 + W)A\Delta t, \tag{2.8}$$

where H is the current height of the slider, ρ_0 is the initial fluid density, c_{f} is fluid compressiblity, H_0 is the initial height of the slider, and W is the position of the piston. When fluid is injected into a rock that is free to deform in the direction orthogonal to sliding, the addition of mass induces an increase of volume equivalent to

$$V_{\text{f}} - V_{\text{f},0} = AW, \tag{2.9}$$

where $V_{\mathrm{f},0}$ is the initial fluid volume. We then derive an expression for rock deformation W from force balance, while using the convention of compression positive,

$$W = \frac{A}{k_{\mathrm{n}}}(\Sigma_0' - \Sigma + P), \tag{2.10}$$

where k_{n} is the normal spring stiffness and Σ_0' is the initial effective stress. We further approximate the mass accumulation term to

$$\rho\frac{\partial}{\partial t}[AH]\Delta t + AH\frac{\partial P}{\partial t}\Delta t = \rho\frac{A}{k_{\mathrm{n}}}\frac{\partial P}{\partial t}\Delta t + H\frac{\rho_0}{\rho}c_{\mathrm{f}}\frac{\partial P}{\partial t}\Delta t \approx \rho\frac{A}{k_{\mathrm{n}}}\frac{\partial P}{\partial t}\Delta t + H_0 c_{\mathrm{f}}\frac{\partial P}{\partial t}\Delta t. \tag{2.11}$$

Note that we consider that the total stress Σ is analogous to overburden stress in the earth, and is therefore constant in time. By substituting Eqs. (2.7)-(3.1) into Eq. (2.6), we find that pore pressure satisfies a diffusion equation that leads to transient behavior at early times and steady-state behavior at late times

$$\dot{P} = \frac{k_{\mathrm{n}}^{\mathrm{eff}}k}{\eta LA}(P_0 - P) + \frac{k_{\mathrm{n}}^{\mathrm{eff}}}{A}Q, \tag{2.12}$$

where η is fluid dynamic viscosity ($\eta = \nu\rho$), Q is the volumetric injection rate per unit area ($Q = \tilde{Q}/\rho A$), and $k_{\mathrm{n}}^{\mathrm{eff}} = (1/k_{\mathrm{n}} + c_{\mathrm{f}}H_0/A)^{-1}$ is an effective stiffness somewhat equivalent to the uniaxial bulk modulus or the reciprocal of the uniaxial specific storage per diffusion length in a continuum (Wang, 2000). Since the slider has a unit base area ($A = 1$), the evolution of the pore pressure as a result of fluid injection follows

$$\dot{P} = \frac{k_{\mathrm{n}}^{\mathrm{eff}}k}{\eta L}(P_0 - P) + k_{\mathrm{n}}^{\mathrm{eff}}Q. \tag{2.13}$$

2.1.3 Governing equations

The dimensional equations describing the dynamic motion of the poroelastic spring–slider system with an evolving pore pressure take the form:

$$\dot{U} = V_0 - V, \tag{2.14}$$

$$\dot{V} = \frac{1}{(T/2\pi)^2}\left[U - \frac{1}{k_\mathrm{s}}(\mu_* + \hat{a}\ln\frac{V}{V_*} + \Theta)(\Sigma - P)\right], \tag{2.15}$$

$$\dot{\Theta} = -\frac{V}{d_\mathrm{c}}(\Theta + \hat{b}\ln\frac{V}{V_*}) + \hat{\alpha}\frac{\dot{P}}{(\Sigma - P)}, \tag{2.16}$$

$$\dot{P} = \frac{k_\mathrm{n}^\mathrm{eff} k}{\eta L}(P_0 - P) + k_\mathrm{n}^\mathrm{eff} Q. \tag{2.17}$$

where U is the relative displacement between the load point and the slider, $\dot{(\,)}$ denotes time derivative, V_0 is the loading velocity, V is slip rate, T is the vibration period, k_s is the shear stiffness, V_* is a normalizing slip rate, μ_* is a constant appropriate for steady-state at slip rate V_*, $\hat{a}$ and $\hat{b}$ are experimentally derived parameters relating friction to changes in slip rate and state, respectively, Θ is a state variable describing the sliding surface, Σ is the total stress, P is the pressure inside the slider (pore pressure), d_c is the characteristic slip distance, $\hat{\alpha}$ is a scaling factor ranging from 0 to μ (Linker and Dieterich, 1992; Kilgore et al., 2012), $k_\mathrm{n}^\mathrm{eff}$ is the effective normal stiffness (related to the uniaxial bulk modulus or the reciprocal of the uniaxial specific storage per diffusion length in a continuum), k is the permeability, η is fluid dynamic viscosity, L is the pressure diffusion length, P_0 is the ambient pressure, and Q is the volumetric injection rate per unit area.

Choosing the following characteristic quantities: $u_\mathrm{c} = d_\mathrm{c}$, $v_\mathrm{c} = V_*$, $\mu_\mathrm{c} = \mu_*$, $p_\mathrm{c} = P_0$, $\tau_\mathrm{c} = \mu_*(\Sigma - P_0)$, $\theta_\mathrm{c} = \mu_*$, and $t_\mathrm{c} = d_\mathrm{c}/V_*$, the equations describing the

dynamic motion of the system, in dimensionless form, become:

$$\dot{u} = v_0 - v, \tag{2.18}$$

$$\dot{v} = \frac{1}{\epsilon^2}\left[u - \frac{1}{\kappa}(1 + a\ln v + \theta)(\sigma - p)\right], \tag{2.19}$$

$$\dot{\theta} = -v(\theta + b\ln v) + \alpha\frac{\dot{p}}{(\sigma - p)}, \tag{2.20}$$

$$\dot{p} = c(p_0 - p) + rq, \tag{2.21}$$

where $\kappa = (k_s d_c)/\tau_c$, $a = \hat{a}/\mu_c$, $b = \hat{b}/\mu_c$, $\alpha = \hat{\alpha}/\mu_c$, $\epsilon = (T/2\pi)/t_c$, $c = t_c/(\eta L/k_n^{\text{eff}}/k)$, $r = t_c k_n^{\text{eff}}$, and $q = Q/p_c$. The parameter κ is the normalized shear stiffness, and a, b, α are normalized frictional parameters. The parameter ϵ is the normalized oscillation period or ratio of inertial to state-evolution timescales, which may range from 10^{-8} to 10^{-6} depending on rupture diameter and shear wave speed. The parameter c is the normalized diffusivity or ratio of the pore-pressure to the state-evolution timescales, which may range from 10^{-4} to 10^{1} depending on reservoir permeability, uniaxial bulk modulus, and well-fault distance. The parameter rq is the normalized injection rate, which may range from 10^{-5} to 10^{-1} depending on injection rate and reservoir size.

2.2 Linear stability analysis

The stability of steady frictional sliding to small perturbations in velocity, which determines whether motion is by slow steady-sliding or violent stick-slip, depends on the evolution of the frictional resistance. Stick-slip occurs whenever a change of frictional resistance with sliding occurs at a rate greater than the loading system is capable of following (Byerlee, 1970). At a constant pore pressure, linear stability analysis of the system about steady-state leads to the stability condition by Ruina (1983). Pore pressure, however, is not constant in time and its evolution depends on the injection rate and on the poroelastic and hydraulic parameters of the rupture. To quantify this, we carry out a linear stability analysis of the system about a quasi

steady-state where sliding is steady but pore pressure is evolving as a result of fluid injection.

The equations describing the quasi-static motion of the spring–poroslider system evolving at variable pore pressure p, in dimensionless form, are

$$\dot{u} = v_0 - v, \tag{2.22}$$

$$0 = (\sigma - p)\mu(v, \theta) - \kappa u, \tag{2.23}$$

$$\dot{\theta} = -v(b \ln v + \theta) + \alpha \frac{\dot{p}}{(\sigma - p)}. \tag{2.24}$$

The quasi-steady-state values of the variables are $v_{\rm qss} = v_0$ and $\theta_{\rm qss} = \alpha\dot{p}/(\sigma - p)/v_0 - b \ln v_0$. Linearizing Eqs. (2.22)–(2.24) about the quasi-steady-state, and then taking the time derivative of Eq. (2.23), yields

$$\Delta\dot{v} = \frac{v_0}{a}\left[b + \frac{\alpha}{v_0}\frac{\dot{p}}{(\sigma - p)} - \frac{\kappa}{(\sigma - p)}\right]\Delta v + \frac{v_0^2}{a}\Delta\theta, \tag{2.25}$$

$$\Delta\dot{\theta} = -\left[b + \frac{\alpha}{v_0}\frac{\dot{p}}{(\sigma - p)}\right]\Delta v - v_0\Delta\theta. \tag{2.26}$$

Equations (2.25)–(2.26) represent a 2×2 system of autonomous linear ODEs with solutions of the form $\Delta v = Ve^{\lambda t}$, $\Delta\theta = \Theta e^{\lambda t}$, where λ is the growth rate and t is time. Substituting these forms into the linearized equations (2.25)–(2.26) yields the characteristic equation

$$a(\sigma - p)\lambda^2 + (-\alpha\dot{p} + \kappa v_0 - (b - a)(\sigma - p)v_0)\lambda + \kappa v_0^2 = 0. \tag{2.27}$$

If the real part of the roots $\lambda_{\rm i}$ are negative for all i, perturbations from the quasi-steady-state are damped and the system is stable. If the real part of the roots $\lambda_{\rm i}$ are positive for some i, then perturbations grow exponentially and the system is unstable. At $\Re(\lambda_{\rm i}) = 0$, we find that the dimensionless critical stiffness is

$$\kappa_{\rm crit} = (b - a)(\sigma - p) + \frac{\alpha}{v_0}\dot{p}. \tag{2.28}$$

So, motion is by stick-slip when the dimensionless shear stiffness of the loading system is lower than a critical value ($\kappa < \kappa_{\text{crit}}$) given by

$$\kappa_{\text{crit}} = (b - a)(\sigma - p) + \frac{\alpha}{v_0}\dot{p}, \tag{2.29}$$

and is by steady-sliding otherwise ($\kappa > \kappa_{\text{crit}}$). Variables p and $\dot{p}$ are dimensionless pore pressure magnitude and pore pressure rate, respectively, at any point in time. Accordingly, frictional instability for the spring–poroslider system with an evolving pore pressure depends not only on the magnitude of pore pressure, but also on the rate of change of pore pressure.

As pore pressure evolves from initial to steady-state conditions in response to fluid injection, we find that the competing effects of p and $\dot{p}$ exhibit a transition in their dominance over frictional instability (Fig. 2-2A). The destabilizing effect of $\dot{p}$ dominates when pore pressure grows rapidly at early times, resulting in an increase in critical stiffness (dashed curve in Fig. 2-2A). It then decreases as pore pressure diffuses and approaches steady state, giving rise to the stabilizing effect of p, which explains the decrease in critical stiffness at late times (dotted curve in Fig. 2-2A). This result is generally consistent with a linear stability analysis of slow slip with mildly rate-strengthening friction in a poroelastic continuum (Heimisson et al., 2019), in which undrained slip-induced poroelastic pressure has a destabilising effect and a sufficiently fast equilibration process has a stabilizing effect. In our analysis, the early-time destabilizing effect of $\dot{p}$ is likely attributed to a short-term effect on contact interlocking, where a decrease in effective normal stress results in fault opening and loss of asperity contacts (Wang and Scholz, 1994). The late-time stabilizing effect of p, in contrast, is likely attributed to a long-term effect on interface locking. A low effective normal stress tends to reduce the degree of interface locking, and thus limit the magnitude of stress drops (Moreno et al., 2010; Kitajima and Saffer, 2012; Segall et al., 2010).

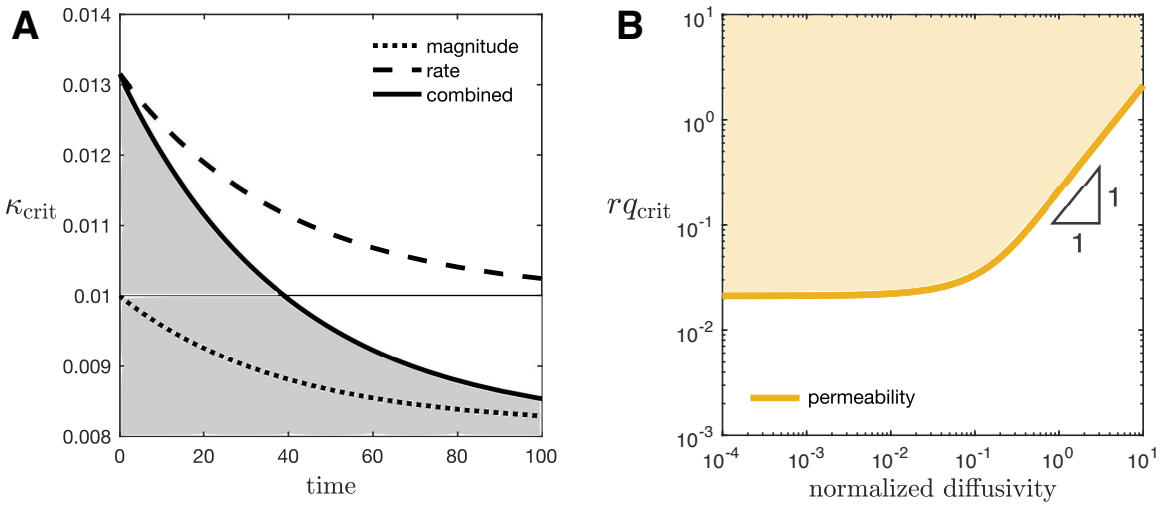

Figure 2-2: Dimensionless critical stiffness and critical injection rate.

This behavior is also qualitatively consistent with laboratory observations of sliding between saturated rocks at both transient and steady-state pore pressure conditions. The early-time destabilizing effect agrees with an experimental study showing that a gradual increase in pore pressure results in unstable slip during the transient-state, and that the degree of instability measured by the total slip, slip rate, and shear stress drop correlates with the rate of effective normal stress reduction (French et al., 2016). The late-time stabilizing effect also agrees with another experimental study, showing that sliding between two rock surfaces is much more stable at high than at low steady-state pore pressure (Byerlee and Brace, 1972). Sliding is observed to be by slow, steady-type motion at high pore pressure, and by stick-slip at low pore pressure. This behavior, however, is different from the observations of shearing granular fault gouge materials (Sawai et al., 2016; Scuderi and Collettini, 2016), where the frictional parameter $(b-a)$ is observed to decrease in magnitude with increasing steady-state pore pressure, an effect related to shear-induced dilatancy strengthening and pore compaction creep.

2.2.1 Quasi-steady-state approximation

The quasi-steady-state approximation, in general, is an approach to simplify dynamic systems of ordinary differential equations with an initial fast transient, after which

some of the dependent variables can be assumed to be in steady-state with regard to the other slowly evolving dependent variables (Segel and Slemrod, 1989). In particular, the QSSA is a good approach to use in our analysis because it allows us to study the stability of steady frictional sliding to small perturbations in velocity while pore pressure is evolving. The sliding velocity and the velocity-dependent part of the state variable are in steady state with respect to the pore pressure. Here, we analyze the QSSA in the context of singular perturbation theory following the analysis by Segel and Slemrod (1989), identify the small parameter(s) necessary for the validity of the QSSA, and quantify the error associated with it.

Reduced dimensional equations

As shown earlier, the dynamics of our poroelastic spring-slider model is governed by a system of four coupled nonlinear ODEs. Under quasi-static loading, velocity is the fastest evolving variable of the system and it responds instantaneously (negligible inertia) to small perturbations. Thus we can focus our analysis on a reduced system of ODEs at steady-state velocity $V = V_0$,

$$\dot{\Theta} = -\frac{V_0}{d_c}(\Theta + \hat{b} \ln \frac{V_0}{V_*}) + \hat{\alpha}\frac{\dot{P}}{\Sigma - P}, \tag{2.30}$$

$$\dot{P} = \frac{k_n^{\text{eff}} k}{\eta L}(P_0 - P) + k_n^{\text{eff}} Q, \tag{2.31}$$

with initial conditions

$$\Theta(0) = 0, \tag{2.32}$$

$$P(0) = P_0. \tag{2.33}$$

Timescales

As a first step in the analysis, we estimate the fast timescale t_Θ of the pre-steady-state period and the slow timescale t_P for the evolution of pore pressure. To estimate t_Θ we make the approximation $P \approx P_0$ in Eq. (2.30). The solution for the state variable

becomes

$$\Theta(t) = \bar{\Theta}(e^{-\frac{V_0}{d_c}t} - 1), \tag{2.34}$$

where $\bar{\Theta} = \hat{b} \ln V_0/V_* - \hat{\alpha}(d_c/V_0)(\dot{P}_0/(\Sigma - P_0))$. Subsequently, we take

$$t_\Theta = \frac{d_c}{V_0}. \tag{2.35}$$

Since the pore pressure evolution is independent of the evolution of the state variable Θ, we estimate t_P by solving Eq. (2.31) with the initial condition $P(0) = P_0$ to obtain

$$P(t) = P_0 + \frac{\eta L}{k} Q(1 - e^{-\frac{k_n^{\text{eff}} k}{\eta L}t}). \tag{2.36}$$

Similarly, we take

$$t_P = \frac{\eta L}{k_n^{\text{eff}} k}. \tag{2.37}$$

Scaled dimensionless equations

During the pre-steady-state, it is reasonable to scale time by t_Θ, where the dimensionless time τ is given by

$$\tau = \frac{t}{t_\Theta}. \tag{2.38}$$

Thus, the scaled dimensionless governing equations become

$$\frac{\partial \theta}{\partial \tau} = -v_0(\theta + b \ln v_0) + \frac{\alpha}{\sigma - p}\frac{\partial p}{\partial \tau}, \tag{2.39}$$

$$\frac{\partial p}{\partial \tau} = \frac{t_\Theta}{t_P}(p_0 - p) + t_\Theta q, \tag{2.40}$$

with initial conditions

$$\theta(0) = 0, \tag{2.41}$$

$$p(0) = p_0, \tag{2.42}$$

where we have defined $b = \hat{b}/\mu_0$, $\alpha = \hat{\alpha}/\mu_0$, and $q = Q/p_0$. After the pre-steady

state, the QSSA is assumed to be valid and t_{P} becomes a reasonable timescale. We introduce a new dimensionless scaled time T by

$$T = \frac{t}{t_{\mathrm{P}}}, \tag{2.43}$$

with which the scaled dimensionless governing equations become

$$\frac{t_\Theta}{t_{\mathrm{P}}}\frac{\partial \theta}{\partial T} = -v_0(\theta + b\ln v_0) + \frac{t_\Theta}{t_{\mathrm{P}}}\frac{\alpha}{\sigma - p}\frac{\partial p}{\partial T}, \tag{2.44}$$

$$\frac{\partial p}{\partial T} = (p_0 - p) + t_{\mathrm{P}} q. \tag{2.45}$$

Singular perturbation

Approximate solutions can now be obtained by methods of singular perturbation theory (Lin and Segel, 1988), for $0 < t_\Theta/t_{\mathrm{P}} \ll 1$. A solution of Eqs. (2.39)-(2.40) is obtained of the form

$$\theta(\tau) = \theta^{(0)}(\tau) + \frac{t_\Theta}{t_{\mathrm{P}}}\,\theta^{(1)}(\tau) + ..., \tag{2.46}$$

$$p(\tau) = p^{(0)}(\tau) + \frac{t_\Theta}{t_{\mathrm{P}}}\,p^{(1)}(\tau) + ..., \tag{2.47}$$

where

$$\theta^{(0)}(\tau) = \bar{\theta}(e^{-\tau} - 1), \tag{2.48}$$

$$p^{(0)}(\tau) = p_0. \tag{2.49}$$

Similarly, the solution of Eqs. (2.44)-(2.45) obtained of the form

$$\theta(T) = \theta_0(T) + \frac{t_\Theta}{t_{\mathrm{P}}}\,\theta_1(T) + ... \,, \tag{2.50}$$

$$p(T) = p_0(T) + \frac{t_\Theta}{t_{\mathrm{P}}} p_1(T) + ... \,, \tag{2.51}$$

where

$$\theta_0 = -b \ln v_0 + \frac{\alpha}{v_0} \frac{t_\Theta q}{\sigma - p_0}, \tag{2.52}$$

$$\frac{\partial p_0}{\partial T} = t_\mathrm{P} q. \tag{2.53}$$

Note that Eqs. (2.52)-(2.53) are associated with initial conditions Eqs. (2.32)-(2.33), and represent the initial state about which we linearized the spring-poroslider system (section 3). The results of this analysis remain valid for general initial conditions $\Theta(0) = \Theta_\mathrm{i}$ and $P(0) = P_\mathrm{i}$ (Segel and Slemrod, 1989), where Θ_i ranges from 0 to Θ_ss and P_i ranges from P_0 to P_ss. Linearizing the spring-poroslider system about the true steady-state, where

$$\theta_0 = -b \ln v_0, \tag{2.54}$$

$$\frac{\partial p_0}{\partial T} = 0, \tag{2.55}$$

thus yields the Ruina (1983) stability condition (Ruina, 1983).

QSSA validity conditions

A necessary aspect of the QSSA is that the duration of the pre-steady-state period is much shorter than the characterstic time for the pore pressure evolution. An essential condition for the QSSA to be valid after the pre-steady state is therefore $t_\Theta \ll t_\mathrm{P}$,

$$0 < c = \left(\frac{d_\mathrm{c}}{V_0}\right) \Big/ \left(\frac{\eta L}{k_\mathrm{n}^\mathrm{eff} k}\right) \ll 1. \tag{2.56}$$

Note that the initial condition $P(0) = P_0$ is reasonable for the QSSA only if there is a negligible relative change $|\Delta P/P_0|$ in pore pressure during the pre-steady state. We estimate $|\Delta P/P_0|$ by

$$\left|\frac{\Delta P}{P_0}\right| \approx \frac{1}{P_0} \left|\frac{\partial P}{\partial t}\right|_\mathrm{max} t_\Theta. \tag{2.57}$$

An additional condition for the validity of the QSSA is therefore

$$0 < rq = \frac{d_c k_n^{eff}}{V_0} \frac{Q}{P_0} \ll 1. \tag{2.58}$$

Recall that parameter c is the normalized diffusivity or ratio of the pore pressure to the state evolution timescales and parameter rq is the normalized injection rate, where $r = t_\Theta k_n^{eff}$ and $q = Q/P_0$.

Error estimates

This analysis shows that using the QSSA to study the stability of steady frictional sliding to small perturbations in velocity with an evolving pore pressure is justified when conditions Eqs. (2.56) and (2.58) are met. In other words, if in a timescale t_Θ sliding reaches steady state with a constant pore pressure, then assuming that sliding is in a quasi-steady state with a changing pore pressure is valid when the pore pressure change occurs on a time scale t_P that is long compared to t_Θ and $\Delta P|_{t_\Theta}$ is small compared to P_0.

Therefore, we expect that the accuracy of our instability criterion depends on dimensionless parameters c and rq. Here we evaluate the error in the analytical estimate of the critical stiffness required to trigger the first slip event (Figure 2-3). We indeed find that the error decreases as c or rq decrease. It becomes small ($< 15\%$) when the normalized diffusivity and normalized injection rate reach small values ($c \leq 5 \times 10^{-2},\ rq \leq 5 \times 10^{-3}$). It is also interesting to note that the QSSA validity may be extended to instances where c is of order one provided that rq is significantly smaller than one (green curve).

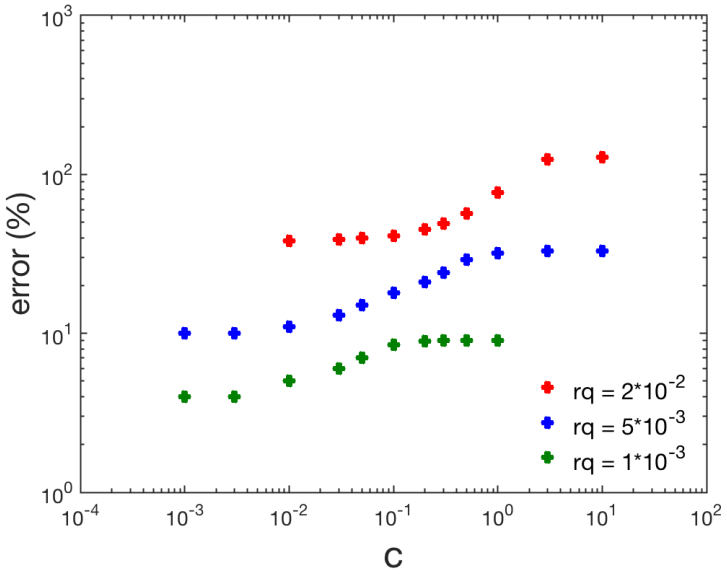

Figure 2-3: Error in the instability criterion as a function of normalized diffusivity and injection rate.

2.2.2 Validation against nonlinear simulations

To validate our analytical instability criterion (Eq. (2.28)), we simulate the fully dynamic equations of motion of the spring–poroslider system (Eqs. (2.18)-(2.21)) with the following initial conditions

$$u(t=0) = v_0(\sigma - p_0)(1 + (a-b)\ln v_0)/\kappa, \tag{2.59}$$

$$v(t=0) = v_0, \tag{2.60}$$

$$\theta(t=0) = 0, \tag{2.61}$$

$$p(t=0) = p_0. \tag{2.62}$$

These coupled nonlinear ordinary differential equations are solved in MATLAB using the `ode15s` solver for stiff systems. Representative results of motion without fluid injection and motion while fluid is being injected into the poroslider at a constant rate are shown in Figures 2-4 and 2-5, respectively.

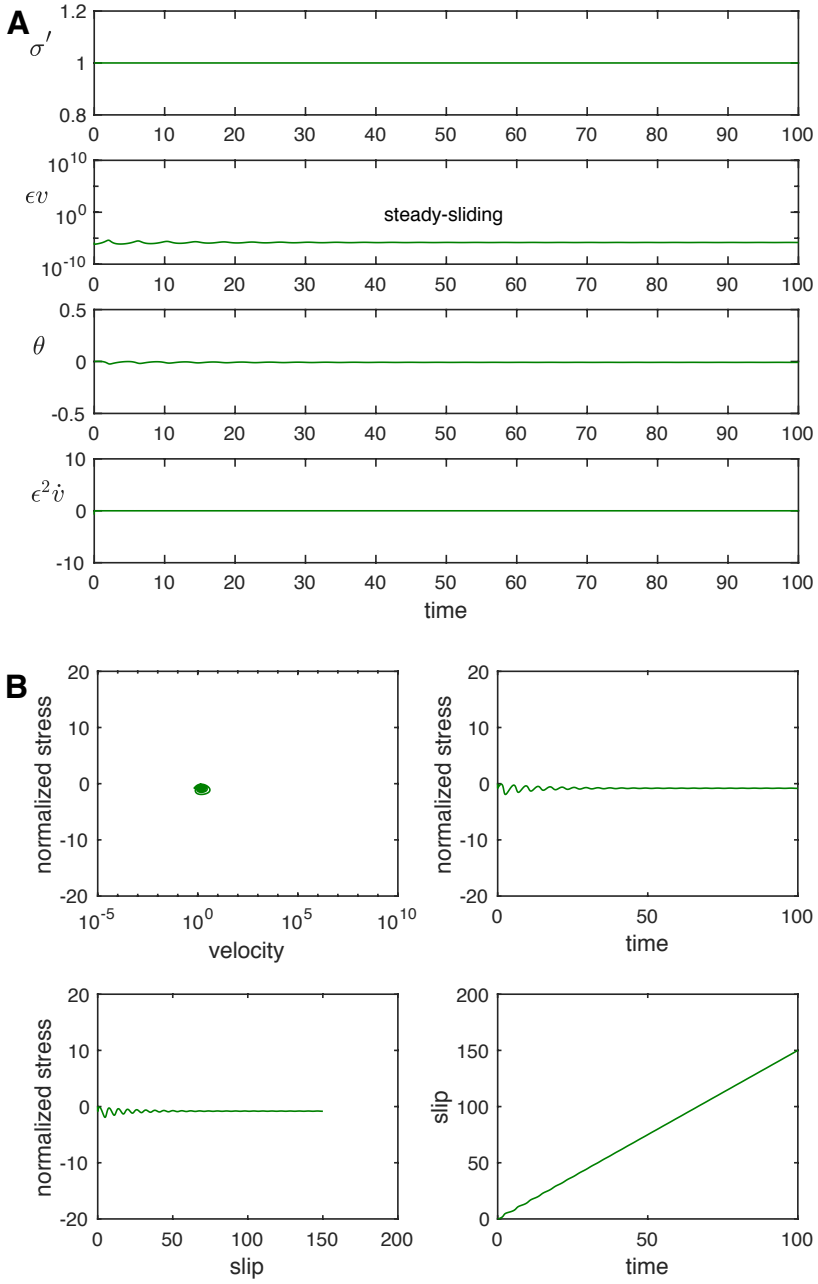

Figure 2-4: Dynamics of the spring-poroslider system without fluid injection, for velocity-weakening friction.

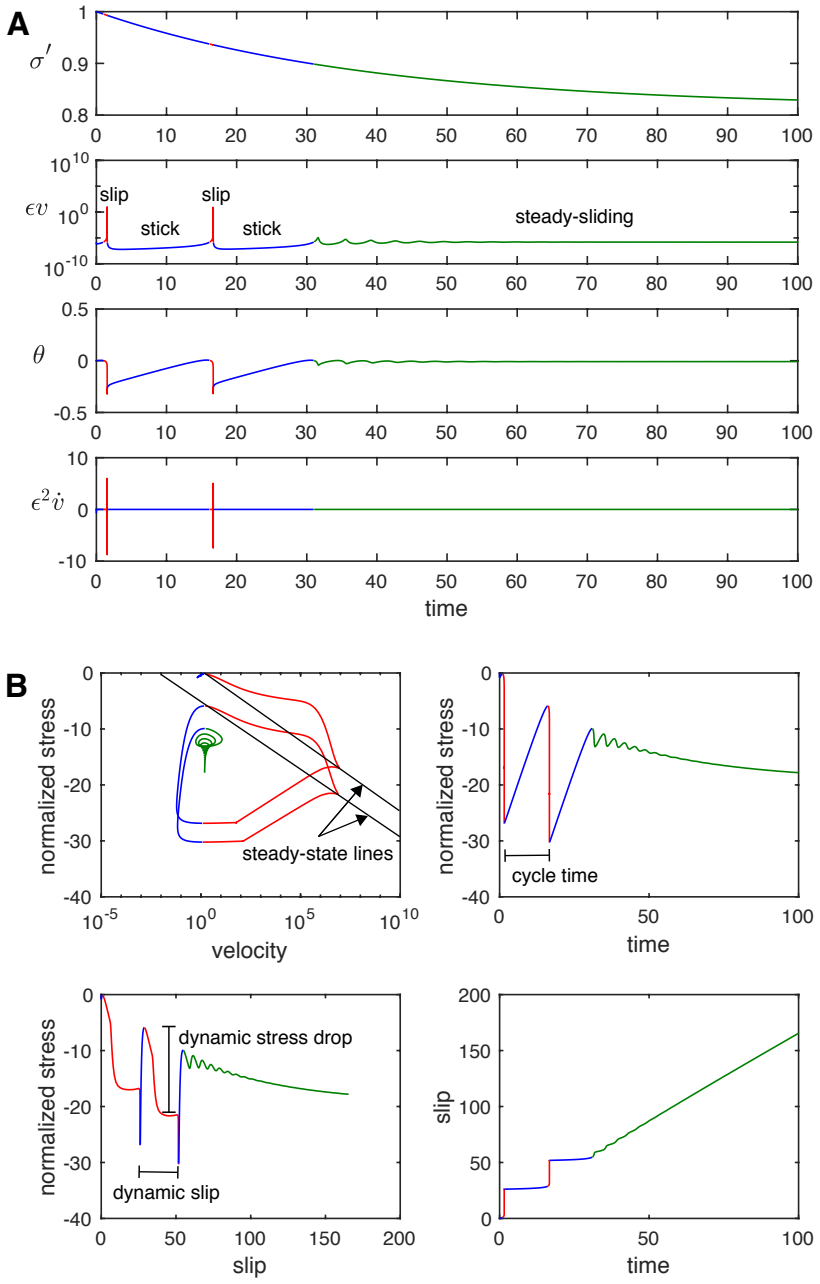

Figure 2-5: Dynamics of the spring-poroslider system under constant fluid injection rate, for velocity-weakening friction.

The simulation without fluid injection is performed using parameter values $a = 0.01$, $b = 0.02$, $\alpha = 1$, $\epsilon = 10^{-6}$, $c = 3 \times 10^{-2}$, and $\kappa = 0.011$. The simulation with fluid injection is performed using the same parameter values along with $rq = 5 \times 10^{-3}$. The poroslider is initially sliding steadily at a fixed loading velocity $v_0 = 1$ and a zero fluid injection rate $q = 0$. It is then made unstable by suddenly increasing the loading velocity to a new fixed value $v_0 = 1.5$ and injecting fluid at a constant rate $q = 10^{-9}$. This triggers two stick-slip events, consisting of a slow build-up followed by a sudden discharge of accumulated stress. The buildup occurs at a nearly stationary state $v \approx 0.1$ over a time period of 15, whereas the discharge is significantly faster reaching a peak velocity $v \approx 10^7$, and has a duration of 0.5 (Fig. 2-5A). Following the two stick-slip events, the poroslider evolves toward steady sliding at a relatively low and constant velocity $v \approx 1.5$.

The normalized stress variations with velocity, slip, and time are shown in Figure 2-5B. Initially, the sudden change in load point velocity and effective normal stress creates an excess of spring force over the frictional resistance, which in turn accelerates the poroslider. The stress drops to a steady state value corresponding to slip velocity. The poroslider continues to slip at a high rate until further shortening of the spring becomes too difficult. It then decelerates to reach a nearly stationary state. During this stage, the stress builds up to a peak value corresponding to stick velocity, and the stick-slip cycle repeats. Note that the cycle is not repeated exactly, the stress buildup after a slip event is dependent on the current effective normal stress. Eventually, the decrease in effective normal stress terminates the stick-slip cycle and initiates an indefinite period of steady-sliding. The stress exhibits decaying oscillations that decrease in amplitude with time.

As a whole, Figure 2-5 shows that the analytical critical stiffness (Eq. (2.28)) is in good qualitative agreement with the numerical simulation results. To validate our instability criterion quantitatively, we compare our instability criterion against estimates obtained empirically from the fully dynamic nonlinear simulations (Fig. 2-6). The analytical estimate (blue) works well when the growth rate of perturbations is large compared to the growth rate of the pore pressure. Initially, when pore pres-

sure grows rapidly, estimates differ slightly, but they become indistinguishable at late times, when pore pressure changes relatively slowly. We suspect that the small difference in estimates at early times is due to, at least partially, the use of the QSSA in our analysis, which we discuss in detail in section 6.

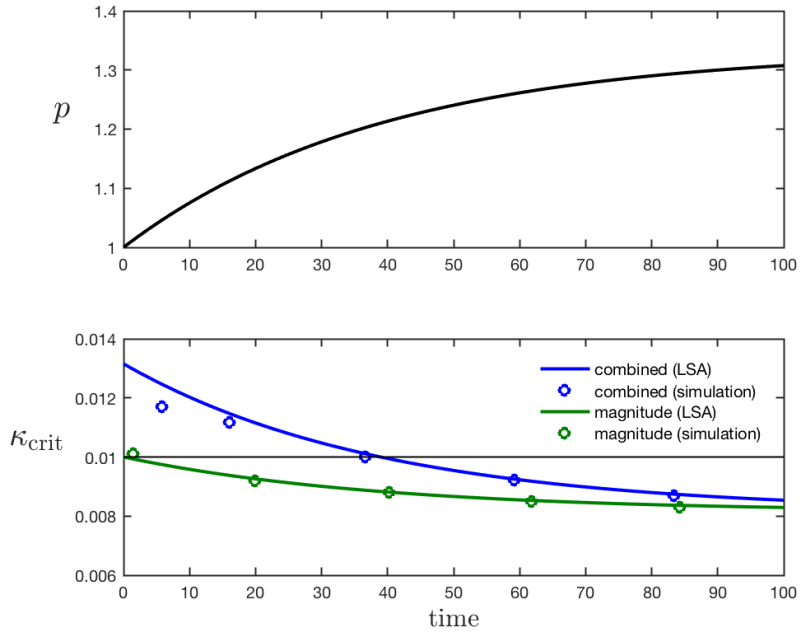

Figure 2-6: Analytical vs. numerical estimates of critical stiffness.

2.3 Application to the Denver earthquakes

Our findings, if they are applicable to natural faults, hold interesting and important implications for induced seismicity. The poroelastic spring-slider may be viewed as a simple model of a fault segment in contact with a reservoir, steady-sliding as an analog of aseismic creep, and stick-slip as a seismic wave-producing rupture cycle (Brace and Byerlee, 1966; Rice and Tse, 1986). Within this view, our findings may be generalized to indicate that a slowly creeping fault segment is destabilized and generates an earthquake if the condition for instability in Eq. (2.29) is met.

To bridge the gap between the analysis of the idealized spring-poroslider model and the real world, we express our instability criterion in dimensional form, and

identify values of dimensionless parameters c and rq that correspond to real-world settings.

In dimensional form, the critical stiffness from the linear stability analysis is

$$k_{\mathrm{s,crit}} = \frac{(\hat{b}-\hat{a})}{d_{\mathrm{c}}}(\Sigma - P) + \frac{\hat{\alpha}}{V_0}\dot{P}, \tag{2.63}$$

or, equivalently,

$$k_{\mathrm{s,crit}} = \left[(\hat{b}-\hat{a}) + \hat{\alpha}\frac{d_{\mathrm{c}}}{V_0}\frac{\dot{P}}{(\Sigma - P)}\right]\frac{(\Sigma - P)}{d_{\mathrm{c}}}, \tag{2.64}$$

where the term $\hat{b}-\hat{a}$ represents the original velocity weakening effect and the dimensionless term $\hat{\alpha}(d_{\mathrm{c}}/V_0)\dot{P}/(\Sigma - P)$ represents an additional weakening effect from fluid pressurization. Note that this pressurization term is maximum at early times and is approximately equal to rq.

The 1960s Denver earthquakes is a good example of a real-world setting, where it is well-documented that injection of wastewater into the fractured Precambrian granite gneiss underneath the Rocky Mountain Arsenal triggered the earthquakes and where injection rate is directly related to the frequency of earthquakes (Evans, 1966; Healy et al., 1968). The reservoir spans a depth interval from 3.7 to 7 km below the surface. Experimental data on granite at this depth shows velocity weakening behavior ($\hat{b}-\hat{a}$ in the range 0.002 to 0.005, $\mu_0 = 0.7$ to 0.75) (Blanpied et al., 1991).

To identify values of dimensionless parameter c that correspond to this setting, we estimate the state evolution timescale t_Θ and the pore pressure evolution timescale t_{p}:

$$c = \frac{t_\Theta}{t_{\mathrm{P}}}. \tag{2.65}$$

The state evolution timescale t_Θ is

$$t_\Theta = \frac{d_c}{V_0}. \tag{2.66}$$

We find that t_Θ ranges from 10 days to 4 months based on field data of the characteristic slip distance and loading rate ($d_{\mathrm{c}} = 10^{-3}$ to 10^{-2} m, $V_0 = 10^{-9}$ m/s) (Scholz,

1988; Marone, 1998).

The pore pressure evolution time scale t_{P} can be transferred from the poroslider model to field settings,

$$t_{\mathrm{P}} = \underbrace{\frac{\eta L}{k_{\mathrm{n}}^{\mathrm{eff}} k}}_{\text{poroslider}} = \frac{L}{k/\eta}\left[\frac{1}{k_{\mathrm{n}}} + H_0 c_{\mathrm{f}}\right] = \frac{L^2}{k/\eta}\left[\frac{1}{K_{\mathrm{v}}} + \phi\frac{1}{K_{\mathrm{f}}}\right] = \frac{L^2}{k/\eta}\frac{S_{\mathrm{s}}}{\rho g} = \underbrace{\frac{L^2 S}{T}}_{\text{field}}. \tag{2.67}$$

We find that t_{P} is approximately 2 years based on a reservoir analysis of the Denver earthquakes, with transmissivity $T = 10^{-5}$ m^2/s, storativity $S = 10^{-5}$, and characteristic length scale $L = 8 \times 10^3$ m (Hsieh and Bredehoeft, 1981).

In a similar manner, we identify values of dimensionless parameter rq. We translate this quantity from the poroslider model to field settings:

$$rq = \underbrace{\frac{d_{\mathrm{c}}}{V_0} k_{\mathrm{n}}^{\mathrm{eff}} \frac{Q}{P_0}}_{\text{poroslider}} = \frac{d_{\mathrm{c}}}{V_0} k_{\mathrm{n}}^{\mathrm{eff}} \frac{Q_{\mathrm{w}}}{P_0 W B} = \frac{d_{\mathrm{c}}}{V_0} \frac{\left[\frac{1}{K_{\mathrm{v}}} + \phi\frac{1}{K_{\mathrm{f}}}\right]^{-1}}{L} \frac{Q_{\mathrm{w}}}{P_0 W B} = \underbrace{\frac{d_{\mathrm{c}}}{V_0} \frac{\rho g}{LS} \frac{Q_{\mathrm{w}}}{P_0 W}}_{\text{field}}, \tag{2.68}$$

and evaluate values based on the reservoir analysis and injection data, with reservoir pressure $P_0 = 30$ MPa, reservoir width $W = 3 \times 10^3$ m, and field injection rate $Q_{\mathrm{w}} = 2$ to 9 million gal/mo (Evans, 1966; Hsieh and Bredehoeft, 1981).

Therefore, reasonable estimates of c and rq for this setting would be in the order of 10^{-2} to 10^{-1} and 10^{-3} to 10^{-1}, respectively. Note that both estimates are much smaller than one, and thus meet the QSSA validity conditions.

Having determined the validity of the QSSA analysis to this setting, we now assess whether pressurization rate effects were likely significant during fluid injection leading to the Denver earthquakes. In dimensionless form, the critical stiffness κ_{crit} is given by Eq. (2.28). Prior to fluid injection, the pore pressure is constant and the critical stiffness,

$$\kappa_{\mathrm{crit}} = (b - a)(\sigma - p_0), \tag{2.69}$$

is estimated to be 0.005 ($b - a = 0.003$ to 0.007, $\sigma - p_0 = 1$). Shortly following the start of fluid injection, the pore pressure increases rapidly and the dimensionless

critical stiffness takes the form:

$$\kappa_{\mathrm{crit}}\Big|_{t=0} = (b-a)(\sigma - p_0) + \frac{\alpha}{v_0}\dot{p}\Big|_{t=0} = (b-a)(\sigma - p_0) + \frac{\alpha}{v_0} rq. \tag{2.70}$$

This results in an increase in critical stiffness at early times in the range of 30% to 3000% ($\alpha = 1$, $v_0 = 1$), thus indicating that the additional weakening effect from fluid pressurization is likely significant in this setting.

2.4 Phase diagram of injection-induced seismicity

To study the influence of reservoir properties on injection-induced seismicity, we simulate the occurrence of earthquakes as a function of dimensionless injection rate $rq = d_{\mathrm{c}} k_{\mathrm{n}}^{\mathrm{eff}} Q/(p_{\mathrm{c}} V_*)$ and normalized diffusivity $c = d_{\mathrm{c}} k_{\mathrm{n}}^{\mathrm{eff}} k/(\eta L V_*)$ for the case $a = 0$, $b = 0.01$, $\alpha = 1$, and $\kappa = 0.011$ (Fig. 2-7). Diffusivity is varied by varying permeability. Each point on the phase diagram represents the maximum slip velocity of a different simulation run with a particular injection rate and a particular normalized diffusivity. The red dots indicate the occurrence of one or more earthquakes over a finite time period, whereas the grey dots indicate the absence of earthquakes over the same period. We observe two distinct regimes depending on the normalized diffusivity: a high diffusivity regime for $c > 1$, and a low diffusivity regime for $c < 0.01$.

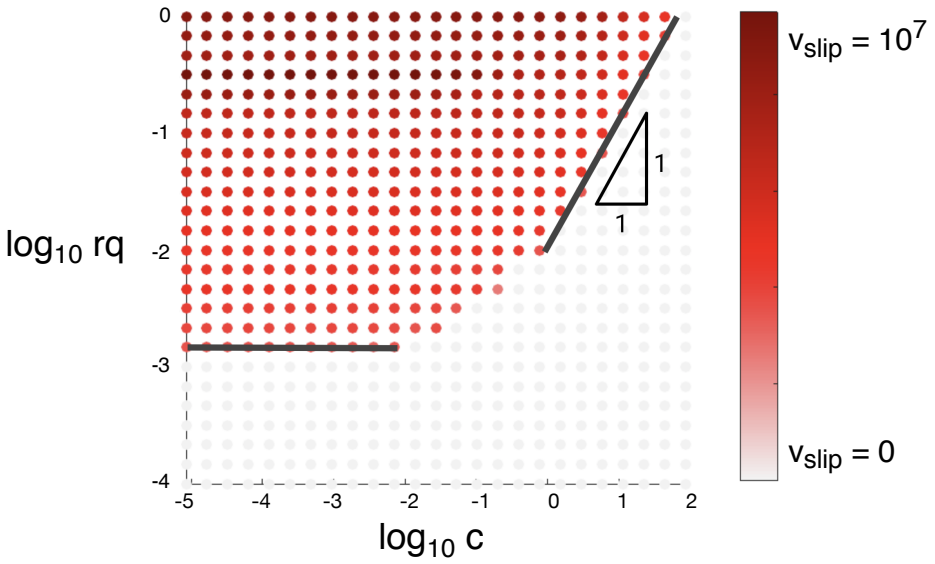

Figure 2-7: Phase diagram of triggered earthquakes as a function of dimensionless injection rate normalized diffusivity.

When the normalized diffusivity is higher than one, the dimensionless pressure diffusion time is less than one. Pore pressure reaches steady-state on a very short time scale, and so the rate of change in pore pressure is negligible. To quantify this, we write

$$\dot{p} \approx 0, \tag{2.71}$$

$$p \approx p_0 + \frac{rq}{c}. \tag{2.72}$$

It is helpful to express the condition for instability (Eq. (2.28)) in terms of rq_{crit} so that an earthquake is triggered if the injection rate is higher than a critical value given by

$$rq_{\text{crit}} \approx \left[(\sigma - p_0) - \frac{\kappa}{(b-a)}\right] c. \tag{2.73}$$

We find that the injection rate required to trigger an earthquake is proportional to diffusivity c, which explains the simulation results in Figure 2-7: In the regime of high diffusivity $c > 1$, $q_{\text{crit}} \sim c$. Accordingly, earthquakes are more easily triggered when fluid is injected into a low permeability reservoir rock than a high permeability, for a fixed effective stiffness.

Conversely, when the normalized diffusivity is lower than 0.001, the dimensionless pressure diffusion time is more than 100. Pore pressure stays near the initial transient-state throughout the simulation period and so the magnitude of change in pore pressure is negligible. To quantify this, we write

$$\dot{p} \approx rq, \tag{2.74}$$

$$p \approx p_0. \tag{2.75}$$

If we express the condition for instability in terms of rq_{crit}, similar to the high diffusivity case above, we find that the injection rate required to trigger an earthquake is

$$rq_{\text{crit}} \approx \frac{v_0}{\alpha}\Big[\kappa - (b-a)(\sigma - p_0)\Big]. \tag{2.76}$$

This also explains the simulation results in Figure 2-7: In the regime of low diffusivity $c < 0.01$, $q_{\text{crit}} \sim$ const. Accordingly, in this regime, earthquake triggering is independent of permeability. These results, as a whole, suggest that reservoirs with high hydraulic diffusivity and low stiffness may be safer sites for fluid injection operations compared to sites with low hydraulic diffusivity and high stiffness.

2.5 Injection scenarios

To further understand how injection rate may be used to minimize or mitigate the seismic hazard, we simulate three different injection scenarios, and examine the stability of each. Figure 2-8 demonstrates how injecting the same volume of fluid can have very different seismic potential depending on the injection profile. We observe that injecting at constant rate in scenario (A) causes the critical stiffness to increase at early times, potentially triggering earthquakes, and decrease at late times, potentially resulting in the cessation of earthquakes. In addition, we observe a dramatic drop in critical stiffness upon stopping injection followed by recovery to the value prior to injection. Scenario (B) shows that a higher injection rate yields higher critical stiffness, implying an increased risk of seismicity for this higher injection rate.

Scenario (C), where the injection rate ramps up in stages, seems to be most stable because the maximum critical stiffness is lower than its value in both (A) and (B). This suggests that a gradual increase in injection rate, where pore pressure is allowed to stabilize between injection stages, may be the safest injection strategy.

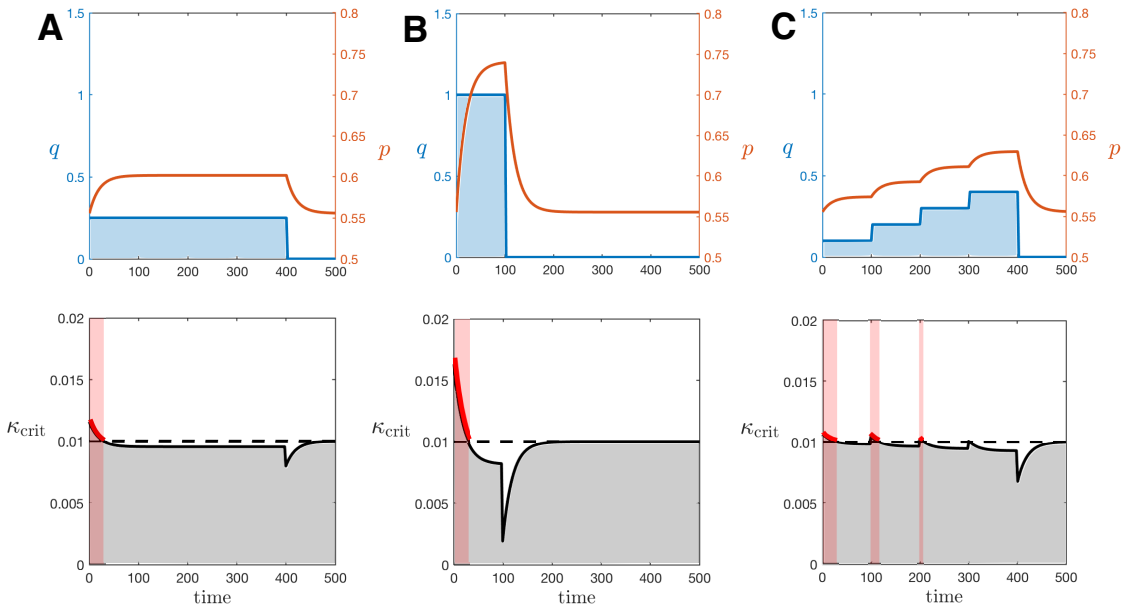

Figure 2-8: Comparison of stability profiles for three different injection scenarios with the same total injected volume.

Chapter 3

Influence of fluid injection on energy partitioning

Earthquakes occur naturally on subsurface faults in the earth's crust, or anthropologically by subsurface energy activities (National Research Council, 2013). Natural earthquakes are caused by the slow buildup of elastic strain energy over geologic times. When tectonic shear stress exceeds fault friction, an earthquake occurs, during which the energy is released as frictional energy, fracture (or breakdown) energy, and radiated energy in the form of seismic waves. The energy partitioning of natural earthquakes has been theoretically investigated by a large body of research using analytical models of dynamic shear cracks and numerical simulations (Kanamori and Rivera, 2006; Beeler, 2001; Scholz, 2002; Kostrov, 1974; Dahlen, 1977). Specialized studies include non-mechanical processes such as flash heating, thermal pressurization and melting (Brantut and Viesca, 2017; Kanamori et al., 2000), complex fault networks and dip-slip faults (Cooke and Murphy, 2004; Dempsey et al., 2012), and variable earthquake rupture modes such as self-healing pulses and mild cracks (Lambert et al., 2021).

Anthropogenic earthquakes can be induced or triggered (McGarr et al., 2002; Albano et al., 2017; Silva et al., 2021). They are induced when subsurface activities perturb stresses around faults originally far from failure, and triggered when faults are already close to failure. Typically, there is a delay between the beginning of

fluid injection and the start of seismicity (Van Der Elst et al., 2013). The energy partitioning of anthropogenic earthquakes has not yet been explicitly studied, but there have been some studies done on the radiated energy and related parameters of such earthquakes. The radiated energy is found by laboratory and in situ experiments to be extremely low compared to the product of injected fluid volume and pressure (or injection energy), and the ratio is lower for induced earthquakes compared to triggered ones (Goodfellow et al., 2015; Kwiatek et al., 2018). A related parameter is the seismic moment (Kanamori, 1978), which is the product of fault slip, rupture area, and shear modulus. It is hypothesized that its maximum is bounded by the product of injected fluid volume and shear modulus (McGarr, 2014; Hallo et al., 2014; Galis et al., 2017). This hypothesis assumes that earthquakes are induced and that most of the energy released come from fluid injection. It is, however, not always accurate (e.g., 2017 Pohang earthquake (Lee et al., 2019; Li et al., 2021)). It is also found by laboratory experiments that the temporal evolution of seismic moment is directly related to fluid pressurization rate (Wang et al., 2020a). To date, there is no physics-based framework that rationalizes or predicts these disparate findings.

To address this gap, we perform an energy analysis of the full anthropogenic earthquake cycle using a single-degree-of-freedom spring poroslider and rate-and-state friction (Alghannam and Juanes, 2020). The model captures stick-slip motion on a fault in contact with a reservoir (Fig. 2-1), where the stick is the interseismic period of elastic strain accumulation and the slip is the seismic wave-producing rupture (Brace and Byerlee, 1966). A key element of the analysis is incorporating the seismic radiation within the spring poroslider using a precisely-defined viscous damper. We then use it to study fluid injection and assess its effects on the energy partitioning during induced and triggered earthquakes.

3.1 Fluid injection into a poroelastic reservoir

When fluid is injected into a reservoir, pore pressure change induces effective stress variations in the reservoir and surrounding rock. We model the corresponding de-

formation process by a poroslider (Alghannam and Juanes, 2020), where a piston is loaded vertically and compresses a spring inside a fluid-filled space. The vertical spring is analogous to the rock skeleton, while the fluid inside the slider represents fluid in the rock pores subject to increase from fluid injection and decrease from pressure diffusion. In this section, we derive an energy balance for this process from the work-energy theorem.

Starting with force balance, we specify the total load acting on the poroslider to be σA, the force acting on the fluid to be pA, and the force acting on the skeleton to be $\sigma' A$. This, using the convention of compression positive, leads to

$$A\sigma = A\sigma_0' - k_\mathrm{n} w + Ap, \tag{3.1}$$

where w is the vertical displacement, k_n is the normal spring stiffness, and σ_0' is the initial effective stress. The net work done on the poroslider as the spring deforms vertically, as a result of fluid injection, is the product of the net load and vertical displacement. In rate form, it is expressed as

$$\sigma A\dot{w} = \sigma_0' A\dot{w} - \left(\frac{1}{2}k_\mathrm{n} w^2\right)^{\cdot} + pA\dot{w}, \tag{3.2}$$

where $\dot{w}$ is the rate of vertical displacement.

We specify the change of mass from fluid seepage to be $\rho A u_\mathrm{f}$, mass accumulation due to rock expansion or fluid compressibility is $(\rho v_\mathrm{f})^{\cdot}$, and injection source term to be $\tilde{q}$. We assume that both the fluid and rock matrix are compressible (Wang, 2000), and so mass balance leads to

$$(\rho V_\mathrm{f})^{\cdot} = \tilde{q} - \rho A u_\mathrm{f}. \tag{3.3}$$

The relative fluid velocity with respect to the skeleton is expressed using Darcy's law as $u_\mathrm{f} = (\kappa/\eta)(p - p_0)/L$, where η is fluid dynamic viscosity, κ is permeability, and L is the pressure diffusion length. The mass accumulation term can be expressed using chain rule and equation of state as $(\rho V_\mathrm{f})^{\cdot} = \rho\dot{v}_\mathrm{f} + (\dot{\Psi}\rho^2/p)V_\mathrm{f}$, where Ψ is the Helmholtz

free energy density such that, $p = \rho^2 \partial\Psi/\partial\rho$ (Truesdell, 1984). When fluid is injected into a rock that is free to deform in the direction orthogonal to sliding, the addition of mass induces an increase of volume equivalent to $V_\mathrm{f} - V_{\mathrm{f},0} = Aw$, where $V_{\mathrm{f},0}$ is the initial fluid volume. We can now re-write the last term in Eq. (3.2) as

$$p\dot{V}_\mathrm{f} = Apq - pAu_\mathrm{f} - \rho\dot{\Psi}V_\mathrm{f}, \tag{3.4}$$

where q is the volumetric injection rate per unit area ($q = \tilde{q}/\rho A$).

By substituting Eq. (3.4) into Eq. (3.2) and re-arranging terms, the energy balance for fluid injection into a poroelastic reservoir becomes

$$\dot{E}_\mathrm{in} - \dot{W}_\mathrm{ex} = \dot{E}_\mathrm{e,s} + \dot{E}_\mathrm{e,f} + \dot{E}_\mathrm{v}. \tag{3.5}$$

The terms in Eq. (3.5) have a physical significance as follows: $\dot{E}_\mathrm{in} = pqA$ is the power source or power supplied by fluid injection, $\dot{W}_\mathrm{ex} = Ap_0(\dot{w} + u_\mathrm{f})$ is the rate of work done by the system on external boundary where $(\dot{w} + u_\mathrm{f})$ is the absolute velocity of the fluid, $\dot{E}_\mathrm{e,s} = (\frac{1}{2}k_\mathrm{n}w^2)^{\cdot}$ is the rate of elastic energy stored in the spring, $\dot{E}_\mathrm{e,f} = \rho\dot{\Psi}V_\mathrm{f}$ is the rate of energy stored in the fluid by compressibility, and $\dot{E}_\mathrm{v} = \frac{\eta L}{k}Au_\mathrm{f}^2$ is the rate of energy dissipated by viscous forces. This energy balance (Eq. (3.5)) provides a basis for the problem of energy partitioning during fluid injection in section 3.4.2.

3.2 Stick-slip motion on a fault

To model the effects of variations in pore pressure on a creeping fault segment, we attach the poroslider to an elastic spring. The coupled model represents frictional slip and consists of a slider that is pulled by a spring whose end is constrained to move at a steady velocity. The spring stiffness accounts for the elastic interaction of the sliding surface with the surrounding rock (Rice and Tse, 1986). In this section, we derive an energy balance for frictional stick-slip from the work-energy theorem.

From momentum balance of forces acting on the slider, the equation of motion of

the system evolution at variable effective normal stress is

$$m\ddot{x} = k_{\mathrm{s}}(\dot{x}_{\infty}t - x) - \mu(\dot{x}, \theta)\sigma' A, \tag{3.6}$$

where x is the slip distance, $\dot{x}_{\infty}$ is the loading velocity, $u = \dot{x}_{\infty}t - x$ is the relative displacement between the load point and the slider, m is the mass, k_{s} is the shear stiffness, and $\mu(\dot{x}, \theta)$ is the Linker and Dieterich (1992) form of rate-and-state friction. Parameter θ is a state variable describing the sliding surface. According to Eq. (3.6), the sum of friction and spring forces acting on the slider, or the net force, determines the rate of change in momentum. The work done by all the forces acting on the slider, or the net work, is the product of the net force and slip distance. In rate form, this is

$$m\ddot{x}\dot{x} = k_{\mathrm{s}}(\dot{x}_{\infty}t - x)\dot{x} - \mu(\dot{x}, \theta)\sigma' A\dot{x}. \tag{3.7}$$

Note that $x(0)$ is not always zero, as the spring may have a pre-stretched initial state corresponding to background tectonic stresses in the Earth. By writing the relative displacement as $u = (\dot{x}_{\infty}t - x) - u(0) + u(0)$ and re-arranging terms, Eq. (3.7) becomes

$$\left(\frac{1}{2}m\dot{x}^2\right)^{\cdot} = k_{\mathrm{s}}u\dot{x}_{\infty} - \left(\frac{1}{2}k_{\mathrm{s}}(u - u(0))^2\right)^{\cdot} - k_{\mathrm{s}}u(0)\dot{u} - \sigma' A\mu(\dot{x}, \theta)\dot{x}. \tag{3.8}$$

We then re-express Eq. (3.8) to obtain the energy balance for stick-slip motion on a fault

$$\dot{E}_{\mathrm{k}} = \dot{W} - \dot{E}_{\mathrm{e}} - \dot{E}_{\mathrm{e},0} - \dot{E}_{\mathrm{f}}, \tag{3.9}$$

where $\dot{E}_{\mathrm{k}}$ is the rate of kinetic energy released, $\dot{W}$ is the power supplied to produce motion $\dot{x}_{\infty}$, $\dot{E}_{\mathrm{e}}$ is the rate of change in elastic strain energy, $\dot{E}_{\mathrm{e},0}$ is the power supplied through the pre-stretch, and $\dot{E}_{\mathrm{f}}$ is the rate of dissipated energy including frictional and breakdown energies. The frictional energy is due to constant friction on the fault plane. It is often equated to the energy dissipated as heat (Kanamori and Rivera,

2006). The breakdown energy is due to a combination of many processes (e.g., plastic yielding, micro cracking, breaking of asperity contacts, etc) (Lin and Segel, 1988). It is the part of the dissipated energy that controls the dynamics of the rupture and is often considered as the frictional analog of the fracture energy from singular and cohesive-zone models of dynamic fracture theory (Kanamori and Rivera, 2006; Cocco et al., 2004). This energy balance (Eq. (3.9)), however, is missing seismic radiation—a key element of the problem of energy partitioning during earthquakes.

3.3 Seismic radiation

One of the most fundamental measures of earthquake dynamics is the total radiated energy. It is defined as the amount of energy that would be carried to the far field in the form of seismic waves if an earthquake occurred in an infinite and non attenuating medium (Rivera and Kanamori, 2005). In seismological practice, seismic radiated energy is obtained from the transient dynamic displacements inferred from examination of seismograms or from measurements of deformation in the epicentral region (Udías et al., 2014; Shearer, 2019). This energy is theoretically determined from the energy flux carried by P and S waves at the far-field (Rudnicki and Freund, 1981). It can also be expressed as a surface integral over the fault plane with the integrand containing the slip function on the fault plane (Rivera and Kanamori, 2005; Kostrov, 1974). Both methods assume a dynamic shear crack in a two- or three-dimensional continuum.

Spring sliders, however, are zero-dimensional and do not take into account the fact that seismic radiation is a mechanism in nature whereby part of the elastic energy lost during rupture can travel away from the fault. A radiation damping term, $\eta\dot{x}$, is sometimes used to approximate energy lost as propagating seismic waves (Burridge and Knopoff, 1967; Beeler, 2001). The coefficient η governs the rate at which energy is radiated away from the fault. In multi-dimensional simulations, it is often taken as $G/2c$, where G is the shear modulus and c is the shear wave speed (Rice, 1993; Thomas et al., 2014), or as a large constant in "quasi-dynamic" simulations (Segall and

Rice, 1995; Pampillón et al., 2018). The former assumes planar waves in a continuum and the later is arbitrary—neither is appropriate to simulate seismic radiation in a spring slider.

Radiation effects can be simulated is by attaching a semi-infinite multi-degree-of-freedom spring-mass system to the slider such that the motion of the slider exciteps a wave traveling upward (Fig. 3-1). The equations of motion for the system are

$$m\ddot{x}_0(t) + k_s x_0(t) + k_s(x_0(t) - x_1(t)) = k_s \dot{x}_\infty t - \sigma' A\mu(\dot{x}_0, \theta), \tag{3.10}$$

$$m\ddot{x}_1(t) + k_s(x_1(t) - x_0(t)) + k_s(x_1(t) - x_2(t)) = 0, \tag{3.11}$$

$$\vdots \tag{3.12}$$

$$\dot{x}_n(t) + \sqrt{k_s/m}(x_n(t) - x_{n-1}(t)) = 0, \tag{3.13}$$

where Eq. (3.13) represents an absorbing boundary condition to prevent significant wave reflection.

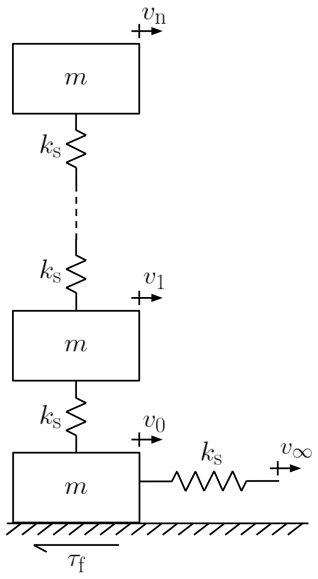

Figure 3-1: A semi-infinite multiple-degree-of-freedom system representing seismic waves radiating away from a moving spring slider on a frictional interface.

The simplest analytical solution to the single-degree-of-freedom spring slider is for the case when the effective normal stress is constant and friction is assumed to drop from an initial static value to a lower dynamic value instantly upon sliding

(Scholz, 2002; Nur, 1978; Jaeger and Cook, 1976). The driving force is therefore the difference between static and dynamic frictions, $F = \Delta\mu\sigma' A$. If we further assume that, during the slip phase, the load point velocity $\dot{x}_\infty$ is negligible compared with the average velocity of the slider, the first-order approximation of the motion becomes $m\ddot{x}_0 + k_\mathrm{s} x_0 = \Delta\mu\sigma' A$ with initial conditions $x_0(0) = \dot{x}_0(0) = 0$. The solutions for displacement and velocity are $x_0(t) = (\Delta\mu\sigma' A/k_\mathrm{s})(1 - \cos(\sqrt{k_\mathrm{s}/m}\ t))$ and $\dot{x}_0(t) = (\Delta\mu\sigma' A/m)\sin(\sqrt{k_\mathrm{s}/m}\ t)$, respectively.

By the D'Alembert solution, the displacement and velocity of a wave traveling in a continuum are $x(y,t) = x_0(t - x/c)$ and $\dot{x}(y,t) = \dot{x}_0(t - y/c)$, where c is the wave speed (Bekefi and Barrett, 1977; Pinchover and Rubinstein, 2005). We assume unit length for spacing between masses, and so the displacement and velocity of the multi-degree-of-freedom spring mass system attached to the slider are $x_\mathrm{i}(t) = x_0(t - i/\sqrt{k_\mathrm{s}/m})$ and $\dot{x}_\mathrm{i}(t) = \dot{x}_0(t - i/\sqrt{k_\mathrm{s}/m})$, where i is a mass index and $\sqrt{k_\mathrm{s}/m}$ is the velocity of the wave traveling upward. The force exerted by the spring on the mass is $k_\mathrm{s}(x_\mathrm{i}(t) - x_{\mathrm{i}-1}(t))$. By Taylor expansion about $t - i/\sqrt{k_\mathrm{s}/m}$, it is equal to $k_\mathrm{s}(x_0(t - i/\sqrt{k_\mathrm{s}/m}) - x_0(t - (i-1)/\sqrt{k_\mathrm{s}/m}))$. It may be further approximated by $k_\mathrm{s}\dot{x}_\mathrm{i}(t - i/\sqrt{k_\mathrm{s}/m})(-1/\sqrt{k_\mathrm{s}/m})$. This gives a dissipative force proportional to velocity, $-\sqrt{k_\mathrm{s}m}\dot{x}_\mathrm{i}(t)$. Therefore, seismic radiation can be modeled within the zero-dimensional spring slider by adding a radiation damping term $\eta\dot{x}$ to the equations of motion, with coefficient $\eta = \sqrt{k_\mathrm{s}m}$.

The final energy balance for stick-slip motion on a fault including seismic radiation is

$$\dot{E}_\mathrm{k} + \dot{E}_\mathrm{r} = \dot{W} - \dot{E}_\mathrm{e} - \dot{E}_{\mathrm{e},0} - \dot{E}_\mathrm{f}, \tag{3.14}$$

where $\dot{E}_\mathrm{r} = \sqrt{k_\mathrm{s}m}\dot{x}^2$ is the power radiated away from the slider—analogous to the seismic power radiated away from a fault. The validation of this analytical expression against numerical simulations with the multi-degree-of-freedom system is found in section 3.3.1. This energy balance (Eq. (3.14)) provides a basis for the problem of energy partitioning during the full earthquake cycle in section 3.4.

3.3.1 Validation against numerical simulations

To validate the radiation damping term we derived, we simulate motion of the multi-degree-of-freedom system (Eqs. 3.10-3.13) and the single-degree-of-freedom system with damping (below)

$$\dot{u} = v_\infty - v, \tag{3.15}$$

$$\dot{v} = \frac{1}{(T/2\pi)^2}\left[u - \frac{1}{k_\mathrm{s}}(\mu_* + a\ln\frac{v}{v_*} + \theta)A(\sigma - p) - \sqrt{\frac{m}{k_\mathrm{s}}}v\right], \tag{3.16}$$

$$\dot{\theta} = -\frac{v}{d_\mathrm{c}}(\theta + b\ln\frac{v}{v_*}) + \alpha\frac{\dot{p}}{(\sigma - p)}, \tag{3.17}$$

$$\dot{p} = \frac{k_\mathrm{n}^\mathrm{eff}k}{\eta LA}(p_\infty - p) + \frac{k_\mathrm{n}^\mathrm{eff}}{A}q, \tag{3.18}$$

where u is the relative displacement between the load point and the slider, $\dot{(\,)}$ denotes time derivative, v_∞ is the loading velocity, v is slip rate, T is the vibration period, k_s is the shear stiffness, v_* is a normalizing slip rate, μ_* is a constant coefficient appropriate for steady-state friction at slip rate v_*, a and b are experimentally derived parameters relating friction to changes in slip rate and state, respectively, θ is a state variable describing the sliding surface, σ is the total stress, p is the pressure inside the slider (pore pressure), d_c is the characteristic slip distance, $\hat{\alpha}$ is a scaling factor ranging from 0 to μ, $k_\mathrm{n}^\mathrm{eff}$ is the effective normal stiffness (related to the uniaxial bulk modulus or the reciprocal of the uniaxial specific storage per diffusion length in a continuum), k is the permeability, η is fluid dynamic viscosity, L is the pressure diffusion length, p_0 is the ambient pressure, and q is the volumetric injection rate per unit area.

Figure 3-2 illustrates the radiated energy (the difference between the change in elastic energy and the energy dissipated by breakdown and friction) for a 3 degree-of-freedom system (A) and an 11 degree-of-freedom system (B). The results are almost identical as the same seismic wave travels up both systems. The 3 DOF system exhibits less numerical oscillations than the 11 DOF system. The results of the radiated energy of the single-degree-of-freedom spring slider system with radiation damping are illustrated in Figure 3-3. Three cases are presented: (A) $\eta = 2\sqrt{k_\mathrm{s}m}$,

(B) $\eta = \sqrt{k_s m}$, and (C) $\eta = (1/2)\sqrt{k_s m}$. Case (A) exhibits no dynamic overshoot and case (C) overpredicts overshoot. The results given by damping term in case (B) are closest to those obtained by simulating the multi-degree-of-freedom, and show that our estimate of seismic radiation is 92% to 96% accurate. In this case, the dynamic slip overshoots the static slip by about 15 percent—in agreement with theoretical studies of dynamic circular faults and laboratory observations (Madariaga, 1976; McGarr, 1999; Lockner and Okubo, 1983). The amount of overshoot is a direct result of inertia and seismic radiation.

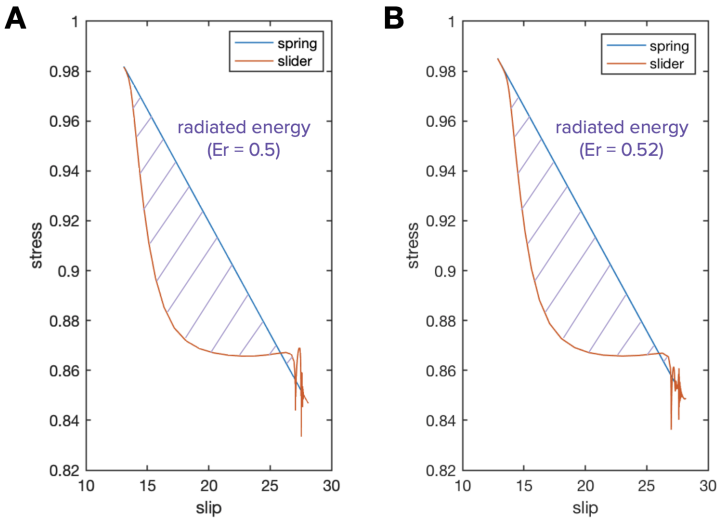

Figure 3-2: Estimates of the radiated energy from a full couple 3 degree-of-freedom system (A) and 11 degree-of-freedom system (B) (quantities expressed here are dimensionless).

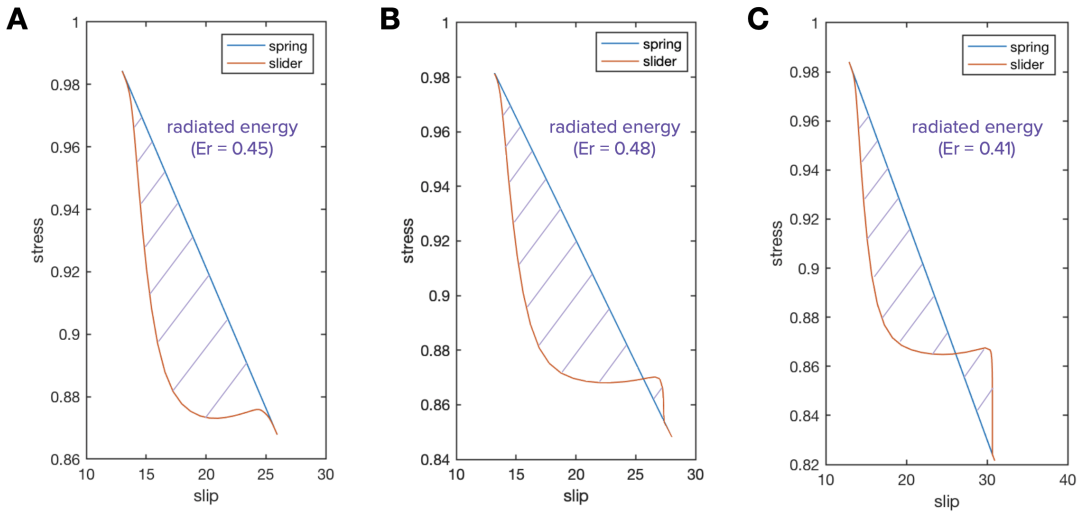

Figure 3-3: Estimates of the radiated energy from a single degree of freedom system with radiation damping term: (A) $\eta = 2\sqrt{km}$, (B) $\eta = \sqrt{km}$, and (C) $\eta = (1/2)\sqrt{km}$ (quantities expressed here are dimensionless).

3.4 Energy partitioning

Understanding the mechanisms controlling anthropogenic earthquakes is key in defining strategies to mitigate them (National Research Council, 2013). The partitioning of energy released during an earthquake into frictional, breakdown, and radiated energy gives an indication of the overall size of the earthquake and its potential for damage to man-made structures (Boatwright and Choy, 1986; Kanamori, 1978; Kanamori and Rivera, 2006). Coupling it with the partitioning of energy supplied by fluid injection into dissipated and stored energy in fluid and skeleton gives an indication of the source of energy released, and how it is influenced by injection parameters (Kwiatek et al., 2018; Li et al., 2021). In this section, we consider the energy budget of a spring poroslider model without fluid injection as a base case (section 3.4.1), and then analyze how it is altered by fluid injection (section 3.4.2). We simulate the spring-poroslider system of equations (section 3.3.1) with the properties listed in table 3.1. Note that these properties do not reflect a specific real setting, but rather generally represent sandstone reservoirs with velocity-weakening faults. Performing energy partitioning analyses for specific real settings could be the subject for future

studies.

Table 3.1: Reservoir and fault properties.

p_∞ (Pa)	$30 * 10^6$	v_* (m/s)	10^{-9}
σ (Pa)	$90 * 10^6$	v_∞ (m/s)	$1.5 * 10^{-9}$
q (m/s)	$10^{-7} - 10^{-8}$	d_c (m)	10^{-2}
K_f (Pa)	$3 * 10^9$	μ_*	0.6
K_v (Pa)	$6 * 10^9$	$\tilde{a}$	0.006
ϕ	0.2	$\tilde{b}$	0.0108
η (Pa.s)	0.001	$\tilde{\alpha}$	0.6
κ (m^2)	$3 * 10^{-14}$	k_s (Pa.m)	$4.3 * 10^6$
L (m)	$3 * 10^3$	T (s)	500

3.4.1 Natural earthquakes

Consider a slider on a frictional surface and connected to a spring which is driven slowly at a uniform velocity. While the slider is nearly stuck, the spring is stretched by the uniform motion of its end at constant velocity $\dot{x}_\infty$. The stick period (shaded by grey in Fig. 3-4A) represents the strain loading of the medium by tectonic forces. By integrating Eq. (3.14) over this time period, the elastic energy accumulated in the spring is

$$\Delta E_\mathrm{e}|_\mathrm{stick} = \frac{k_\mathrm{s}}{2}(\dot{x}_\infty t)^2, \tag{3.19}$$

where $\dot{x}_\infty t$ is the elongation of the spring. In our example, $\Delta E_\mathrm{e}|_\mathrm{stick} = 4.3 \times 10^7$ J/m^2.

The slider is then made unstable by suddenly increasing the loading velocity. This change creates an excess of spring force over the frictional resistance, which in turn accelerates the slider. The friction drops to a lower dynamic value over a characteristic slip distance. The slider continues to slip at a high rate until further shortening of the spring is no longer possible, overshoots, and then decelerates to reach a nearly stationary state. The slip period (shaded by grey in Fig. 3-4B) represents the seismic rupture. As the spring force drops from an initial value $\tau_\mathrm{s,i}$ to a final value $\tau_\mathrm{s,f}$, the

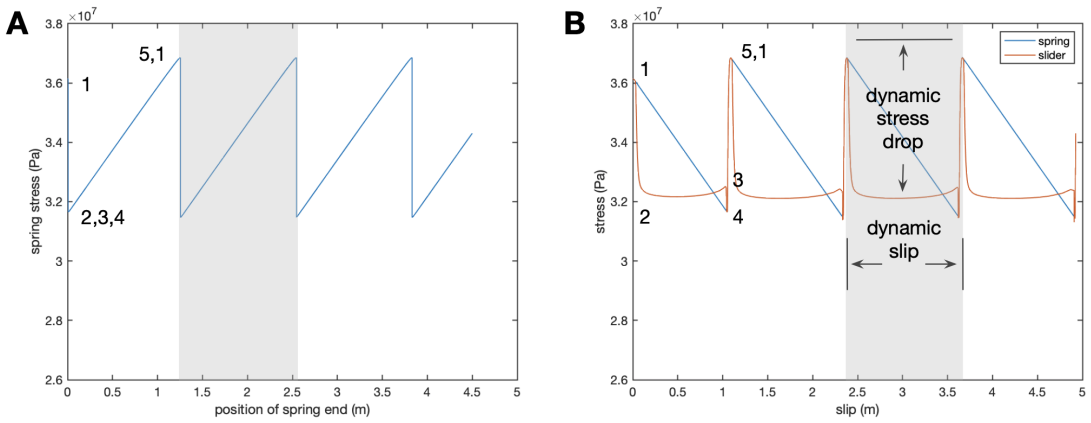

Figure 3-4: Dynamics of stick-slip cycle without fluid injection.

change in elastic energy in the spring is,

$$\Delta E_{\mathrm{e}}|_{\mathrm{slip}} = -\frac{1}{2}(\tau_{\mathrm{s,i}} + \tau_{\mathrm{s,f}})A\Delta x, \tag{3.20}$$

where Δx is the total slip. In our simulations, $\Delta E_{\mathrm{e}}|_{\mathrm{slip}} = 4.2 \times 10^7$ J/m^2. Most of this energy is dissipated,

$$\Delta E_{\mathrm{f}} = \int_{x_1}^{x_2} \mu(\dot{x}, \theta)\sigma' A \; dx. \tag{3.21}$$

This integral includes both the breakdown and frictional energies (section 3.2). The former is generally much smaller than the latter (Scholz, 2002), and so we just compute the lumped value $\Delta E_{\mathrm{f}} = 4 \times 10^7$ J/m^2. The remaining energy is radiated as seismic waves,

$$\Delta E_{\mathrm{r}} = \int_{\mathrm{x}_1}^{\mathrm{x}_2} \sqrt{k_{\mathrm{s}} m}\dot{x} \; dx. \tag{3.22}$$

In our simulations, $\Delta E_{\mathrm{r}} = 2.3 \times 10^6$ J/m^2. Note that the kinetic energy vanishes before and after slip, and so $\Delta E_{\mathrm{k}} = 0$.

Graphically, the energy budget during a natural earthquake is illustrated in Fig. 3-5. The change in elastic strain energy is given by the trapezoidal area under the curve for spring load, the total dissipated energy is given by the area under the curve for

frictional resistance, and the seismic radiated energy given is the difference between the two. The ratio of the radiated energy to the change in elastic strain energy is referred to as the seismic efficiency. It serves as an indicator of earthquake potential for damage to man-made structures. McGarr (1994, 1999) shows that it is typically less than 6%. For the particular set of reservoir and fault properties in table 3.1, it is estimated to be around 5%. Stress drop and total slip—indicators of the overall size of an earthquake—can also be estimated from our energy budget. They are around 5 MPa and 1.2 m, respectively.

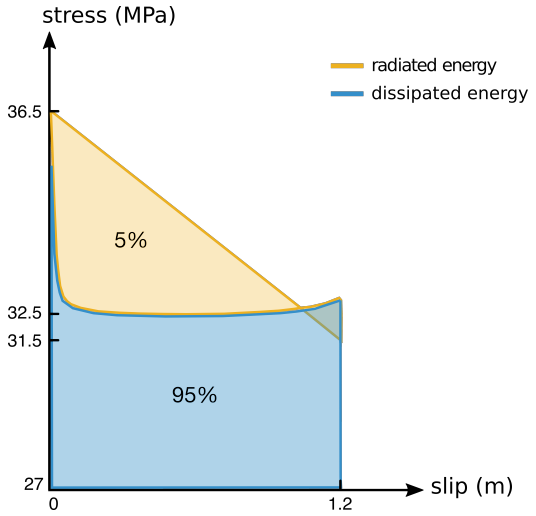

Figure 3-5: Energy partitioning during a natural earthquake.

3.4.2 Anthropogenic earthquakes

When fluid is injected into a faulted reservoir, pore pressure change induces effective stress variations in the reservoir and surrounding rock. It increases at high rate at early times, and then reaches steady state at late times by balancing the rate of fluid injection with the rate of pore pressure diffusion (Alghannam and Juanes, 2020). Fluid injection induces or triggers slip when the resulting change in frictional resistance occurs at a rate greater than the loading system is capable of following, that is, when the stiffness of the loading system is lower than a critical value given

by

$$k_{\mathrm{s,crit}} = \left[(b-a) + \alpha \frac{d_{\mathrm{c}}}{v_{\infty}} \frac{\dot{p}}{\sigma'}\right] \frac{\sigma'}{d_{\mathrm{c}}}, \tag{3.23}$$

where a, b, d_{c}, α are rate-and-state frictional parameters (Byerlee, 1970). The term $(b-a)$ represents an original velocity-weakening effect and the term $\alpha d_{\mathrm{c}} \dot{p} / v_{\infty} \sigma'$ represents an additional weakening effect from fluid pressurization. Fluid injection interrupts the stick-slip cycle during the period of elastic strain accumulation. The associated reduction in effective normal stress accelerates the point at which the spring force exceeds the frictional resistance, which in turn leads to a premature slip (Fig. 3-6).

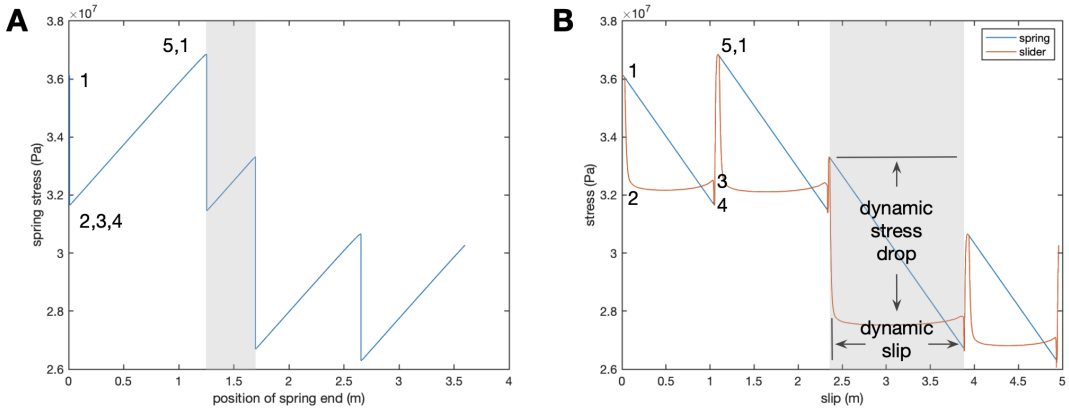

Figure 3-6: Dynamics of stick-slip cycle with fluid injection.

There is a delay from the beginning of fluid injection to the start of slip (Van Der Elst et al., 2013). By integrating Eq. (3.5) over this time period, we can write an expression for the energy input from fluid injection

$$\Delta E_{\mathrm{in}} = \Delta W_{\mathrm{ex}} + \Delta E_{\mathrm{e,s}} + \Delta E_{\mathrm{e,f}} + \Delta E_{\mathrm{v}}. \tag{3.24}$$

We simulate four cases (tables 3.2-3.4) corresponding to two injection rates (10^{-7} m/s and 10^{-8} m/s) and two types of anthropogenic earthquakes (induced and triggered). The earthquake is induced when fluid injection interrupts the stick-slip cycle early during the period of elastic strain accumulation, and is triggered when fluid injection interrupts the cycle late (Albano et al., 2017; Silva et al., 2021; McGarr et al., 2002).

Table 3.2: Summary of fluid injection into the reservoir.

case	type of earthquake	q (m/s)	time to first event (s)	cumulative injection (m)	E_{in} (J/m^2)	$\Delta E_{\text{e,s}}/\Delta E_{\text{in}}$ (%)
1	natural	0	–	0	–	–
2	induced	10^{-7}	$1.3 * 10^8$	13	$4.61 * 10^8$	3.9
3	induced	10^{-8}	$6.2 * 10^8$	6.2	$1.93 * 10^8$	0.1
4	triggered	10^{-7}	$4.5 * 10^7$	4.5	$1.47 * 10^8$	3.8
5	triggered	10^{-8}	$1.4 * 10^8$	1.4	$4.34 * 10^7$	0.4

Table 3.3: Summary of stick-slip energies on the fault.

case	$\Delta E_{\text{e}}\|_{\text{stick}}$ (J/m^2)	$\Delta E_{\text{e}}\|_{\text{slip}}$ (J/m^2)	ΔE_{f} (J/m^2)	ΔE_{r} (J/m^2)
1	$4.26 * 10^7$	$4.22 * 10^7$	$3.98 * 10^7$	$2.31 * 10^6$
2	$1.39 * 10^7$	$4.56 * 10^7$	$4.2 * 10^7$	$3.57 * 10^6$
3	$3.97 * 10^7$	$4.34 * 10^7$	$4.1 * 10^7$	$2.32 * 10^6$
4	$3.58 * 10^7$	$5.53 * 10^7$	$5.1 * 10^7$	$4.53 * 10^6$
5	$4.09 * 10^7$	$4.4 * 10^7$	$4.15 * 10^7$	$2.4 * 10^6$

Table 3.4: Summary of efficiencies and event size indicators.

case	$\dot{p}\|_{\text{event}}$ (Pa/s)	$\Delta E_{\text{r}}/\Delta E_{\text{e}}\|_{\text{slip}}$ (%)	$\Delta E_{\text{r}}/\Delta E_{\text{in}}$ (%)	stress drop (Pa)	total slip (m)
1	–	5.47	–	$5.36 * 10^6$	1.25
2	$2.2 * 10^{-2}$	7.83	0.77	$6.61 * 10^6$	1.53
3	$2 * 10^{-6}$	5.35	1.2	$5.42 * 10^6$	1.27
4	$7.5 * 10^{-2}$	8.19	3.08	$7.45 * 10^6$	1.72
5	$1.9 * 10^{-3}$	5.45	5.53	$5.55 * 10^6$	1.29

We take case 2 as an example. Figure 3-7A illustrates the energy budget for fluid injection into the poroslider. The energies are represented by the areas under and between the curves. Most of the energy input goes into performing work on the external boundary. The remaining energy is initially stored in the compressible fluid. With time, part of it is dissipated by viscous forces from fluid flow and part of it is stored in the skeleton. The amount of elastic energy stored in the skeleton is 4.6×10^8 J/m^2—the lowest out of the four. It is directly related to the rate of fluid injection. This indicates that only a small part (4%) of the energy input has any

potential to contribute to the energy released during frictional slip.

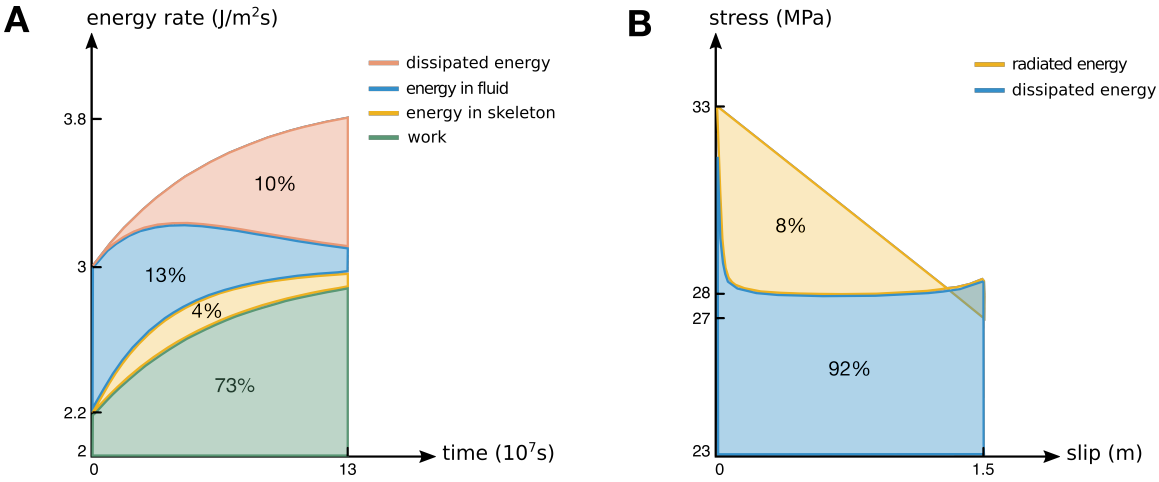

Figure 3-7: Energy partitioning during an induced earthquake.

In case 2, the elastic energy accumulated in the spring during the stick period is 1.4×10^7 J/m^2, lower than the case without fluid injection. During slip, the energy partitioning is as follows: the drop in elastic energy is 4.6×10^7 J/m^2, out of which 4.2×10^7 J/m^2 is dissipated and 3.6×10^6 J/m^2 is radiated as seismic waves (Fig. 3-7B). Seismic efficiency, stress drop, and total slip are 8%, 5 MPa and 1.5 m, respectively—all higher than in the case without fluid injection. The increase in these quantities is a direct consequence of the additional frictional weakening effect from fluid pressurization (Alghannam and Juanes, 2020; Olsson, 1988). This result qualitatively agrees with a laboratory experiment (Wang et al., 2020a), in which it was observed that the temporal evolution of seismic moment (correlated with radiated energy and total slip (Kanamori, 1978)) is affected by fluid pressurization rates. When fluid pressure stabilizes at higher value, subsequent slip events tend to be slightly smaller than the ones prior to fluid injection.

We summarize the results of our analysis of the energy partitioning during anthropogenic earthquakes in tables 3.2-3.4, and find three interesting points. First, the delay between the beginning of fluid injection and the start of seismicity depends on both the rate and timing of fluid injection within the earthquake cycle. That is, it depends on the change of frictional resistance on the fault and the state of tectonic shear loading at the time of injection. Note that our model does not consider the

influence of spatial extent of pore pressure diffusion on the delay (Shapiro and Dinske, 2009). Second, seismic injection efficiency, or the ratio between the radiated energy to the injection energy, is generally very low. It is lower for induced earthquakes ($0.8\% - 1.2\%$) compared to triggered ones ($3.1\% - 5.5\%$), which agrees with laboratory and in situ experiments (Goodfellow et al., 2015; Kwiatek et al., 2018). Third, seismic efficiency, stress drop, and total slip are not correlated with volume of fluid injected. In contrast with some previous studies (McGarr, 2014; De Barros et al., 2019; Wang et al., 2020a), our finding represent earthquakes occurring under variable fluid pressure, while previously published results represent earthquakes occurring under constant fluid pressure.

Chapter 4

Heterogeneous friction and earthquakes

The spring-poroslider is a good first step towards understanding how temporal variations in fluid pressure affects fault stability, but it cannot capture the spatial complexity of fault zones in nature (Loveless and Meade, 2016; Ye et al., 2018; Barnhart et al., 2016). Fault zones in nature are heterogeneous in material and complex in geometry with multiple slip surfaces and deformation zones (Blanpied et al., 1991; Scholz, 1988). In their simplest form, faults consist of a heterogeneous zone of intense deformation, or gouge, which macroscopically is seen as a frictional interface between two surfaces (Childs et al., 1997, 2009). Seismological and laboratory observations suggest that heterogeneity in fault roughness exists at all length scales from a few micrometers to a few kilometers, and spatial variations in the rock physical properties exist at length scales from a few millimeters to hundreds of meters (Kirkpatrick et al., 2020; Power et al., 1987; Candela et al., 2009; Latour et al., 2011). The critical slip distance d_c correlates with the roughness of the sliding surface and width of the gouge zone (Marone, 2002; Ohnaka, 2003; Scholz, 1988), the rate-and-state frictional parameter $b - a$ correlates with the physical properties of rocks and gouge at the interface (Blanpied et al., 1991; Scuderi and Collettini, 2016; Ikari et al., 2009).

To help bridging the gap between the idealized spring-poroslider and natural faults, we extend the model to study the effect of heterogeneity on the dynamics

of frictional slip. In particular, we develop an objective or frame-indifferent formulation of frictional contact between heterogeneous surfaces at the microscopic-scale. We describe friction as a function of the states of the upper and lower surfaces, each representing roughness and microstructual details for the surface. We then spatially average the heterogeneous stress and frictional parameters to obtain a macroscopic-scale representation of time-varying interface friction. Results of this work indicate that the simple heterogeneous Coulomb friction gives rise to complex slip patterns ranging from stable creep to unstable regular stick-slip and slow—potentially leading to a fundamentally new understanding of frictional instabilities and earthquakes.

4.1 Frame-indifferent formulation of frictional slip

Seismological data indicates that subsurface displacements on natural fault planes can go up to a few meters during regular and slow earthquakes (Wells and Coppersmith, 1994; Ohnaka, 2000). The typical sample size in laboratory experiments of friction, for comparison, is around a few centimeters (Marone, 1998; Scholz, 2002). Studying stability of steady sliding between elastically deformable continua using rate- and state-dependent friction laws gives insights into the characteristics of such earthquakes. While some studies have considered the effects of having dissimilar solids and heterogeneous frictional properties (Rice et al., 2001; Shlomai et al., 2020; Aldam et al., 2017, 2016; Ray and Viesca, 2017; Luo and Ampuero, 2018), the description has not addressed the kinematics of large slip—a fundamental aspect to obtain an objective, reference-frame-independent formulation.

Here, we focus on formulating an objective (or frame-indifferent) formulation of friction. We adopt an idealized two-dimensional model of a heterogeneous interface between elastic solids (Fig. (4-1)), where the frictional parameters vary in space. A cause of frictional heterogeneity is material or rock type. For instance, clay-rich fault gouges are weak with coefficient of friction of less than 0.4 whereas basalt is strong with a coefficient of friction around 0.85 (Phillips et al., 2020). Other causes include heterogeneity in surface roughness, micro-structural details, varying wear (or gouge)

thickness, among others (Marone et al., 1990; Kirkpatrick et al., 2020).

The fundamental observation is that points A^+ and P^+ on the upper surface are in contact with different points on the lower surface at each instant of time, and this must be taken into account when defining appropriate time derivatives of interface quantities. Current formulations of friction fail to account for the kinematics of "what is in contact with what" at large slip distances. A commonly used concept in nonlinear continuum mechanics to guarantee frame indifference is the material derivative or, more generally, the Lie derivative (Marsden and Hughes, 1994; Simo et al., 1988). It basically takes a spatial object, transforms it to the reference configuration before time differentiating, and then transform the results back to the spatial frame, so that the effect of the changing basis embedded in the motion is removed from the time derivative (Laursen, 2013).

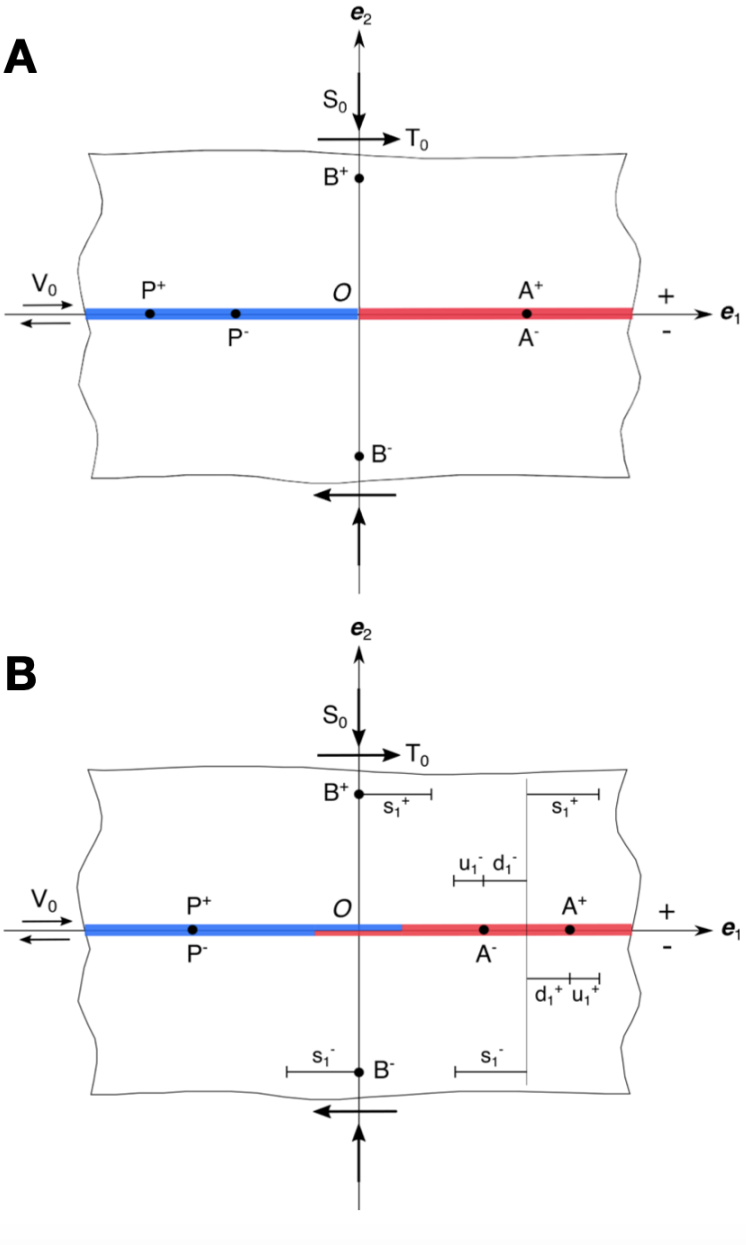

Figure 4-1: Schematic of frictional sliding in 2D, where (A) represents the reference configuration and (B) represents the deformed configuration during slip.

4.1.1 Preliminaries

This section follows the work by Anand (1993). We begin by identifying the elastically deformable continua as two bodies Ω^+ and Ω^-, respectively, whose motions with

respect to reference configurations Ω_0^+ and Ω_0^- are described by

$$a^+ = \Phi^+(p^+, t) \text{ and } a^- = \Phi^-(p^-, t), \tag{4.1}$$

while those relative to their current configurations Ω_t^+ and Ω_t^- are described by

$$y^+ = \Phi_t^+(a^+, \hat{t}) \text{ and } y^- = \Phi_t^-(a^-, \hat{t}), \tag{4.2}$$

where $\hat{t}$ denotes a time Δt later than time t. The incremental displacements corresponding to these motions are denoted by

$$u_t^+(a^+, \hat{t}) = y^+ - a^+ \text{ and } u_t^-(a^-, \hat{t}) = y^- - a^-, \tag{4.3}$$

and the spatial velocities by

$$v^+(a^+, t) = \frac{\partial}{\partial \hat{t}} u_t^+(a^+, \hat{t})|_{\hat{t}=t} \text{ and } v^-(a^-, t) = \frac{\partial}{\partial \hat{t}} u_t^-(a^-, \hat{t})|_{\hat{t}=t}, \tag{4.4}$$

respectively.

Consider the situation when the two bodies are in contact, and assume that the region of contact between the elastically deformable continua is sufficiently "thin" so that it may be replaced by an interface of zero thickness. In particular, we set

$$a \equiv a^+ = a^- \tag{4.5}$$

for the current positions of representative particles p^+ and p^- on either side of the interface and denote it by $\Sigma(a, t) = 0$. Let

$$n(a, t) \tag{4.6}$$

denote the unit normal field on $\Sigma(a, t)$, where n is the unit outward normal to the surface of the upper body Ω_t^+, or equivalently the unit inward normal to the lower

body Ω_{t}^{-} at the point a under consideration at time t. Let

$$\bar{v} \equiv v^{+} - v^{-} \tag{4.7}$$

denote the relative tangential velocity between the upper and lower bodies. Let

$$\bar{u}_t(\hat{t}) \equiv u_{\mathrm{t}}^{+}(a^{+}, \hat{t}) - u_{\mathrm{t}}^{-}(a^{-}, \hat{t}), \tag{4.8}$$

denote the relative tangential displacement increment. We assume that there is no separation or penetration of the two currently contacting points.

An element of area dA on the interface $\Sigma(a,t)$ is subjected to a contact force $\tau_{(\mathrm{n})}^{+}(a^{+},t)dA$ which acts on the material within Ω_{t}^{+}, and $\tau_{(-\mathrm{n})}^{-}dA = -\tau_{(\mathrm{n})}^{-}dA$ which acts on the material within Ω_{t}^{-}. Balance of forces requires that

$$\tau_{(\mathrm{n})}^{+}(a^{+},t)dA + \tau_{(-\mathrm{n})}^{-}dA = 0 \;\rightarrow\; \tau_{(\mathrm{n})}^{+}(a^{+},t)dA - \tau_{(\mathrm{n})}^{-}dA = 0. \tag{4.9}$$

For simplicity, we write

$$\tau = \tau(a^{+},t) = \tau_{(\mathrm{n})}^{+}(a^{+},t) \tag{4.10}$$

for the traction exerted by the lower body on the upper. This traction τ may be decomposed into normal and tangential parts as

$$\tau = \tau_{\mathrm{N}} + \tau_{\mathrm{T}}, \tag{4.11}$$

where

$$\tau_{\mathrm{N}} = (n \otimes n)\tau = (\tau \cdot n)n = \tau_{\mathrm{N}} n \text{ and } \tau_{\mathrm{T}} = (1 - n \cdot n)\tau = \tau - \tau_{\mathrm{N}} n. \tag{4.12}$$

The quantity, $\sigma = -\tau_{\mathrm{N}}$ represents the normal pressure or contact pressure. We denote the magnitude of the tangential traction vector τ_{T} by

$$\bar{\tau} = \sqrt{\tau_{\mathrm{T}} \cdot \tau_{\mathrm{T}}}, \tag{4.13}$$

and call it the effective tangential traction or simply the shear stress.

Let α^+ and α^- denote the "states" of the upper and lower surfaces, respectively. These state parameters are different from the one in rate-and-state friction. They symbolically represent all the surface roughness and microstructural details of the upper and lower surfaces. We denote the state of the interface by

$$\alpha = \{\alpha^+, \alpha^-\}, \tag{4.14}$$

where α depends on the state of the upper α^+ and lower α^- surfaces, and its evolution depends on the evolution of the state of the upper surface with respect to evolution of the lower surface.

4.1.2 Two-sided description of friction

Interface friction is the ratio of the shear stress τ to normal stress σ_{n}. As the surfaces slip against each other, laboratory observations indicate that friction initially rapidly increases and then gradually drops to a residual level at steady-state (Rosakis et al., 2020). This behavior is roughly captured by the slip-weakening model, where the coefficient of friction μ evolves with slip s according to

$$\mu(s) = \mu_\infty + (\mu_0 - \mu_\infty)e^{-s/d_{\mathrm{c}}}, \tag{4.15}$$

where μ_0 and μ_∞ are the static and dynamic friction coefficient, and d_{c} is the e-folding distance over which μ_∞ is reached. The parameters μ_0, μ_∞ and d_{c} are material properties. Here we choose that the coefficient of friction is equal to the state of the interface

$$\mu = \alpha, \tag{4.16}$$

and that the slip distance is equal to the relative tangential displacement increment

$$s = \bar{u}_{\mathrm{t}}. \tag{4.17}$$

The upper material and lower material descriptions of slip-weakening friction are formulated for frames of reference (or observers) that are attached to the upper and lower surfaces, respectively. Here, we formulate an objective slip-weakening model for an arbitrary placed frame of reference. We describe friction as a function of the states of the upper and lower surfaces, each representing roughness and microstructural details for the surface. The state of the frictional behavior of a surface is characterized by the static coefficient $\alpha_0(p^{\pm}, t)$, dynamic coefficient $\alpha_\infty(p^{\pm}, t)$, characteristic slip distance over which the dynamic state is reached $d_c(p^{\pm}, t)$, and slip distance $s(p^{\pm}, t)$.

We consider two heterogeneous surfaces sliding against each other. We choose an arbitrary frame of reference on the interface, and denote it by (x, t). This frame of reference is related to the upper material point a^+ and lower material point a^- by

$$x = \Psi^+(a^+, t), \tag{4.18}$$

and

$$x = \Psi^-(a^-, t), \tag{4.19}$$

respectively, where $a^+ = \Phi^+(p^+, t)$ and $a^- = \Phi^-(p^-, t)$. We then describe interface friction in the chosen frame of reference as a multiplicative function of the states of the upper and lower surfaces. If a slippery surface is sliding against a sticky surface, the friction of the slippery surface would dominate (Rabinowicz, 1965). Here we choose the following geometric average function but ideally this would need to be determined by laboratory experiments

$$\hat{\mu}(x, t) = (\hat{\alpha}^+(x, t) \cdot \hat{\alpha}^-(x, t))^{1/2}, \tag{4.20}$$

where the evolution of the upper and lower states follows

$$\frac{\partial \hat{\alpha}^+}{\partial t}(x, t) = \frac{D\alpha^+}{Dt}(a^+, t) = \frac{\partial \alpha^+}{\partial t}(a^+, t) + \frac{\partial a^+}{\partial t}\frac{\partial \alpha^+}{\partial a^+}(a^+, t), \tag{4.21}$$

$$\frac{\partial \hat{\alpha}^-}{\partial t}(x, t) = \frac{D\alpha^-}{Dt}(a^-, t) = \frac{\partial \alpha^-}{\partial t}(a^-, t) + \frac{\partial a^-}{\partial t}\frac{\partial \alpha^-}{\partial a^-}(a^-, t), \tag{4.22}$$

respectively. The partial derivatives in the above expressions are defined by

$$\frac{\partial \alpha^+}{\partial t}(a^+,t) = -\frac{\partial s}{\partial t}(a^+,t)\frac{1}{d_c^+(a^+)}[\alpha^+(a^+,t) - \alpha_\infty^+(a^+)], \tag{4.23}$$

$$\frac{\partial \alpha^-}{\partial t}(a^-,t) = -\frac{\partial s}{\partial t}(a^-,t)\frac{1}{d_c^-(a^-)}[\alpha^-(a^-,t) - \alpha_\infty^-(a^-)], \tag{4.24}$$

$$\frac{\partial a^+}{\partial t} = \frac{\partial (\Psi^+)^{-1}}{\partial t}(x,t), \tag{4.25}$$

$$\frac{\partial a^-}{\partial t} = \frac{\partial (\Psi^-)^{-1}}{\partial t}(x,t), \tag{4.26}$$

$$\begin{aligned}\frac{\partial \alpha^+}{\partial a^+}(a^+,t) = \frac{\partial \alpha_\infty^+}{\partial a^+}(a^+,t) + [\frac{\partial \alpha_0^+}{\partial a^+}(a^+,t) - \frac{\partial \alpha_\infty^+}{\partial a^+}(a^+,t)]e^{-s(a^+,t)/d_c^+(a^+,t)} \\ + [\alpha_0^+(a^+,t) - \alpha_\infty^+(a^+,t)]e^{-s(a^+,t)/d_c^+(a^+,t)} * [\frac{s(a^+,t)(\partial d_c^+/\partial a^+(a^+,t))}{d_c^+(a^+,t)^2}],\end{aligned} \tag{4.27}$$

$$\begin{aligned}\frac{\partial \alpha^-}{\partial a^-}(a^-,t) = \frac{\partial \alpha_\infty^-}{\partial a^-}(a^-,t) + [\frac{\partial \alpha_0^-}{\partial a^-}(a^-,t) - \frac{\partial \alpha_\infty^-}{\partial a^-}(a^-,t)]e^{-s(a^-,t)/d_c^-(a^-,t)} \\ + [\alpha_0^-(a^-,t) - \alpha_\infty^-(a^-,t)]e^{-s(a^-,t)/d_c^-(a^-,t)} * [\frac{s(a^-,t)(\partial d_c^-/\partial a^-(a^-,t))}{d_c^-(a^-,t)^2}].\end{aligned} \tag{4.28}$$

The slip at the interface is defined by

$$s(a^+,t) = s(a^-,t) = \Phi^+(a^+,t) - \Phi^-(a^-,t). \tag{4.29}$$

4.1.3 Test cases

To demonstrate the need for an objective, reference-frame-independent formulation of slip-weakening friction, we analyze four cases of heterogeneous surfaces sliding against each other (Fig. 4-2). All four of these cases have a heterogeneous upper surface that degrades with slip. Note that we define a surface as degradable when it deforms or weakens with slip (finite d_c) as a result of wear formation or other plastic processes and non-degradable when it remains unaltered with slip (infinite d_c) (Rabinowicz, 1965). The heterogeneous degradable upper surface slides against a lower surface that is: (A)

continuous, homogeneous and non-degradable, (B) discontinuous and non-degradable, (C) homogeneous and degradable, and (D) heterogeneous and degradable. We show results of frictional evolution that would not have been achieved if we did not include the transport term in the objective description of friction.

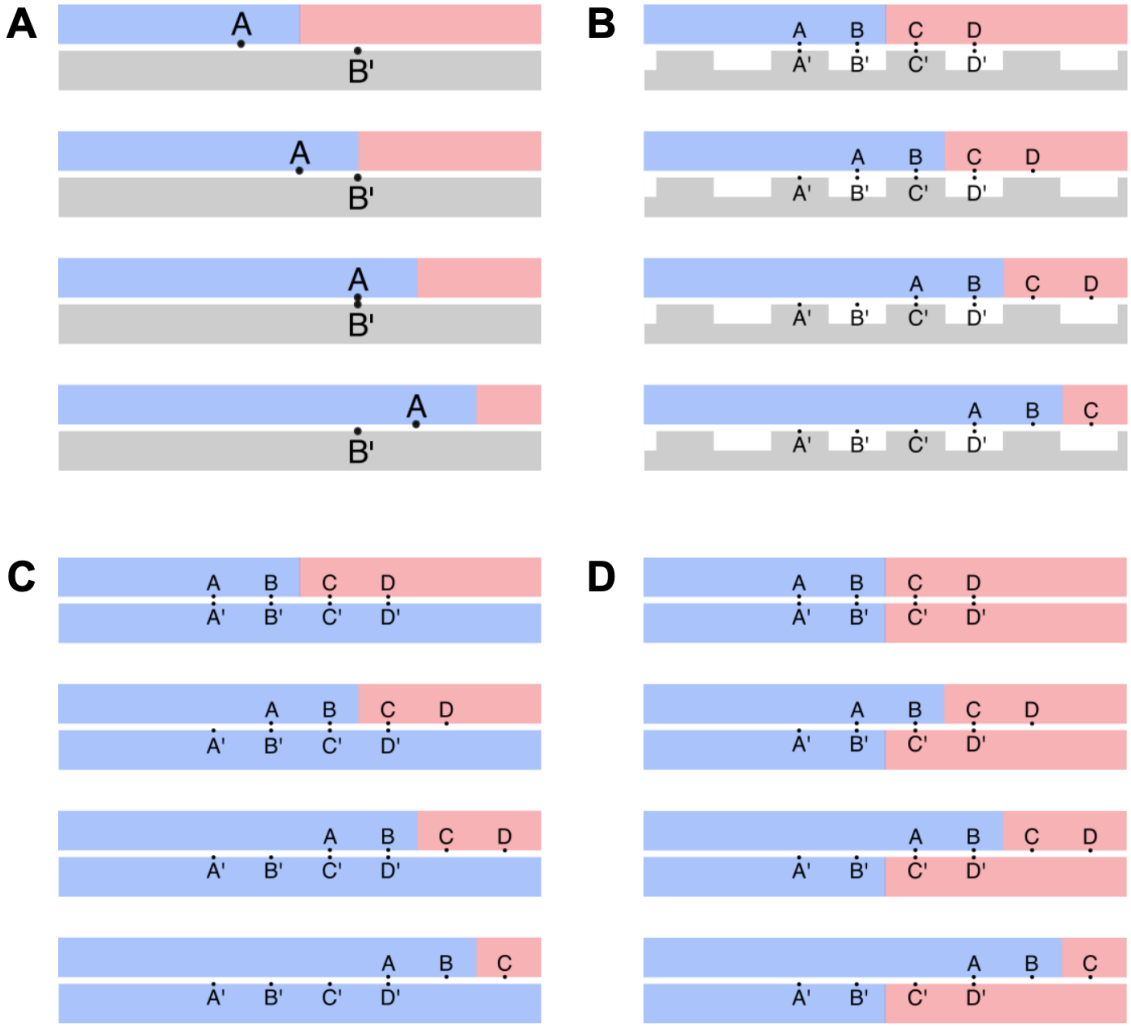

Figure 4-2: Schematic of two surfaces sliding against each other. Red and blue represent degradable surfaces with different frictional properties, and grey represents non-degradable surfaces (figures not drawn to scale).

Continuous non-degradable lower surface

We start by analyzing a simple model of single material discontinuity with slip-weakening friction law (Fig. 4-2A). Material point (A) moves with the upper surface

at constant velocity, while spatial point (B') is fixed. Note that point (A) on the upper surface is in contact with different points on the lower surface at each instant of time. We therefore need to take this into account when defining appropriate time derivatives of interface quantities or evolution of friction.

When simulating the evolution of friction at upper surface material point (A) and lower surface spatial point (B'), we obtain the curves in Fig. (4-3). Note that the variations in frictional parameters are described by smooth step functions. The curve associated with (A) follows the frictional evolution associated with left-side (blue) frictional parameters. The curve associated with (B') describes the frictional values of upper surface material points passing at each point in time. At $t = 0$, the friction evolves with right-side (red) frictional parameters. At $t = 1$, a frictional discontinuity takes place associated with the change to left-side (blue) frictional parameters. At $t = 2$, points (A) and (B') are in contact and so the frictional values are identical.

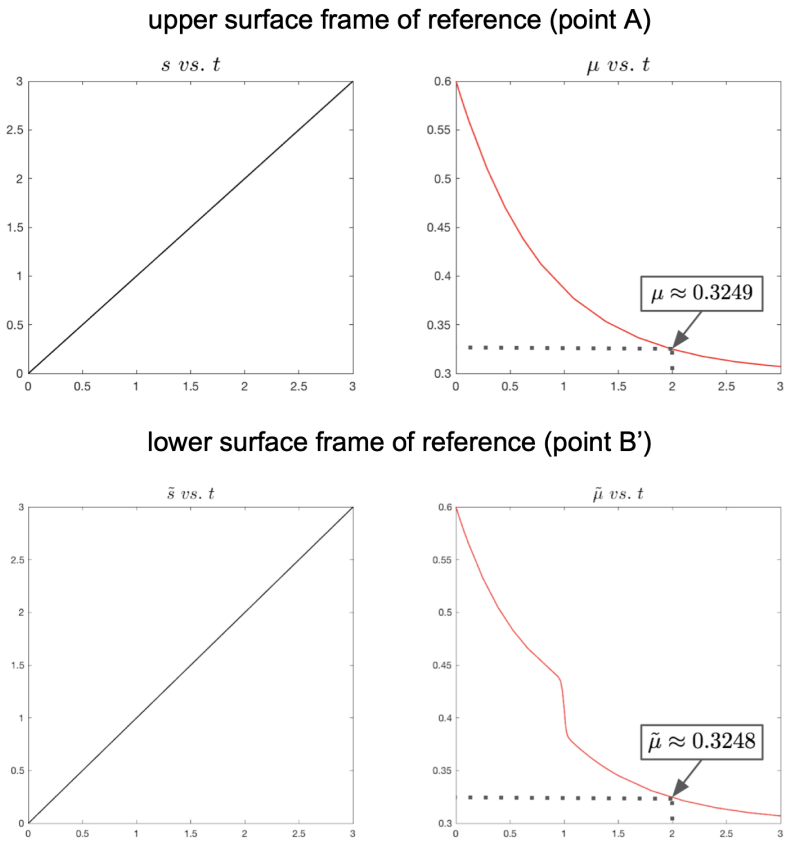

Figure 4-3: Frictional evolution of a heterogeneous degradable upper surface sliding against a continuous non-degradable lower surface.

Discontinuous non-degradable lower surface

Similar to the continuous lower surface case, we analyze a simple model of single material discontinuity with slip-weakening friction law with the difference that the lower surface is discontinuous with periodic gaps (Fig. 4-2B). Points (A,B,C,D) on the upper surface move with the upper surface at constant velocity, while points (A',B',C',D') on the lower surface are fixed.

When simulating the evolution of friction at upper surface points (A,B) and lower surface points (C',D'), we obtain the curves in Fig. 4-4. Similar to the continuous case, the variations in frictional parameters are described by smooth step functions. The curves associated with (A,B) follow the frictional evolution associated with left-side (blue) frictional parameters. The curves associated with (C',D') describe the frictional values of upper surface material points passing at each point in time. At

$t = 0$, the friction evolves with right-side (red) frictional parameters. At $t = 0.25$ and $t = 0.75$, a frictional discontinuity takes place associated with the change from right-side (red) to left-side (blue) frictional parameters for (C') and (D'), respectively. At $t = 1$, points (A,B) and (C',D') form pairs and so the frictional values are identical.

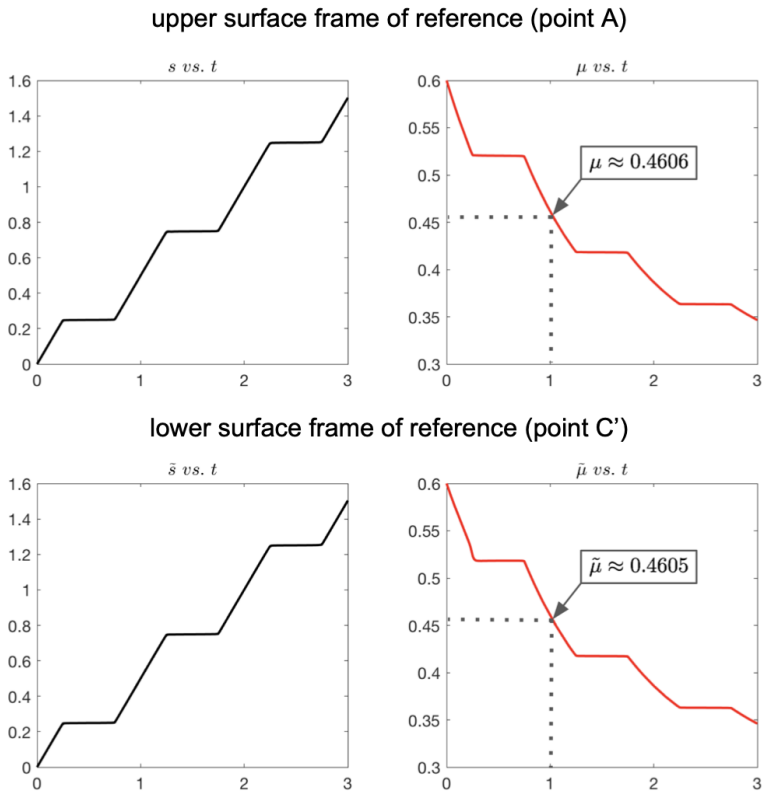

Figure 4-4: Frictional evolution of a heterogeneous degradable upper surface sliding against a discontinuous non-degradable lower surface.

Homogeneous degradable lower surface

Similar to the continuous lower surface case, we analyze a simple model of a material discontinuity with slip-weakening friction law with the difference that the lower surface is also degradable (Fig. 4-2C). Points (A,B,C,D) move with the upper surface at constant velocity, while points (A',B',C',D') are fixed.

When simulating the evolution of friction at the upper point (A) and lower surface point (C'), we obtain the curves in Fig. 4-5. The curve associated with (A) follows the

frictional evolution associated with left-side (blue/blue) frictional parameters. The curve associated with (C') describes the frictional values of upper surface material points passing at each point in time. At $t = 0$, the friction evolves with right-side (red/blue) frictional parameters. At $t = 0.25$, a frictional discontinuity takes place associated with the change from right-side (red/blue) to left-side (blue/blue) frictional parameters for (C'). At $t = 1$, points (A) and (C') form a pair and so the frictional values are identical.

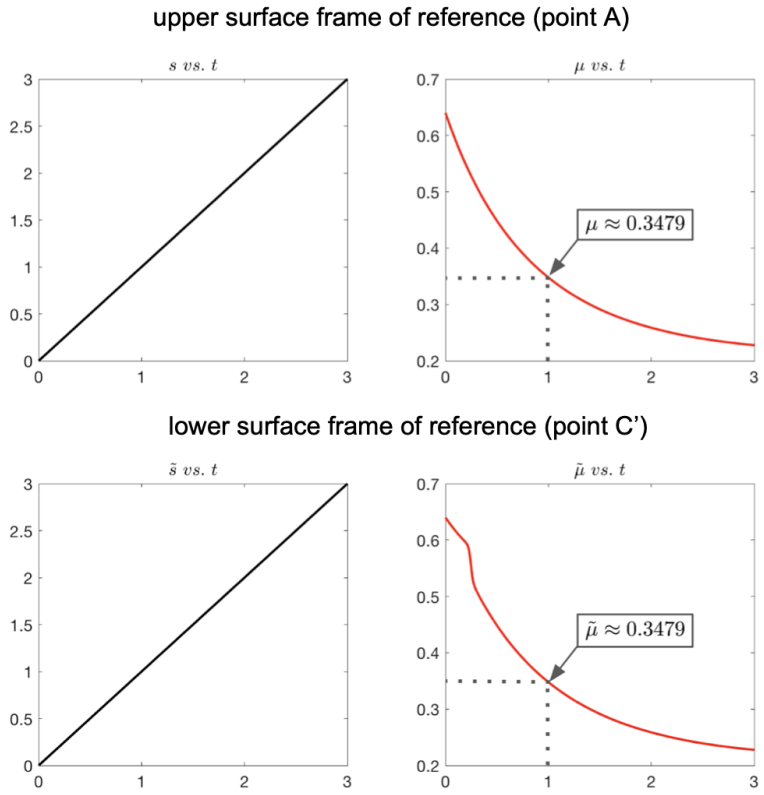

Figure 4-5: Frictional evolution of a heterogeneous degradable upper surface sliding against a homogeneous degradable lower surface.

Heterogeneous degradable lower surface

Similar to the homogeneous degradable surface case, we analyze a simple model of a material discontinuity with slip-weakening friction law with the difference that the lower surface also contains a material discontinuity (Fig. 4-2D). Again, points

(A,B,C,D) move with the upper surface at constant velocity v_0, while points (A',B',C',D') are fixed.

When simulating the evolution of friction at the upper material point (A) and lower surface spatial point (C'), we obtain the curves in Fig. 4-6. The curve associated with (A) follows the frictional evolution associated with left-slide (blue) frictional parameters of the upper surface and left (blue) right (red) sides frictional parameters of the lower surface. At $t = 0$, the friction evolves according to the (blue/blue) frictional parameters. At $t = 0.75$, a frictional discontinuity takes place associated with the change from (blue/blue) to (blue/red) frictional parameters. The friction coefficient increases with time as a result of heterogeneity. Similarly, the curve associated with (C') depends on both the upper and lower surface frictional parameters. At $t = 0$, the friction evolves with (red/red) frictional parameters. At $t = 0.25$, a frictional discontinuity takes place associated with the change from right-side (red/red) to left-side (blue/red) frictional parameters. At $t = 1$, points (A) and (C') form a pair and so the frictional values are identical.

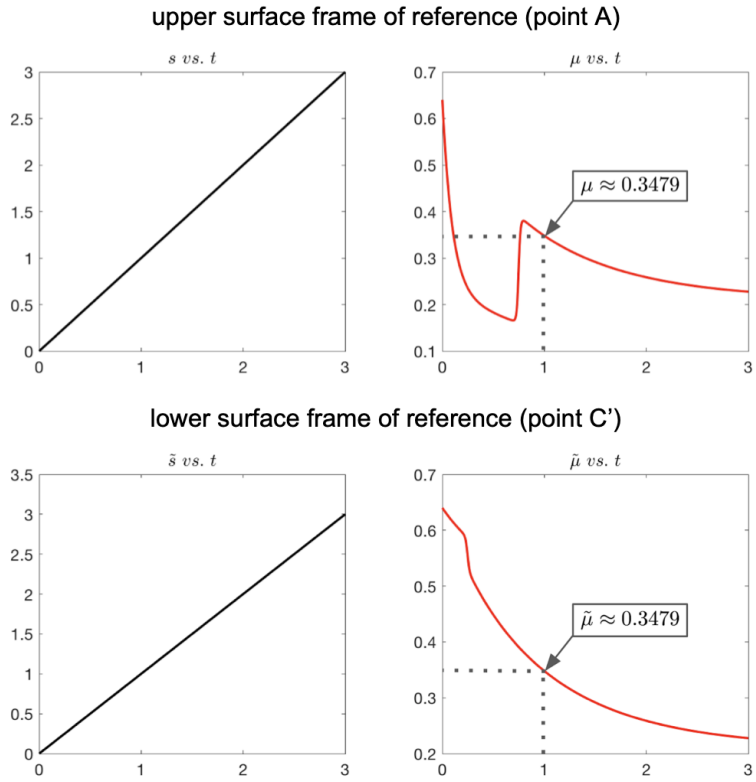

Figure 4-6: Frictional evolution of a heterogeneous degradable upper surface sliding against a heterogeneous degradable lower surface.

4.2 Stick-slip from heterogeneous Coulomb friction

Brace and Byerlee (1966) recognized that earthquakes are the result of stick-slip frictional instabilities. The seismic rupture is the slip, and the stick is the interseismic period of elastic strain accumulation. Observed stress drops represent release of a small fraction of the stress supported by the rock surrounding the earthquake focus. Since then, many studies have contributed to understanding the nature of these instabilities and the factors controlling them. Experiments have been performed with many rock types, with and without various fault gouge layers, at a range of slip rates, confining pressures, pore pressures, temperatures, and in machines with different geometries and stiffness (Marone, 1998; Scholz, 2002). These experimental observations led to the development of rate-and-state friction laws—the gold standard in modeling earthquake dynamics (Dieterich, 1979b; Ruina, 1983; Scholz, 1998).

Stick-slip, in general, is caused by variations in frictional resistance as a function of some other variable (Rabinowicz, 1965; Mate, 2008). One variable is velocity, in which the instability originates from a pure velocity-weakening friction (Carlson and Langer, 1989). In this case, there is a high static friction when the surfaces are at rest and, once shear stress exceeds this value, the surfaces slide with a lower kinetic friction. Another variable is time, in which the static friction increases with it while the kinetic friction remains relatively constant (Rabinowicz, 1958; Ringoot et al., 2021). If the increase in static friction during a stick phase is greater than the variation in kinetic friction during slip, repeated stick-slip cycles occur. Rate-and-state laws combine both velocity- and time-dependence of friction. A third variable, and a largely overlooked one in studies of rock friction and earthquakes, is position. The instability is caused by the frictional resistance varying as a function of position over the sliding surface.

Topological stick-slip is observed in the macroscopic sliding of metals (Rabinowicz, 1965), as well as in atomic force microscopy experiments where the intermittent motion of a tungsten tip is a measure of the atomic-scale corrugations on a graphite surface (Mate et al., 1987). In the sliding of metals, fluctuations of friction arise from junctions growth and thinning, and alternating lubricant coverage. In the second case, friction fluctuates with the same periodicity as the crystal lattice on the surface. This type of stick-slip, however, has not yet been experimentally studied in rocks and only one theoretical study exists (Nur, 1978). It suggests that the slip is caused by irregular surface roughness and uses nonuniform friction to explain it, but many of the arguments are only qualitative. Here we revive this approach to understanding stick-slip motion, develop a position-dependent friction framework, and analyze the resulting slip dynamics using a spring-slider model.

4.2.1 Position-dependent friction

Rock surfaces, irrespective of their mode of formation, contain irregularities or deviations from a prescribed geometrical form at all scales (Fig. 4-7) (Scholz, 2002; Bhushan, 1998). The protrusions on the surfaces are referred to as asperities and

the dimples are referred to as valleys. When two nominally flat surfaces are placed in contact, surface roughness causes contact to occur at discrete contact spots or junctions.

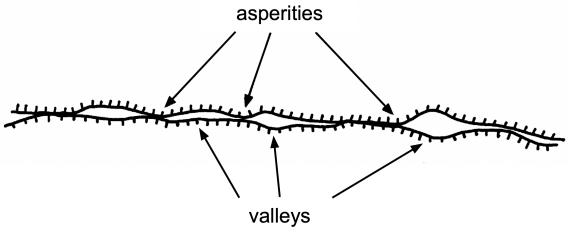

Figure 4-7: Schematic of irregular contacting surfaces (modified from Scholz (2002)).

Following the framework for interface friction by Anand (1993), we let α^+ and α^- denote the states of the upper and lower surfaces, respectively. These state parameters symbolically represent all the roughness and microstructural details of the upper and lower surfaces. We denote the state of the interface by $\alpha = \{\alpha^+, \alpha^-\}$. We define the frictional resistance of the interface by $\tau_{\rm f} = f(\sigma', \alpha)$, where $\tau_{\rm f}$ is a scalar with dimensions of stress. It represents an averaged resistance to macroscopic slip at a given normal effective stress σ' and state α of the interface. One of the open problems for interface constitutive models is to provide a realistic micro-mechanical description for the state of the interface and its evolution. Here we replace α by a mesoscopic scalar variable μ, which is the Coulomb friction coefficient.

To obtain an objective or frame-indifferent formulation of Coulomb friction between irregular surfaces, we describe the interface at a point x in terms of upper and lower surface points a^+ and a^-. Using the interface frame of reference, the state of the upper and lower surfaces may be written as $\alpha^+(x,t) = \alpha^+(\Psi^+(a^+,t),t)$ and $\alpha^-(x,t) = \alpha^-(\Psi^-(a^-,t),t)$, where Ψ^+ and Ψ^- are transformation functions. We then describe friction as a multiplicative function of the states of the upper and lower surfaces. We choose the geometric average, $\mu(x,t) = \sqrt{\alpha^+(x,t) * \alpha^-(x,t)}$, but ideally this constitutive relation would need to be determined by laboratory experiments. Diagrams of the state of the upper surface, the state of the lower surface, and the resulting friction of the interface as a function of position and time are illustrated

in Figure 4-8. If an asperity is sliding over an asperity, the friction at the interface is maximum, whereas if a valley is sliding over a valley or an asperity, the friction is minimum. The averaged resistance to slip at a given position on the interface is illustrated in Figure 4-9. The high values on the curve represent contact spots or junctions and the low values represent no or weak contact. Friction is approximated by a cosine function, where its amplitude represents the degree of heterogeneity and wavelength represents the length of a patch.

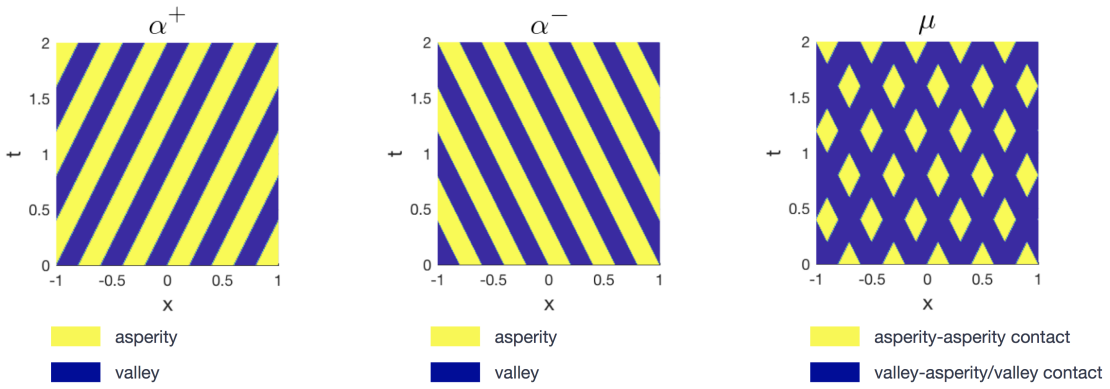

Figure 4-8: Characteristic space (x,t) of the state of the upper surface, the state of the lower surface, and the resulting friction of the interface as a function of time and position.

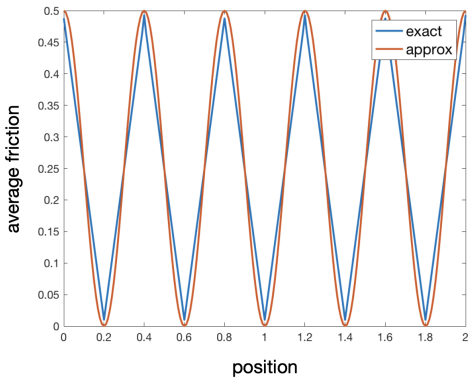

Figure 4-9: Exact and approximate averaged resistance to slip at a given position on the interface.

This shows how the interaction between irregular surfaces results in heterogeneous Coulomb friction along the interface. Spatial variations in lithostatic load, pore pres-

sure, rock type or physical properties would produce a similar effect (Kirkpatrick et al., 2020; Rabinowicz, 1965). In this case, asperities would be the high-strength or sticky patches along surfaces and valleys would be the low-strength or slippery ones.

4.2.2 Spring-slider model with heterogeneous Coulomb friction

Consider a slider of unit base area that is pulled by a spring with stiffness k_s whose end is constrained to move at a steady slip rate (Fig. 4-10). The stiffness k accounts for the elastic interaction of the sliding surface with the surrounding rock. The slider has a mass m to incorporate the effect of inertia and is attached to a damper with coefficient $\sqrt{k_\mathrm{s} m}$ to incorporate the effect of seismic radiation—see section 3.3 for more details. The slider moves over a heterogeneous surface that is described by a Coulomb friction varying as a function of position.

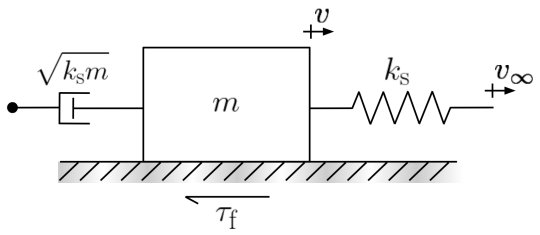

Figure 4-10: Spring-slider model of a heterogeneous fault.

The equations describing the dynamic motion of the spring-slider, in dimensional form, are

$$\dot{U} = V_\infty - V, \tag{4.30}$$

$$\dot{V} = \frac{1}{m}\left[k_\mathrm{s} U - F(U)\Sigma' - \sqrt{k_\mathrm{s} m} V\right], \tag{4.31}$$

where U is the relative displacement between the load point and the slider, V_∞ is the loading velocity, V is slip rate, k_s is the shear stiffness, and Σ' is the normal effective stress. In the spring-slider model, there is no difference between position-dependent friction and displacement-dependent friction. We can therefore describe friction as a

function of the relative displacement, $F(U) = A(\cos B(U - U_0) + 1)$. Amplitude A represents the degree of heterogeneity and wavelength $2\pi/B$ represents the length of a patch.

Choosing the following characteristic quantities: $t_c = 1/(BV_\infty)$, $v_c = V_\infty$, $u_c = 1/B$, $\mu_c = A$, and $\sigma_c = \Sigma_0'$, the equations describing the dynamic motion of the system, in dimensionless form, become

$$\dot{u} = v_\infty - v, \tag{4.32}$$

$$\dot{v} = \frac{1}{\epsilon^2}\left[u - \frac{1}{\kappa}\mu(u)\sigma' - \epsilon v\right], \tag{4.33}$$

where $\mu(u) = \cos(u - u_0) + 1$, $\kappa = k_s/(BA\Sigma_0')$, and $\epsilon = BV_\infty/\sqrt{k_s/m}$. Parameter κ is the normalized shear stiffness and parameter ϵ is the normalized oscillation period or the ratio of the natural vibration period of the analogous freely slipping system to the frictional fluctuation period.

4.2.3 Slip dynamics

To analyze the resulting slip dynamics, we simulate the equations of motion of the spring-slider system (Eqs. (4.32)-(4.33)) with the following initial conditions: $u(0) = -\sigma'/\kappa$, $v(0) = 0$. The coupled ordinary differential equations are solved in MATLAB using the `ode15s` solver for stiff systems. We find that the simple heterogeneous Coulomb friction gives rise to complex slip patterns, ranging from stable creep to unstable regular stick-slip and slow slip. Representative results are shown in Figures 4-11, 4-12, and 4-13. The simulation of creep (Fig. 4-11) is performed using parameter values $\kappa = 2$ and $\epsilon = 0.01$, regular stick-slip (Fig. 4-12) is performed using $\kappa = 0.1$ and $\epsilon = 0.01$, and slow slip (Fig. 4-13) is performed using $\kappa = 0.01$ and $\epsilon = 10$.

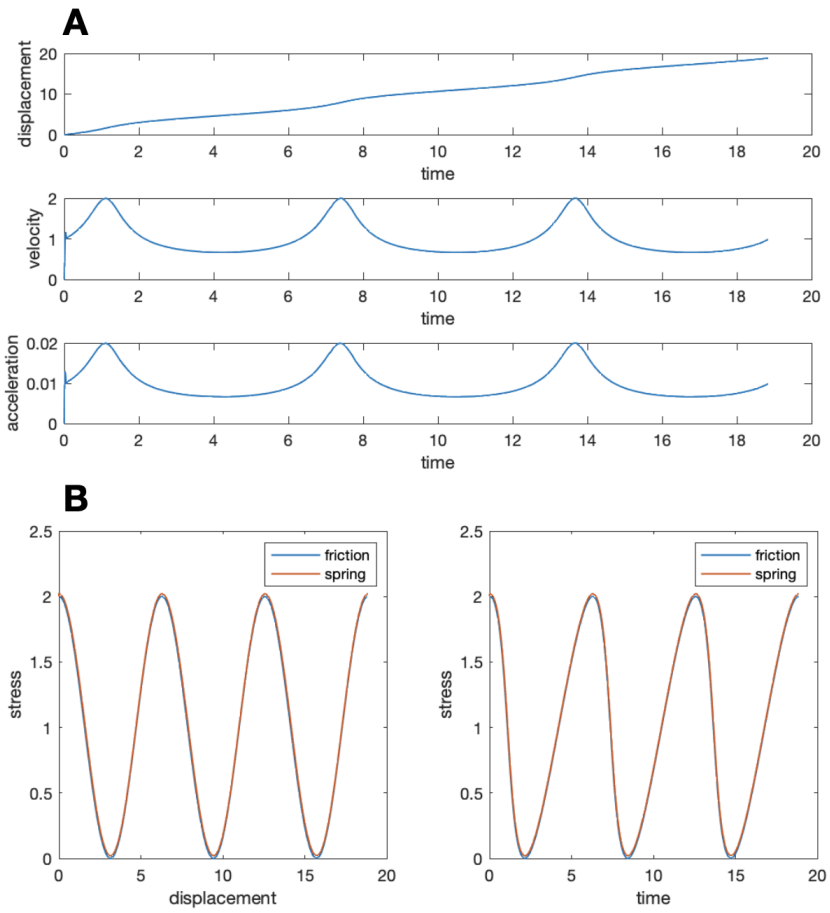

Figure 4-11: Creep motion of the spring-slider system with dimensionless parameters $\kappa = 2$, $\epsilon = 0.01$.

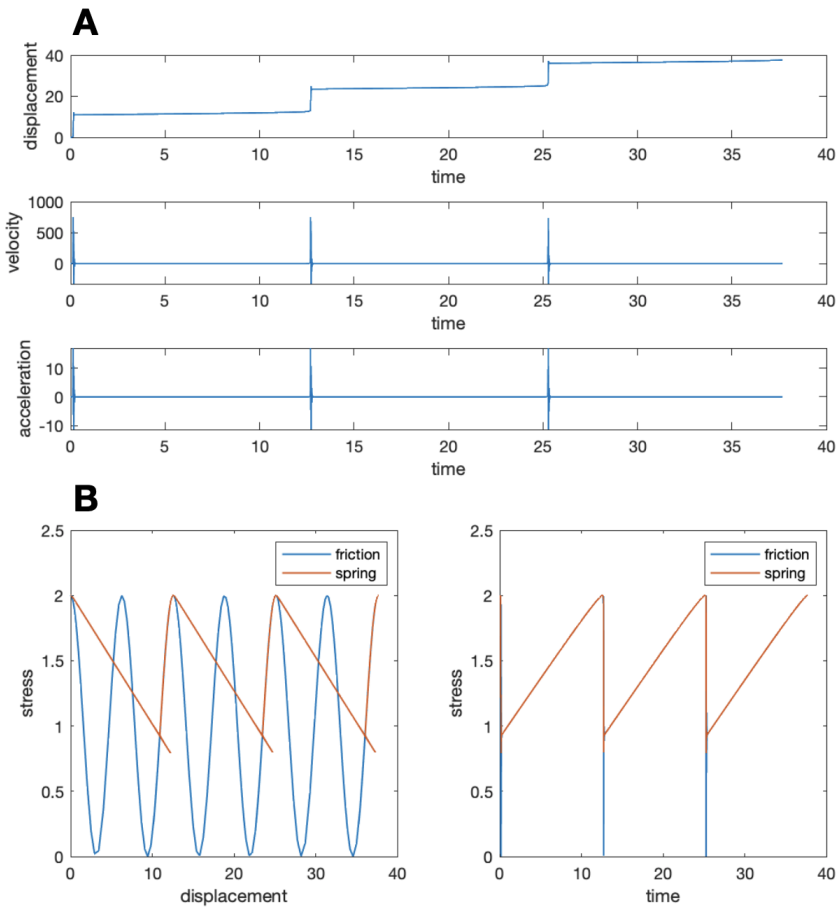

Figure 4-12: Regular stick-slip motion of the spring-slider system with dimensionless parameters $\kappa = 0.1$, $\epsilon = 0.01$.

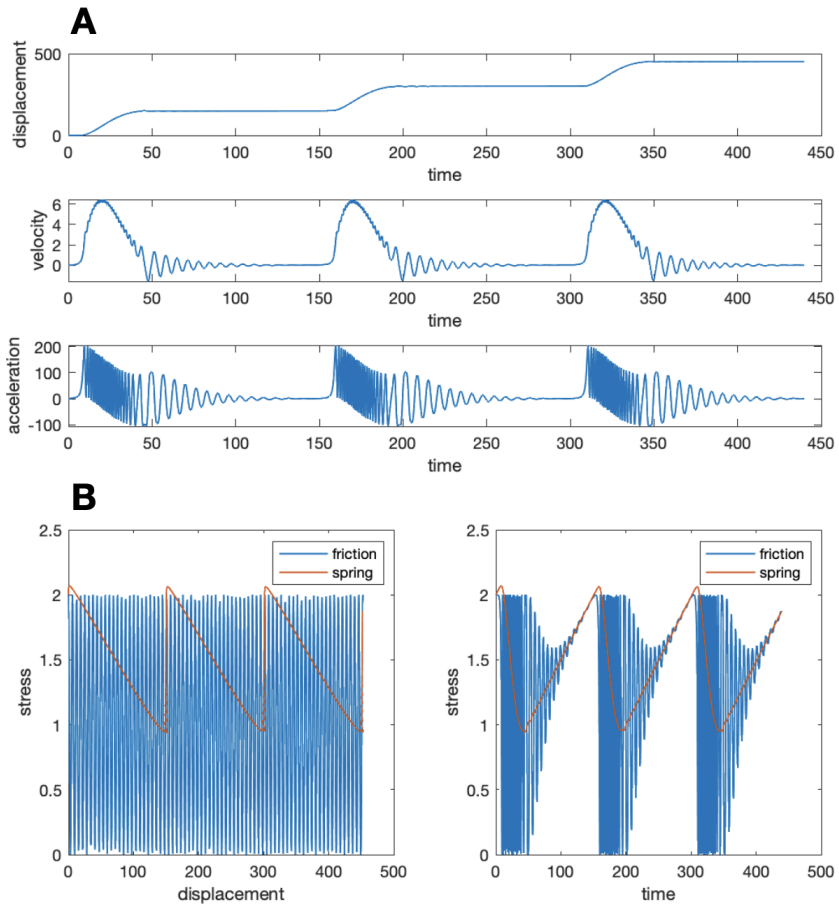

Figure 4-13: Slow slip motion of the spring-slider system with dimensionless parameters $\kappa = 0.01$, $\epsilon = 10$.

When the spring stretches sufficiently, the slider creeps slowly until it reaches a peak in frictional resistance. In the case where stiffness is high and oscillation period is low, there is no unstable motion—only accelerated or decelerated creep relative to the loading rate (Fig. 4-11). In the case where both stiffness and oscillation period are low, unstable stick-slip motion occurs. The excess of spring force over the frictional resistance causes the slider to accelerate rapidly. It moves over two friction fluctuations, overshoots, and decelerates when further relaxation of the spring becomes too difficult. At this point, the frictional resistance cannot be overcome. The slider creeps until it reaches a peak in frictional resistance, and the stick-slip cycle repeats (Fig. 4-12). In the case where stiffness is low but oscillation period is high, unstable motion also occurs. The dynamics are similar to the previous case, but the slip is much slower. It is also interesting to note that the velocity and particularly the acceleration time functions show irregularities due to the variable friction (Fig. 4-13).

To gain further insights into the influence of heterogeneity on slip motion, we exhaustively explore the system dynamics as a function of the normalized shear stiffness $\kappa = k_s/(BA\Sigma_0')$ and normalized oscillation period $\epsilon = BV_\infty/\sqrt{k_s/m}$. Each point on the phase diagram shown in Fig. 4-14A represents the maximum slip velocity of a different simulation run with a particular shear stiffness and a particular oscillation period. Similarly, each point on the phase diagram shown in Fig. 4-14B represents the maximum slip distance. We observe three regimes: a creep regime (low slip rate, low-to-medium slip distance), a regular stick-slip regime (high slip rate, medium-to-high slip distance), and a slow-slip regime (medium slip rate, high slip distance).

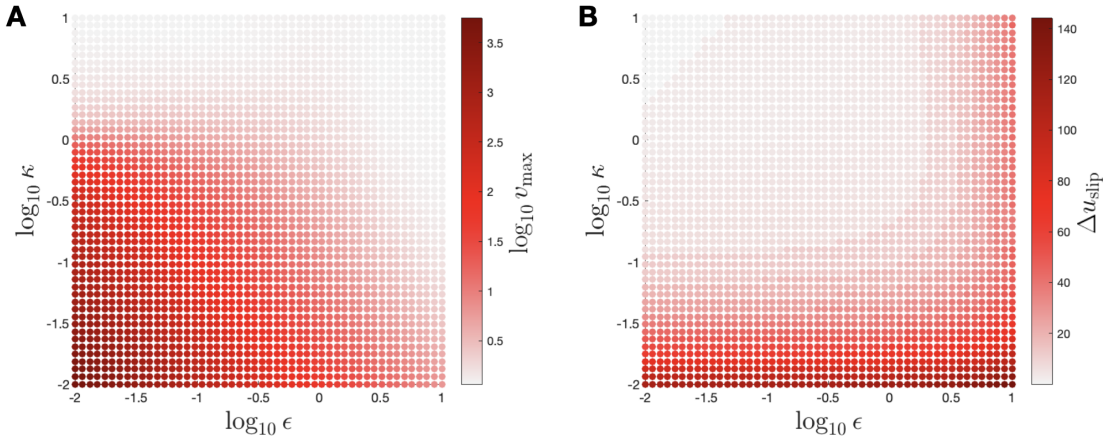

Figure 4-14: Phase diagrams of slip rate (A) and slip distance (B) as a function of normalized shear stiffness κ and normalized oscillation period ϵ.

The transition between the different regimes depends on the heterogeneity of the interface and on the elastic and internal properties of the spring-slider. Stable slip occurs whenever frictional resistance and spring loading balances, and unstable slip occurs whenever a change of frictional resistance with sliding occurs at a rate greater than the loading system is capable of following (Byerlee, 1970). That is, motion is by creep when the normalized shear stiffness of the loading system is higher than a critical value ($\kappa > \kappa_{\text{crit}}$) given by

$$\kappa_{\text{crit}} = \left.\frac{\partial \mu(u)}{\partial u}\right|_{\max} \sigma', \tag{4.34}$$

and is by regular stick-slip or slow slip otherwise ($\kappa < \kappa_{\text{crit}}$). The softer the spring, the greater the number of friction fluctuations over which the slider moves (Fig. 4-15). The duration of slip is controlled by the normalized oscillation period. Motion is by regular stick-slip when the natural vibration period is much lower than the frictional fluctuation period ($\epsilon \ll 1$), and is by slow slip otherwise ($\epsilon \gg 1$). This shows that our framework for position-dependent friction is not only capable of modeling stable and unstable slip, but also the transition between regular stick-slip and slow slip.

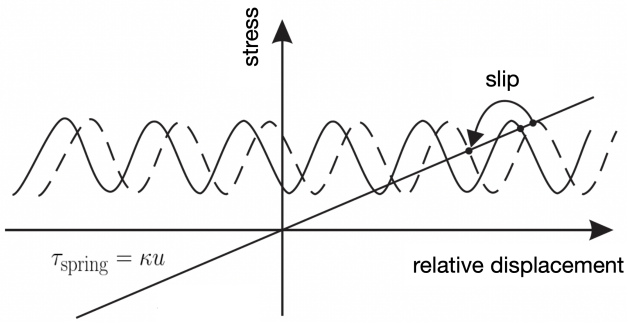

Figure 4-15: Spring loading and frictional resistance for two slider positions (modified from Mate (2008)).

Chapter 5

Conclusions

Understanding the physical mechanisms that underpin the link between fluid injection and seismicity is essential in efforts to mitigate the seismic risk associated with subsurface technologies (National Research Council, 2013). In Chapter 2, we develop a poroelastic model of frictional slip based on rate-and-state friction in the manner of spring–sliders, and analyze conditions for the emergence of stick-slip frictional instability by carrying out nonlinear simulations and a linear stability analysis. We find that frictional slip depends largely on the rate of increase in pore pressure rather than its magnitude. Fluid pressurization can significantly increase the critical stiffness, and thus increase the risk of triggering earthquakes. This may explain several injection-induced seismicity observations (Frohlich, 2012; Weingarten et al., 2015; Healy et al., 1968; Improta et al., 2015; Langenbruch and Zoback, 2016; Cuenot et al., 2008; Kim, 2013; Tang et al., 2018). Our model implies that, for the same cumulative volume of injected fluid, an abrupt high-rate injection protocol is likely to increase the seismic risk whereas a gradual step-up protocol is likely to decrease it.

In Chapter 3, we perform an energy analysis of the full anthropogenic earthquake cycle using the same framework of a spring poroslider and rate-and-state friction (Alghannam and Juanes, 2020). A key element of the analysis is incorporating the seismic radiation within the spring poroslider using a precisely-defined viscous damper (coefficient equal to the square root of spring stiffness times mass). We then use it to study fluid injection and assess its effects on the energy partitioning during induced

and triggered earthquakes. The aim of this study is to gain physical insights on the influence of fluid injection on energy partitioning during the earthquake cycle. We find that event size indicators (radiated energy, seismic efficiency, stress drop, and total slip) are directly influenced by the rate of fluid pressurization. The higher the rate of fluid pressurization at the time of the earthquake, the higher the values of event size indicators. This effect is more pronounced at high injection rates. The framework of this work could be generalized to study energy dissipation mechanisms in fluid-saturated materials to understand the energy budget of slow and silent earthquakes (Im et al., 2020). It could also be used to study dilatancy and compaction in a fluid-infiltrated fault, and asses their contributions to the seismic energy budget (Segall and Rice, 1995). This would facilitate making further advances towards understanding the influence of fluid pressure on the mechanics of earthquakes.

Fault zones in nature are heterogeneous in material and complex in geometry with multiple slip surfaces and deformation zones (Blanpied et al., 1991; Scholz, 1988). They also exhibit large spatial variations in pore pressure (Kirkpatrick et al., 2020; Rabinowicz, 1965). To bridge the gap between the idealized spring-poroslider and natural faults, in Chapter 4, we extend the model to study the effect of heterogeneity on the dynamics of frictional faults. In particular, we develop an objective or frame-independent formulation of frictional contact between heterogeneous surfaces. We describe friction as a function of the states of the upper and lower surfaces, each representing roughness and microstructual details for the surface. We then average the heterogeneous stress and frictional parameters to obtain a large scale representation of interface friction. By analyzing the resulting slip dynamics using a spring slider model, we find that a simple heterogeneous Coulomb friction can give rise to complex slip patterns, ranging from creep to regular stick-slip and slow earthquakes. Our formulation provides a complementary, or perhaps an alternative, framework to rate-and-state friction to modeling the dynamics of earthquakes.

This thesis examines how the rate of fluid injection influences the propensity and potential damage of induced and triggered earthquakes, and how the temporal variations in fluid pressure and and spatial heterogeneity in friction control the mechanics

of earthquakes. Our findings, as a whole, could ultimately lead to new design and strategies that mitigate or minimize the seismic risk associated with a wide range of subsurface operations, from hydraulic fracturing and geothermal energy extraction to wastewater injection and geologic CO_2 sequestration. This thesis also highlights the need to perform further research in the following areas:

• Fluid pressure effect on dynamic friction: Natural faults are typically viewed as rock surfaces filled with wear detritus, called fault gouge. There is currently no friction model that takes into account the effect of fluid pressurization on both the real area of contact and frictional properties in gouge-filled rock surfaces. To understand the effect of fluid pressurization on the evolution of dynamic friction, more laboratory experiments are needed to (1) identify dominant physical mechanisms governing the processes of sliding between bare rock surfaces and shearing gouge materials, and (2) model them holistically.

• Microscopic basis of friction: One of the open problems for interface constitutive models in the field of earthquake mechanics or, more broadly, tribology is to provide a realistic micro-mechanical description for the state of the interface and its evolution. It is needed to (1) describe the microstructural details of rough surfaces using statistical and deterministic methods, and (2) understand the mechanisms governing the microscopic behavior of fault gouge or wear particles.

• Multiscale modeling of frictional sliding and fault poromechanics: Earthquake source and faulting processes involve multiple spatial and temporal scales, where processes that occur at a certain scale can govern the behavior in other scales. Modeling multiscale processes is a major challenge across all fields of science and engineering. To help address it in the field of earthquakes, it is needed to develop solution frameworks for (1) upscaling of heterogeneous or non-planar interfaces, and (2) long-term quasi-static loading histories with occasional rapid slip events.

Bibliography

Albano, M., Barba, S., Tarabusi, G., Saroli, M., and Stramondo, S. (2017). Discriminating between natural and anthropogenic earthquakes: Insights from the Emilia Romagna (Italy) 2012 seismic sequence. *Scientific Reports*, 7(1):1–14.

Albaric, J., Oye, V., Langet, N., Hasting, M., Lecomte, I., Iranpour, K., Messeiller, M., and Reid, P. (2014). Monitoring of induced seismicity during the first geothermal reservoir stimulation at Paralana, Australia. *Geothermics*, 52:120–131.

Aldam, M., Bar-Sinai, Y., Svetlizky, I., Brener, E., Fineberg, J., and Bouchbinder, E. (2016). Frictional sliding without geometrical reflection symmetry. *Physical Review X*, 6(4):041023.

Aldam, M., Xu, S., Brener, E., Ben-Zion, Y., and Bouchbinder, E. (2017). Nonmonotonicity of the frictional bimaterial effect. *Journal of Geophysical Research: Solid Earth*, 122(10):8270–8284.

Alghannam, M. and Juanes, R. (2020). Understanding rate effects in injection-induced earthquakes. *Nature Communications*, 11(3053):1–6.

Anand, L. (1993). A constitutive model for interface friction. *Computational Mechanics*, 12(4):197–213.

Baisch, S., Bohnhoff, M., Ceranna, L., Tu, Y., and Harjes, H.-P. (2002). Probing the crust to 9-km depth: Fluid-injection experiments and induced seismicity at the KTB superdeep drilling hole, Germany. *Bulletin of the Seismological Society of America*, 92(6):2369–2380.

Baisch, S., Weidler, R., Vörös, R., Wyborn, D., and De Graaf, L. (2006). Induced seismicity during the stimulation of a geothermal HFR reservoir in the Cooper Basin, Australia. *Bulletin of the Seismological Society of America*, 96(6):2242–2256.

Bar-Sinai, Y., Spatschek, R., Brener, E., and Bouchbinder, E. (2013). Instabilities at frictional interfaces: Creep patches, nucleation, and rupture fronts. *Physical Review E*, 88(6):060403.

Barbour, A., Norbeck, J., and Rubinstein, J. (2017). The effects of varying injection rates in Osage County, Oklahoma, on the 2016 M_w 5.8 Pawnee earthquake. *Seismological Research Letters*, 88(4):1040–1053.

Barnhart, W., Murray, J., Briggs, R., Gomez, F., Miles, C. P., Svarc, J., Riquelme, S., and Stressler, B. (2016). Coseismic slip and early afterslip of the 2015 Illapel, Chile, earthquake: Implications for frictional heterogeneity and coastal uplift. *Journal of Geophysical Research: Solid Earth*, 121(8):6172–6191.

Beeler, N. (2001). Stress drop with constant, scale independent seismic efficiency and overshoot. *Geophysical Research Letters*, 28(17):3353–3356.

Bekefi, G. and Barrett, A. (1977). *Electromagnetic vibrations, waves, and radiation*. MIT Press.

Bhushan, B. (1998). Contact mechanics of rough surfaces in tribology: Multiple asperity contact. *Tribology Letters*, 4(1):1–35.

Blanpied, M., Lockner, D., and Byerlee, J. (1991). Fault stability inferred from granite sliding experiments at hydrothermal conditions. *Geophysical Research Letters*, 18(4):609–612.

Block, L., Wood, C., Yeck, W., and King, V. (2014). The 24 January 2013 M_L 4.4 earthquake near Paradox, Colorado, and its relation to deep well injection. *Seismological Research Letters*, 85(3):609–624.

Boatwright, J. and Choy, G. (1986). Teleseismic estimates of the energy radiated by shallow earthquakes. *Journal of Geophysical Research: Solid Earth*, 91(B2):2095–2112.

Bourouis, S. and Bernard, P. (2007). Evidence for coupled seismic and aseismic fault slip during water injection in the geothermal site of Soultz (France), and implications for seismogenic transients. *Geophysical Journal International*, 169(2):723–732.

Brace, W. and Byerlee, J. (1966). Stick-slip as a mechanism for earthquakes. *Science*, 153(3739):990–992.

Brantut, N. and Viesca, R. (2017). The fracture energy of ruptures driven by flash heating. *Geophysical Research Letters*, 44(13):6718–6725.

Burridge, R. and Knopoff, L. (1967). Model and theoretical seismicity. *Bulletin of the Seismological Society of America*, 57(3):341–371.

Byerlee, J. (1970). The mechanics of stick-slip. *Tectonophysics*, 9(5):475–486.

Byerlee, J. and Brace, W. (1972). Fault stability and pore pressure. *Bulletin of the Seismological Society of America*, 62(2):657–660.

Candela, T., Renard, F., Bouchon, M., Brouste, A., Marsan, D., Schmittbuhl, J., and Voisin, C. (2009). Characterization of fault roughness at various scales: Implications of three-dimensional high resolution topography measurements. In *Mechanics, Structure and Evolution of Fault Zones*. Springer.

Cappa, F., Scuderi, M., Collettini, C., Guglielmi, Y., and Avouac, J.-P. (2019). Stabilization of fault slip by fluid injection in the laboratory and in situ. *Science Advances*, 5(3):eaau4065.

Carlson, J. and Langer, J. (1989). Properties of earthquakes generated by fault dynamics. *Physical Review Letters*, 62(22):2632.

Childs, C., Manzocchi, T., Walsh, J., Bonson, C., Nicol, A., and Schöpfer, M. (2009). A geometric model of fault zone and fault rock thickness variations. *Journal of Structural Geology*, 31(2):117–127.

Childs, C., Walsh, J., and Watterson, J. (1997). Complexity in fault zone structure and implications for fault seal prediction. In *Norwegian Petroleum Society Special Publications*. Elsevier.

Cocco, M., Bizzarri, A., and Tinti, E. (2004). Physical interpretation of the breakdown process using a rate-and state-dependent friction law. *Tectonophysics*, 378(3-4):241–262.

Cooke, M. and Murphy, S. (2004). Assessing the work budget and efficiency of fault systems using mechanical models. *Journal of Geophysical Research: Solid Earth*, 109(B10).

Cornet, F., Helm, J., Poitrenaud, H., and Etchecopar, A. (1997). Seismic and aseismic slips induced by large-scale fluid injections. *Pure and Applied Geophysics*, 150(3-4):563–583.

Cuenot, N., Dorbath, C., and Dorbath, L. (2008). Analysis of the microseismicity induced by fluid injections at the EGS site of Soultz-sous-Forêts (Alsace, France): Implications for the characterization of the geothermal reservoir properties. *Pure and Applied Geophysics*, 165(5):797–828.

Dahlen, F. (1977). The balance of energy in earthquake faulting. *Geophysical Journal International*, 48(2):239–261.

Davis, S. and Pennington, W. (1989). Induced seismic deformation in the Cogdell oil field of West Texas. *Bulletin of the Seismological Society of America*, 79(5):1477–1495.

De Barros, L., Cappa, F., Guglielmi, Y., Duboeuf, L., and Grasso, J.-R. (2019). Energy of injection-induced seismicity predicted from in-situ experiments. *Scientific Reports*, 9(1):1–11.

Deichmann, N. and Giardini, D. (2009). Earthquakes induced by the stimulation of an enhanced geothermal system below Basel (Switzerland). *Seismological Research Letters*, 80(5):784–798.

Dempsey, D., Ellis, S., Archer, R., and Rowland, J. (2012). Energetics of normal earthquakes on dip-slip faults. *Geology*, 40(3):279–282.

Diehl, T., Kissling, E., Herwegh, M., and Schmid, S. (2021). Improving absolute hypocenter accuracy with 3D Pg and Sg body-wave inversion procedures and application to earthquakes in the Central Alps region. *Journal of Geophysical Research: Solid Earth*, 126(12):e2021JB022155.

Dieterich, J. (1979a). Modeling of rock friction: 1. Experimental results and constitutive equations. *Journal of Geophysical Research: Solid Earth*, 84(B5):2161–2168.

Dieterich, J. (1979b). Modeling of rock friction: 2. Simulation of preseismic slip. *Journal of Geophysical Research: Solid Earth*, 84(B5):2169–2175.

Dieterich, J. and Linker, M. (1992). Fault stability under conditions of variable normal stress. *Geophysical Research Letters*, 19(16):1691–1694.

Duboeuf, L., De Barros, L., Cappa, F., Guglielmi, Y., Deschamps, A., and Seguy, S. (2017). Aseismic motions drive a sparse seismicity during fluid injections into a fractured zone in a carbonate reservoir. *Journal of Geophysical Research: Solid Earth*, 122(10):8285–8304.

Ellsworth, W. (2013). Injection-induced earthquakes. *Science*, 341(6142):1225942.

Evans, D. (1966). The Denver area earthquakes and the Rocky Mountain Arsenal disposal well. *The Mountain Geologist*, 3(1):23–36.

Evans, K., Zappone, A., Kraft, T., Deichmann, N., and Moia, F. (2012). A survey of the induced seismic responses to fluid injection in geothermal and CO_2 reservoirs in Europe. *Geothermics*, 41:30–54.

French, M., Zhu, W., and Banker, J. (2016). Fault slip controlled by stress path and fluid pressurization rate. *Geophysical Research Letters*, 43(9):4330–4339.

Frohlich, C. (2012). Two-year survey comparing earthquake activity and injection-well locations in the Barnett Shale, Texas. *Proceedings of the National Academy of Sciences*, 109(35):13934–13938.

Galis, M., Ampuero, J., Mai, M., and Cappa, F. (2017). Induced seismicity provides insight into why earthquake ruptures stop. *Science Advances*, 3(12):eaap7528.

Goebel, T. and Brodsky, E. (2018). The spatial footprint of injection wells in a global compilation of induced earthquake sequences. *Science*, 361(6405):899–904.

Goodfellow, S., Nasseri, M., Maxwell, S., and Young, R. (2015). Hydraulic fracture energy budget: Insights from the laboratory. *Geophysical Research Letters*, 42(9):3179–3187.

Gori, M., Rubino, V., Rosakis, A., and Lapusta, N. (2021). Dynamic rupture initiation and propagation in a fluid-injection laboratory setup with diagnostics across multiple temporal scales. *Proceedings of the National Academy of Sciences*, 118(51):e2023433118.

Grigoli, F., Cesca, S., Priolo, E., Rinaldi, A. P., Clinton, J., Stabile, T., Dost, B., Fernandez, M. G., Wiemer, S., and Dahm, T. (2017). Current challenges in monitoring, discrimination, and management of induced seismicity related to underground industrial activities: A European perspective. *Reviews of Geophysics*, 55(2):310–340.

Grigoli, F., Cesca, S., Rinaldi, A., Manconi, A., López-Comino, J., Clinton, J., Westaway, R., Cauzzi, C., Dahm, T., and Wiemer, S. (2018). The November 2017 M_w 5.5 Pohang earthquake: A possible case of induced seismicity in South Korea. *Science*, 360(6392):1003–1006.

Guglielmi, Y., Cappa, F., Avouac, J.-P., Henry, P., and Elsworth, D. (2015). Seismicity triggered by fluid injection–induced aseismic slip. *Science*, 348(6240):1224–1226.

Hager, B., Dieterich, J., Frohlich, C., Juanes, R., Mantica, S., Shaw, J., Bottazzi, F., Caresani, F., Castineira, D., Cominelli, A., et al. (2021). A process-based approach to understanding and managing triggered seismicity. *Nature*, 595(7869):684–689.

Hallo, M., Oprsal, I., Eisner, L., and Ali, M. (2014). Prediction of magnitude of the largest potentially induced seismic event. *Journal of Seismology*, 18(3):421–431.

He, C., Ma, S., and Huang, J. (1998). Transition between stable sliding and stick-slip due to variation in slip rate under variable normal stress condition. *Geophysical Research Letters*, 25(17):3235–3238.

Healy, J., Rubey, W., Griggs, D., and Raleigh, C. (1968). The Denver earthquakes. *Science*, 161(3848):1301–1310.

Heimisson, E., Dunham, E., and Almquist, M. (2019). Poroelastic effects destabilize mildly rate-strengthening friction to generate stable slow slip pulses. *Journal of the Mechanics and Physics of Solids*, 130:262–279.

Hofmann, H., Zimmermann, G., Farkas, M., Huenges, E., Zang, A., Leonhardt, M., Kwiatek, G., Martinez-Garzon, P., Bohnhoff, M., Min, K.-B., et al. (2019). First field application of cyclic soft stimulation at the Pohang enhanced geothermal system site in Korea. *Geophysical Journal International*, 217(2):926–949.

Hong, T. and Marone, C. (2005). Effects of normal stress perturbations on the frictional properties of simulated faults. *Geochemistry, Geophysics, Geosystems*, 6(3):Q03012.

Horton, S. (2012). Disposal of hydrofracking waste fluid by injection into subsurface aquifers triggers earthquake swarm in central Arkansas with potential for damaging earthquake. *Seismological Research Letters*, 83(2):250–260.

Hough, S. and Page, M. (2015). A century of induced earthquakes in Oklahoma? *Bulletin of the Seismological Society of America*, 105(6):2863–2870.

Hsieh, P. and Bredehoeft, J. (1981). A reservoir analysis of the Denver earthquakes: A case of induced seismicity. *Journal of Geophysical Research: Solid Earth*, 86(B2):903–920.

Hubbert, K. and Rubey, W. (1959). Role of fluid pressure in mechanics of overthrust faulting: I. mechanics of fluid-filled porous solids and its application to overthrust faulting. *Geological Society of America Bulletin*, 70(2):115–166.

Ikari, M., Saffer, D., and Marone, C. (2009). Frictional and hydrologic properties of clay-rich fault gouge. *Journal of Geophysical Research: Solid Earth*, 114(B5).

Im, K., Saffer, D., Marone, C., and Avouac, J.-P. (2020). Slip-rate-dependent friction as a universal mechanism for slow slip events. *Nature Geoscience*, 13(10):705–710.

Improta, L., Valoroso, L., Piccinini, D., and Chiarabba, C. (2015). A detailed analysis of wastewater-induced seismicity in the Val d'Agri oil field (Italy). *Geophysical Research Letters*, 42(8):2682–2690.

Iverson, R. (2005). Regulation of landslide motion by dilatancy and pore pressure feedback. *Journal of Geophysical Research: Earth Surface*, 110(F2).

Jaeger, J. and Cook, N. (1976). *Fundamentals of rock mechanics*. Chapman and Hall, London.

Kanamori, H. (1978). Quantification of earthquakes. *Nature*, 271(5644):411–414.

Kanamori, H., Heaton, T., and Rundle, J. (2000). Microscopic and macroscopic physics of earthquakes. *Geophysical Monograph-American Geophysical Union*, 120:147–164.

Kanamori, H. and Rivera, L. (2006). Energy partitioning during an earthquake. *Geophysical Monograph-American Geophysical Union*, 170(3):3–13.

Keranen, K., Weingarten, M., Abers, G., Bekins, B., and Ge, S. (2014). Sharp increase in central Oklahoma seismicity since 2008 induced by massive wastewater injection. *Science*, 345(6195):448–451.

Kilgore, B., Lozos, J., Beeler, N., and Oglesby, D. (2012). Laboratory observations of fault strength in response to changes in normal stress. *Journal of Applied Mechanics*, 79(3):031007.

Kim, W.-Y. (2013). Induced seismicity associated with fluid injection into a deep well in Youngstown, Ohio. *Journal of Geophysical Research: Solid Earth*, 118(7):3506–3518.

King, V., Block, L., Yeck, W., Wood, C., and Derouin, S. (2014). Geological structure of the Paradox Valley Region, Colorado, and relationship to seismicity induced by deep well injection. *Journal of Geophysical Research: Solid Earth*, 119(6):4955–4978.

Kirkpatrick, J., Edwards, J., Verdecchia, A., Kluesner, J., Harrington, R., and Silver, E. (2020). Subduction megathrust heterogeneity characterized from 3D seismic data. *Nature Geoscience*, 13(5):369–374.

Kitajima, H. and Saffer, D. (2012). Elevated pore pressure and anomalously low stress in regions of low frequency earthquakes along the Nankai trough subduction megathrust. *Geophysical Research Letters*, 39(23):L23301.

Kostrov, V. (1974). Seismic moment and energy of earthquakes, and seismic flow of rock. *Izv. Acad. Sci. USSR Phys. Solid Earth, Engl. Transl.*, 1:23–44.

Kraft, T. and Deichmann, N. (2014). High-precision relocation and focal mechanism of the injection-induced seismicity at the Basel EGS. *Geothermics*, 52:59–73.

Kwiatek, G., Martínez-Garzón, P., Plenkers, K., Leonhardt, M., Zang, A., Von Specht, S., Dresen, G., and Bohnhoff, M. (2018). Insights into complex subdecimeter fracturing processes occurring during a water injection experiment at depth in äspö hard rock laboratory, Sweden. *Journal of Geophysical Research: Solid Earth*, 123(8):6616–6635.

Lambert, C. (2017). Structural controls on fluid migration and seismic variability in northern Oklahoma. Master's Thesis, Dep. Earth Atmos. Sci., Cornell Univ., Ithaca, NY.

Lambert, V., Lapusta, N., and Perry, S. (2021). Propagation of large earthquakes as self-healing pulses or mild cracks. *Nature*, 591(7849):252–258.

Langenbruch, C., Weingarten, M., and Zoback, M. (2018). Physics-based forecasting of man-made earthquake hazards in Oklahoma and Kansas. *Nature Communications*, 9(1):3946.

Langenbruch, C. and Zoback, M. (2016). How will induced seismicity in Oklahoma respond to decreased saltwater injection rates? *Science Advances*, 2(11):e1601542.

Latour, S., Campillo, M., Voisin, C., Ionescu, I., Schmedes, J., and Lavallée, D. (2011). Effective friction law for small-scale fault heterogeneity in 3D dynamic rupture. *Journal of Geophysical Research: Solid Earth*, 116(B10).

Laursen, T. (2013). *Computational contact and impact mechanics: Fundamentals of modeling interfacial phenomena in nonlinear finite element analysis*. Springer Science & Business Media.

Lee, K.-K., Ellsworth, W., Giardini, D., Townend, J., Ge, S., Shimamoto, T., Yeo, I.-W., Kang, T.-S., Rhie, J., Sheen, D.-H., et al. (2019). Managing injection-induced seismic risks. *Science*, 364(6442):730–732.

Li, Z., Elsworth, D., and Wang, C. (2021). Constraining maximum event magnitude during injection-triggered seismicity. *Nature Communications*, 12(1528):1–9.

Lin, C.-C. and Segel, L. (1988). *Mathematics applied to deterministic problems in the natural sciences*. SIAM.

Linker, M. and Dieterich, J. H. (1992). Effects of variable normal stress on rock friction: Observations and constitutive equations. *Journal of Geophysical Research: Solid Earth*, 97(B4):4923–4940.

Lockner, D. and Okubo, P. (1983). Measurements of frictional heating in granite. *Journal of Geophysical Research: Solid Earth*, 88(B5):4313–4320.

Loveless, J. and Meade, B. (2016). Two decades of spatiotemporal variations in subduction zone coupling offshore Japan. *Earth and Planetary Science Letters*, 436:19–30.

Luo, Y. and Ampuero, J.-P. (2018). Stability of faults with heterogeneous friction properties and effective normal stress. *Tectonophysics*, 733:257–272.

Madariaga, R. (1976). Dynamics of an expanding circular fault. *Bulletin of the Seismological Society of America*, 66(3):639–666.

Majer, E., Baria, R., Stark, M., Oates, S., Bommer, J., Smith, B., and Asanuma, H. (2007). Induced seismicity associated with enhanced geothermal systems. *Geothermics*, 36(3):185–222.

Marone, C. (1998). Laboratory-derived friction laws and their application to seismic faulting. *Annual Review of Earth and Planetary Sciences*, 26(1):643–696.

Marone, C. (2002). Laboratory-derived friction laws and their application to seismic faulting. *Annual Review of Earth and Planetary Sciences*, 26(1):643–696.

Marone, C., Raleigh, C. B., and Scholz, C. (1990). Frictional behavior and constitutive modeling of simulated fault gouge. *Journal of Geophysical Research: Solid Earth*, 95(B5):7007–7025.

Marsden, J. and Hughes, T. (1994). *Mathematical foundations of elasticity*. Courier Corporation.

Martínez-Garzón, P., Kwiatek, G., Sone, H., Bohnhoff, M., Dresen, G., and Hartline, C. (2014). Spatiotemporal changes, faulting regimes, and source parameters of induced seismicity: A case study from the Geysers geothermal field. *Journal of Geophysical Research: Solid Earth*, 119(11):8378–8396.

Mate, C. M. (2008). *Tribology on the small scale: A bottom up approach to friction, lubrication, and wear*. Oxford University Press.

Mate, C. M., McClelland, G., Erlandsson, R., and Chiang, S. (1987). Atomic-scale friction of a tungsten tip on a graphite surface. *Physical Review Letters*, 59(1942):226–229.

McGarr, A. (1994). Some comparisons between mining-induced and laboratory earthquakes. *Pure and Applied Geophysics*, 142(3):467–489.

McGarr, A. (1999). On relating apparent stress to the stress causing earthquake fault slip. *Journal of Geophysical Research: Solid Earth*, 104(B2):3003–3011.

McGarr, A. (2014). Maximum magnitude earthquakes induced by fluid injection. *Journal of Geophysical Research: Solid Earth*, 119(2):1008–1019.

McGarr, A., Simpson, D., Seeber, L., and Lee, W. (2002). Case histories of induced and triggered seismicity. *International Geophysics Series*, 81(A):647–664.

Moreno, M., Rosenau, M., and Oncken, O. (2010). 2010 Maule earthquake slip correlates with pre-seismic locking of Andean subduction zone. *Nature*, 467(7312):198–202.

Mulargia, F. and Bizzarri, A. (2014). Anthropogenic triggering of large earthquakes. *Scientific Reports*, 4(1):1–7.

National Research Council (2013). *Induced seismicity potential in energy technologies*. National Academies Press. Washington, DC.

Norbeck, J. and Rubinstein, J. (2018). Hydromechanical earthquake nucleation model forecasts onset, peak, and falling rates of induced seismicity in Oklahoma and Kansas. *Geophysical Research Letters*, 45(7):2963–2975.

Nur, A. (1978). Nonuniform friction as a physical basis for earthquake mechanics. *Pure and Applied Geophysics*, 116(4):964–989.

Ogwari, P., DeShon, H., and Hornbach, M. (2018). The Dallas-Fort Worth airport earthquake sequence: Seismicity beyond injection period. *Journal of Geophysical Research: Solid Earth*, 123(1):553–563.

Ohnaka, M. (2000). A physical scaling relation between the size of an earthquake and its nucleation zone size. *Pure and Applied Geophysics*, 157(11-12):2259–2282.

Ohnaka, M. (2003). A constitutive scaling law and a unified comprehension for frictional slip failure, shear fracture of intact rock, and earthquake rupture. *Journal of Geophysical Research: Solid Earth*, 108(B2).

Olsson, W. (1988). The effects of normal stress history on rock friction. In *The 29th US Symposium on Rock Mechanics*. American Rock Mechanics Association.

Ougier-Simonin, A. and Zhu, W. (2013). Effects of pore fluid pressure on slip behaviors: An experimental study. *Geophysical Research Letters*, 40(11):2619–2624.

Pampillón, P., Santillán, D., Mosquera, J., and Cueto-Felgueroso, L. (2018). Dynamic and quasi-dynamic modeling of injection-induced earthquakes in poroelastic media. *Journal of Geophysical Research: Solid Earth*, 123(7):5730–5759.

Perfettini, H. and Schmittbuhl, J. (2001). Periodic loading on a creeping fault: Implications for tides. *Geophysical Research Letters*, 28(3):435–438.

Perfettini, H., Schmittbuhl, J., Rice, J., and Cocco, M. (2001). Frictional response induced by time-dependent fluctuations of the normal loading. *Journal of Geophysical Research: Solid Earth*, 106(B7):13455–13472.

Phillips, N. J., Belzer, B., French, M. E., Rowe, C. D., and Ujiie, K. (2020). Frictional strengths of subduction thrust rocks in the region of shallow slow earthquakes. *Journal of Geophysical Research: Solid Earth*, 125(3):e2019JB018888.

Pinchover, Y. and Rubinstein, J. (2005). *An introduction to partial differential equations*. Cambridge University Press.

Power, W., Tullis, T., Brown, S., Boitnott, G., and Scholz, C. (1987). Roughness of natural fault surfaces. *Geophysical Research Letters*, 14(1):29–32.

Pratt, W. and Johnson, D. (1926). Local subsidence of the Goose Creek oil field. *The Journal of Geology*, 34(7):577–590.

Rabinowicz, E. (1958). The intrinsic variables affecting the stick-slip process. *Proceedings of the Physical Society (1958-1967)*, 71(4):668.

Rabinowicz, E. (1965). *Friction and wear of materials*. John Willey & Sons, Inc. New York.

Raleigh, C. B., Healy, J., and Bredehoeft, J. (1976). An experiment in earthquake control at Rangely, Colorado. *Science*, 191(4233):1230–1237.

Ranjith, K. and Rice, J. (1999). Stability of quasi-static slip in a single degree of freedom elastic system with rate and state dependent friction. *Journal of the Mechanics and Physics of Solids*, 47(6):1207–1218.

Ray, S. and Viesca, R. (2017). Earthquake nucleation on faults with heterogeneous frictional properties, normal stress. *Journal of Geophysical Research: Solid Earth*, 122(10):8214–8240.

Rice, J. (1993). Spatio-temporal complexity of slip on a fault. *Journal of Geophysical Research: Solid Earth*, 98(B6):9885–9907.

Rice, J., Lapusta, N., and Ranjith, K. (2001). Rate and state dependent friction and the stability of sliding between elastically deformable solids. *Journal of the Mechanics and Physics of Solids*, 49(9):1865–1898.

Rice, J. and Tse, S. (1986). Dynamic motion of a single degree of freedom system following a rate and state dependent friction law. *Journal of Geophysical Research: Solid Earth*, 91(B1):521–530.

Richardson, E. and Marone, C. (1999). Effects of normal stress vibrations on frictional healing. *Journal of Geophysical Research: Solid Earth*, 104(B12):28859–28878.

Ringoot, E., Roch, T., Molinari, J.-F., Massart, T., and Cohen, T. (2021). Stick–slip phenomena and schallamach waves captured using reversible cohesive elements. *Journal of the Mechanics and Physics of Solids*, 155:104528.

Rivera, L. and Kanamori, H. (2005). Representations of the radiated energy in earthquakes. *Geophysical Journal International*, 162(1):148–155.

Rosakis, A., Rubino, V., and Lapusta, N. (2020). Recent milestones in unraveling the full-field structure of dynamic shear cracks and fault ruptures in real-time: From photoelasticity to ultrahigh-speed digital image correlation. *Journal of Applied Mechanics*, 87(3).

Rosson, Z., Walter, J., Goebel, T., and Chen, X. (2019). Narrow spatial aftershock zones for induced earthquake sequences in Oklahoma. *Geophysical Research Letters*, 46(17-18):10358–10366.

Rudnicki, J. and Freund, L. (1981). On energy radiation from seismic sources. *Bulletin of the Seismological Society of America*, 71(3):583–595.

Ruina, A. (1983). Slip instability and state variable friction laws. *Journal of Geophysical Research: Solid Earth*, 88(B12):10359–10370.

Rutter, E. and Hackston, A. (2017). On the effective stress law for rock-on-rock frictional sliding, and fault slip triggered by means of fluid injection. *Philosophical Transactions of the Royal Society A: Mathematical, Physical and Engineering Sciences*, 375(2103):20160001.

Sawai, M., Niemeijer, A., Plümper, O., Hirose, T., and Spiers, C. (2016). Nucleation of frictional instability caused by fluid pressurization in subducted blueschist. *Geophysical Research Letters*, 43(6):2543–2551.

Scholz, C. (1988). The critical slip distance for seismic faulting. *Nature*, 336(6201):761.

Scholz, C. (1998). Earthquakes and friction laws. *Nature*, 391(6662):37–42.

Scholz, C. (2002). *The mechanics of earthquakes and faulting*. Cambridge University Press.

Schultz, R., Corlett, H., Haug, K., Kocon, K., MacCormack, K., Stern, V., and Shipman, T. (2016). Linking fossil reefs with earthquakes: Geologic insight to where induced seismicity occurs in Alberta. *Geophysical Research Letters*, 43(6):2534–2542.

Scuderi, M. and Collettini, C. (2016). The role of fluid pressure in induced vs. triggered seismicity: Insights from rock deformation experiments on carbonates. *Scientific Reports*, 6:24852.

Scuderi, M. and Collettini, C. (2018). Fluid injection and the mechanics of frictional stability of shale-bearing faults. *Journal of Geophysical Research: Solid Earth*, 123(10):8364–8384.

Scuderi, M., Collettini, C., and Marone, C. (2017). Frictional stability and earthquake triggering during fluid pressure stimulation of an experimental fault. *Earth and Planetary Science Letters*, 477:84–96.

Segall, P. and Lu, S. (2015). Injection-induced seismicity: Poroelastic and earthquake nucleation effects. *Journal of Geophysical Research: Solid Earth*, 120(7):5082–5103.

Segall, P. and Rice, J. (1995). Dilatancy, compaction, and slip instability of a fluid-infiltrated fault. *Journal of Geophysical Research: Solid Earth*, 100(B11):22155–22171.

Segall, P., Rubin, A., Bradley, A., and Rice, J. (2010). Dilatant strengthening as a mechanism for slow slip events. *Journal of Geophysical Research: Solid Earth*, 115(B12).

Segel, L. and Slemrod, M. (1989). The quasi-steady-state assumption: A case study in perturbation. *SIAM Review*, 31(3):446–477.

Shapiro, S. and Dinske, C. (2009). Scaling of seismicity induced by nonlinear fluid-rock interaction. *Journal of Geophysical Research: Solid Earth*, 114(B9).

Shapiro, S., Patzig, R., Rothert, E., and Rindschwentner, J. (2003). Triggering of seismicity by pore-pressure perturbations: Permeability-related signatures of the phenomenon. In *Thermo-Hydro-Mechanical Coupling in Fractured Rock*. Springer.

Shearer, P. (2019). *Introduction to seismology*. Cambridge University Press.

Shlomai, H., Kammer, D., Adda-Bedia, M., and Fineberg, J. (2020). The onset of the frictional motion of dissimilar materials. *Proceedings of the National Academy of Sciences*, 117(24):13379–13385.

Silva, J., Byrne, H., Plesch, A., Shaw, J., and Juanes, R. (2021). Revisiting the classical experiment in earthquake control at the Rangely oil field, Colorado, 1970, using a coupled flow and geomechanical model. *Bulletin of the Seismological Society of America*, 111(6):3136–3159.

Simo, J., Marsden, J., and Krishnaprasad, P. (1988). The hamiltonian structure of nonlinear elasticity: The material and convective representations of solids, rods, and plates. *Archive for Rational Mechanics and Analysis*, 104(2):125–183.

Tang, L., Lu, Z., Zhang, M., Sun, L., and Wen, L. (2018). Seismicity induced by simultaneous abrupt changes of injection rate and well pressure in Hutubi gas field. *Journal of Geophysical Research: Solid Earth*, 123(7):5929–5944.

Thomas, M., Lapusta, N., Noda, H., and Avouac, J.-P. (2014). Quasi-dynamic versus fully dynamic simulations of earthquakes and aseismic slip with and without enhanced coseismic weakening. *Journal of Geophysical Research: Solid Earth*, 119(3):1986–2004.

Torberntsson, K., Stiernström, V., Mattsson, K., and Dunham, E. (2018). A finite difference method for earthquake sequences in poroelastic solids. *Computational Geosciences*, 22(5):1351–1370.

Truesdell, C. (1984). Historical introit the origins of rational thermodynamics. In *Rational Thermodynamics*. Springer.

Udías, A., Vallina, A. U., Madariaga, R., and Buforn, E. (2014). *Source mechanisms of earthquakes: Theory and practice*. Cambridge University Press.

Van Der Elst, N., Savage, H., Keranen, K., and Abers, G. (2013). Enhanced remote earthquake triggering at fluid-injection sites in the midwestern United States. *Science*, 341(6142):164–167.

Wang, H. (2000). *Theory of linear poroelasticity with applications to geomechanics and hydrogeology*. Princeton University Press.

Wang, L., Kwiatek, G., Rybacki, E., Bohnhoff, M., and Dresen, G. (2020a). Injection-induced seismic moment release and laboratory fault slip: Implications for fluid-induced seismicity. *Geophysical Research Letters*, 47(22):e2020GL089576.

Wang, L., Kwiatek, G., Rybacki, E., Bonnelye, A., Bohnhoff, M., and Dresen, G. (2020b). Laboratory study on fluid-induced fault slip behavior: The role of fluid pressurization rate. *Geophysical Research Letters*, 47(6):e2019GL086627.

Wang, W. and Scholz, C. (1994). Micromechanics of the velocity and normal stress dependence of rock friction. *Pure and Applied Geophysics*, 143(1-3):303–315.

Wei, S., Avouac, J.-P., Hudnut, K., Donnellan, A., Parker, J., Graves, R., Helmberger, D., Fielding, E., Liu, Z., and Cappa, F. (2015). The 2012 Brawley swarm triggered by injection-induced aseismic slip. *Earth and Planetary Science Letters*, 422:115–125.

Weingarten, M., Ge, S., Godt, J., Bekins, B., and Rubinstein, J. (2015). High-rate injection is associated with the increase in US mid-continent seismicity. *Science*, 348(6241):1336–1340.

Wells, D. and Coppersmith, K. (1994). New empirical relationships among magnitude, rupture length, rupture width, rupture area, and surface displacement. *Bulletin of the Seismological Society of America*, 84(4):974–1002.

Xing, T., Zhu, W., French, M., and Belzer, B. (2019). Stabilizing effect of high pore fluid pressure on slip behaviors of gouge-bearing faults. *Journal of Geophysical Research: Solid Earth*, 124(9):9526–9545.

Ye, L., Kanamori, H., and Lay, T. (2018). Global variations of large megathrust earthquake rupture characteristics. *Science Advances*, 4(3):eaao4915.

Yeck, W., Hayes, G., McNamara, D., Rubinstein, J., Barnhart, W., Earle, P., and Benz, H. (2017). Oklahoma experiences largest earthquake during ongoing regional wastewater injection hazard mitigation efforts. *Geophysical Research Letters*, 44(2):711–717.

Yeck, W., Weingarten, M., Benz, H., McNamara, D., Bergman, E., Herrmann, R., Rubinstein, J., and Earle, P. (2016). Far-field pressurization likely caused one of the largest injection induced earthquakes by reactivating a large preexisting basement fault structure. *Geophysical Research Letters*, 43(19):10–198.

Zhai, G., Shirzaei, M., Manga, M., and Chen, X. (2019). Pore-pressure diffusion, enhanced by poroelastic stresses, controls induced seismicity in Oklahoma. *Proceedings of the National Academy of Sciences*, 116(33):16228–16233.

Zoback, M., Kohli, A., Das, I., and McClure, M. (2012). The importance of slow slip on faults during hydraulic fracturing stimulation of shale gas reservoirs. In *SPE Americas Unconventional Resources Conference*. Society of Petroleum Engineers.